Analysis of Plane Strain Deformations of Linearly Elastic Strain-Gradient Materials by the Finite Element Method

Akshay Dahiya

Thesis submitted to the Faculty of the
Virginia Polytechnic Institute and State University
in partial fulfillment of the requirements for the degree of

Master of Science
in
Engineering Mechanics

Romesh C. Batra, Chair
Rakesh K. Kapania
Scott W. Case

December 15, 2020
Blacksburg, Virginia

Keywords: Strain-gradient theory, Lagrange multipliers, Finite element method, Infinitesimal deformations, Method of manufactured solutions.

Analysis of Plane Strain Deformations of Linearly Elastic Strain-Gradient Materials by the Finite Element Method

Akshay Dahiya

(ABSTRACT)

At small scales, numerous experimental studies have shown that material behavior strongly depends upon the specimen size. Classical theories are unable to explain this size dependence, whereas a strain gradient continuum theory has intrinsic *length scales* and may well describe mechanical deformations of small size bodies. In the current contribution, we develop a numerical software based on the finite element method (FEM) to analyze infinitesimal deformations of strain-gradient dependent materials by introducing auxiliary variables to enable the use of simple low order polynomials as basis functions. We use Lagrange multipliers to satisfy the non-classical boundary conditions pertinent to strain gradients. To verify the developed software, we analyze plane strain deformations of a clamped, transversely isotropic beam. The obtained stresses and displacements compare well with the analytical solutions available in the literature, thus verifying the numerical solution. The Method of Manufactured solutions (MMS) was used to further verify the developed code as the assumed displacements and the resulting stresses were successfully reproduced. To study the effect of the *material characteristic length* (l_c) in isotropic and transversely isotropic materials, we numerically study some known problems of plane strain elasticity and compare the classical and strain-gradient solutions. As l_c is increased, the beam becomes stiffer as evidenced by a decreased tip deflection under the same loads. This numerically predicted stiffening reflects the experimental findings. We also observe that as the beam thickness becomes much larger as compared to l_c, the strain-gradient solution approaches the classical solution.

Analysis of Plane Strain Deformations of Linearly Elastic Strain-Gradient Materials by the Finite Element Method

Akshay Dahiya

(GENERAL AUDIENCE ABSTRACT)

Classical mechanics-based material models help us understand how large scale bodies deform. However, when bodies are very small—like in microelectronics or biomedical implants—experiments show that their behavior is stiffer than that predicted by the classical theories. To address this, researchers have developed advanced theories, such as a *strain-gradient theory*, which considers both strains and strain-gradients in developing stress-strain relations and hence equilibrium equations. These theories introduce additional material parameters that may help explain small-scale effects. In this thesis, we have used a strain-gradient theory and developed the associated software using the finite element method. We verified the software using a well-known mathematical approach, called the Method of Manufactured Solutions (MMS), and then use it to study bending of small beams to delineate the effect of specimen size on its response to applied loads. Our results support the test observation that a beam becomes stiffer as its size becomes smaller.

Dedication

To my late grandfather, Sh. Dhoop Singh Dahiya.

Acknowledgments

I would like to thank my advisor, Dr. Romesh C. Batra, for his invaluable guidance and support throughout my research. His meticulous review and insightful suggestions have greatly enhanced the quality of this work. I am also sincerely grateful to my committee members, Dr. Rakesh K. Kapania and Dr. Scott W. Case, for their valuable feedback.

I extend my gratitude to the Biomedical Engineering and Mechanics (BEAM) Department at Virginia Tech for the opportunity to pursue my Master's degree and for providing the necessary computational resources. Additionally, I appreciate my labmates — Lisha Yuan, Balachandar Guduri, Berkan Alanbay, Dongho Justin Kim, and Devin Burns—in the Computational Mechanics Laboratory for their helpful discussions and feedback on my research.

Finally, I would like to thank my parents, sister, and brother for their unwavering belief in me and their constant support.

I take full responsibility for any errors in this thesis.

Contents

List of Figures ix

List of Tables xii

1 Introduction 1

1.1 Background and Motivation 2

1.2 Research Objectives 3

1.3 Organization of the thesis 3

2 Review of Literature 5

3 Problem Formulation 9

3.1 Problem Formulation for Linearly Elastic Strain-Gradient Materials 9

3.1.1 Transversely Isotropic Material 13

3.2 Finite element formulation of the problem 15

4 Results and Discussion 23

4.1 Verification of the developed software 23

4.1.1 Verification of the code by using the method of manufactured solutions 23

4.1.2 Plane strain deformation of a clamped-clamped transversely isotropic beam . . . 29

4.2 Numerical Examples . . . 33

4.2.1 An isotropic cantilever beam under a uniform tangential traction . . 33

4.2.2 An isotropic and a transversely isotropic cantilever beam under a tangential traction at the unclamped edge . . . 39

4.2.3 Clamped transversely isotropic beam under a sinusoidal load on the top surface . . . 43

4.2.4 Clamped transversely isotropic beam under a sinusoidal load with 25 half-waves . . . 48

4.2.5 Isotropic cantilever beam under higher-order loading . . . 50

5 Conclusions **54**

Bibliography **56**

Appendices **62**

Appendix A FEM details **63**

A.1 Assembly of global stiffness matrix $\boldsymbol{K}_g$ . . . 63

A.2 Method of constraint counting . . . 67

A.3 Expressions for MMS . . . 69

A.4 Expressions for shape functions . . . 71

A.5 Iterative procedure 77

Appendix B MATLAB codes **79**

B.1 Solution using *mldivide* : direct solver 79

B.2 Plotting 90

B.3 Chebyshev–Gauss–Lobatto (CGL) grid 102

List of Figures

3.1 A 3-D body with domain Ω and unit normal vector n_i and a unit tangent vector e_i illustrating edges a) $\Gamma(\overline{\partial_1\Omega} \cap \overline{\partial_2\Omega})$ and b) $\Gamma_p(\overline{\partial_3\Omega} \cap \overline{\partial_4\Omega})$. 12

3.2 Sketch of $QU34L4$, $QU34L16$ and $QU48L32$ finite elements. $QU34L16$ and $QU48L32$ FEs were studied by Shu et al. [1] 17

4.1 Geometric configuration of the body. 24

4.2 Comparison of computed and assumed (MMS) displacements on the line $\bar{x}_1 = 0.5$. 26

4.3 Comparison on the line $\bar{x}_1 = 0.5$ of the computed and the MMS values of displacement gradients. 26

4.4 Comparison of through-the-thickness distributions of classical stresses at $\bar{x}_1 = 0.5$. 27

4.5 Comparison of through-the-thickness distributions of higher-order stresses at $\bar{x}_1 = 0.5$. 28

4.6 Comparison of the MMS solution with the computed results using three different elements $QU34L4$ (40×40), $QU34L16$ (12×12), and $QU48L32$ (12×12). 30

4.7 Sketch of the beam problem with sinusoidal load on the top surface. 31

4.8 Non-dimensional deformed shapes of the mid-surface for $L/H = 4$, 10 and 20. 32

4.9 For the beam with $(L/H = 4)$, through-the-thickness distributions of the non-dimensional axial and shear stresses at different locations. 32

4.10 Sketch of the beam under a uniform shear traction at the right edge. 34

4.11 For $l_c = 0$, 2, 6, and 10 mm, deformed mid-surfaces of the clamped beam. . 34

4.12 Through-the-thickness distributions of non-dimensional surface traction t_1 and t_2 at different values of x_1/L. 35

4.13 Axial distribution of non-dimensional surface traction t_1 and t_2 at different values of x_2/H. 36

4.14 Variations on planes X_1 = constant of t_1, t_2, r_1 and r_2 at the point $x_2 = -0.025H$. 37

4.15 The logarithm of the ratio of stiffness versus the logarithm of H/l_c. 38

4.16 The non-dimensional deflection versus H/l_c. 38

4.17 Sketch of the beam under a parabolic shear traction at the right edge. 39

4.18 Deflections of the mid-surface of the beam for different values of the characteristic length; (left) isotropic, and (right) transversely isotropic material. . . 40

4.19 For the isotropic material beam, variations on planes x_1 =constant of t_1, t_2, r_1 and r_2 at the point $x_2 = -0.0417H$. 42

4.20 For the transversely isotropic material beam, variations on planes x_1 =constant of t_1, t_2, r_1 and r_2 at the point $x_2 = -0.0417H$. 43

4.21 Sketch of the beam under a sinusoidal load on the top surface. 44

4.22 For $l_c = 0$, 2, 4, 6, 8 and 10 mm, deformed mid-surfaces of the clamped beam. 45

4.23 Distributions of t_1, t_2, r_1 and r_2 on the plane $x_2 = 0.4353H$. 46

4.24 Deflections of the mid-surface of the beam with angles of transverse isotropy ($l_c = 4\ mm$), and a sketch of the beam showing the angle of transverse isotropy. 47

4.25 The non-dimensional deflection versus $n = H/l_c$. 48

4.26 Sketch of the beam under a sinusoidal load with 25 half-waves on the top surface. 49

4.27 Deflections of the mid-surface of the beam with different values of the characteristic length. 50

4.28 Distributions of t_1, t_2, r_1 and r_2 on the plane $x_2 = 0.4353H$. 51

4.29 Sketch of the beam under a higher-order surface traction, r_2, at the right edge. 52

4.30 Distributions of t_1, t_2, r_1 and r_2 on the plane $x_2 = 0.4643H$. 53

A.1 Standard mesh with n elements in both x_1 and x_2 directions and the left and bottom edges are clamped. 67

A.2 Sketch of the $QU34L4$ finite element. 73

A.3 Sketch of the $QU34L16$ finite element. 74

A.4 Sketch of the $QU48L32$ finite element. 76

List of Tables

4.1 Maximum % relative difference between the computed and the assumed MMS solution for five different meshes. 25

4.2 % Relative difference between the computed results with varying mesh size for non-dimensional displacement and displacement gradients for the case L/H=4. 31

4.3 Deflections at the tip of the mid-surface of the beam for different values of l_c. 34

4.4 For isotropic and transversely isotropic material beams with the axis of transverse isotropy along the beam axis, deflections at the tip of the mid-surface of the beam for different values of l_c. [Analytical solution for isotropic material beam and $l_c = 0$: $u_2(m) = -0.201$] 41

4.5 Maximum deflections of the beam's mid-surface ((u_2^{max})) with different values of the characteristic length l_c. 44

4.6 Maximum deflections of the beam's mid-surface with different angles of transverse isotropy and characteristic length values. 45

4.7 Maximum deflections of the beam's mid-surface for strain-gradient theory (u_2^{sgt}) and the classical theory ($u_2^{classical}$) for different values of H/l_c. 47

4.8 Maximum deflections ((u_2^{max})) of the beam's mid-surface for different values of the characteristic length l_c. 49

Chapter 1

Introduction

With the advent of nanotechnology and increased applications of solids at small scales, researchers have renewed interest in gradient-based theories. At such small sizes, the classical theory produces inaccurate results, whereas non-local and higher-order theories have proved to be effective. Numerous works have focused on exploring strain-gradient based approaches, both experimentally and theoretically, for estimating the response of small scale solids.

In the past few decades, we have seen an exponential rise in computing capacity. The use of advanced numerical techniques such as the Finite Element Method (FEM) is often quicker and less expensive than experimental investigations. Any physical phenomenon, from the bending of a beam to blood flow in veins, can be represented by a mathematical model that consists of a set of equations (either ordinary, partial differential, integral or algebraic) along with suitable initial and boundary conditions. The FEM, a widely popular technique among the engineering community, relies on the discretization of the geometry, i.e., subdividing the structure into an assembly of simple (finite) elements. The problem of solving a complex partial differential equation gets simplified to solving a system of linear algebraic equations. And if the FE mesh is fine enough, the approximate solution is sufficiently accurate.

In this thesis, we have analyzed plane strain deformations of linearly elastic strain-gradient materials using the FEM. As higher-order theories like strain-gradient contain higher-order derivatives of displacements, one would require at least C^1-continuous elements to ensure a converged solution in the FEM. We use isoparametric quadrilateral elements and introduce

auxiliary variables to allow the use of low order polynomials as the basis functions. We use Lagrange multipliers to satisfy the kinematic constraints pertinent to displacement gradients and use the principle of minimum potential energy to obtain a weak form of the equilibrium equations. To understand the effect of new material parameters introduced in the strain-gradient theory, we compare the classical solution with the strain-gradient solutions.

1.1 Background and Motivation

Classical continuum mechanics theories have proved to be appropriate when the wavelength of a deformation field is much larger than the length scale of the material's lattice structure. However, at micron and sub-micron levels, material behavior displays strong size dependence as the two length scales are comparable. For example, in the micro-torsion of thin copper wires, Fleck et al. [2] observed that the shear strength increases three times as wire diameter decreases from 170 to 12 µm. This indicates drawbacks of classical mechanics for small size structures.

The Cosserat brothers [3] were the first to propose a non-local continuum theory for linear elastic materials known as a *couple stress theory*. In addition to the material displacement $\boldsymbol{u}$, they defined an independent rotation quantity $\boldsymbol{\theta}$. Couple stresses were assumed as the work conjugate to the spatial gradient of $\boldsymbol{\theta}$, called micro-curvature. Later, Toupin [4], and Mindlin [5] proposed a theory in which the strain energy of linear elastic material is a function of the gradient of strain, in addition to strain.

These theories introduce new material properties, which are supposedly correlated to the atomic structure of the lattice, but no proof has been established yet. Artan and Batra [6] amongst other investigators, studied free vibrations of strain-gradient beams and found that *material characteristic length* noticeably affected frequencies of free vibration.

1.2 Research Objectives

As compared to the classical theory, solving differential equations for a strain-gradient theory is more complex because of the involvement of gradients of the kinematic tensors. Hence, numerical techniques like the FEM are used to solve these complex problems.

In a strain-gradient theory, the internal work is done by a mathematical combination of the Cauchy stresses and higher-order stresses pertinent to strain gradients.

The main research objectives of this work are as follows:

1. To develop a finite element code for studying 2-D plane strain problems for a strain gradient theory pertinent to linearly elastic solids.

2. To verify the developed code by comparing the results for problems solved in the literature and by using the Method of Manufactured Solutions (MMS).

3. To understand the effect of the new material constants pertinent to the strain gradient theory.

4. To study the effect of the *material characteristic length* for simple problems.

1.3 Organization of the thesis

The assembly of the rest of the thesis is as follows:

Chapter 2 includes the literature review and contributions of our work. We look at some of the work related to the application of higher-order theories and their implementation in numerical techniques like the Finite Element Method.

Chapter 3 describes the adopted methodology, introducing the governing equations and boundary conditions pertinent to a strain gradient theory, related constitutive relations, formulation of the finite element problem, the weak form, and the implementation of the theoretical framework in a MATLAB code.

In chapter 4, we verify the developed MATLAB code by comparing its predictions with those available in the literature for a few simple problems and the Method of Manufactured Solution. Then we present the results for various beam problems for isotropic and transversely isotropic materials.

In chapter 5, we summarize the conclusions and contributions of this work. In Chapter 6, we discuss some future directions related to this work, followed by Bibliography. The Appendix contains the in-house developed MATLAB codes and the related details.

Chapter 2

Review of Literature

Reviewing all relevant works is beyond the scope of the thesis. The author regrets having missed many significant works in the field.

The success of non-local or higher-order theories is attributed to the introduction of length scales dependent variables. Motivated by Mindlin's work [7], Aifantis [8] proposed a simplified and robust model with just one non-classical material constant, called the *material characteristic length*.

Experimental evidence of size effects in plastic materials has also been reported. This led to the development of non-local plasticity theories, among others, by Dillon and Kratochvil [9], Aifantis [10], and Fleck and Hutchinson [11]. Later, Hwang et al. [12] proposed a strain gradient theory of plasticity for finite deformations. Batra [13] has used a strain gradient theory to study elastoplastic deformations.

Batra [14] studied the thermodynamics of hyperelastic materials whose strain energy density depends upon the first- and the second-order gradients of the deformation, the temperature, its gradient, and the time rate of change of the temperature. He used an entropy inequality proposed by Green and Laws [15] to study its compatibility with the second law of thermodynamics. He showed that in such materials, either thermal disturbances propagate with a finite speed in the linear theory and the constitutive quantities do not depend upon the second-order gradients of the deformation or the constitutive quantities may depend upon

the second-order gradients of the deformation, and in the linear theory, thermal disturbances do not propagate with finite speed.

Yang et al. [16] used a strain gradient theory to study problems for linearly elastic isotropic materials. Hwang and Batra [17] used a strain gradient-based theory to analyze adiabatic shear bands in viscoplastic materials.

Kandaz et al.[18] used a modified strain gradient theory (MSGT) and a modified couple stress theory (MCST) to analyze microbeams using the FEM. By comparison with the experimental results in the literature, they concluded that higher-order theories should be used for gold microbeams with thickness $< 30\ \mu m$. Amanatidou et al. [19] used a mixed FE formulation and proposed 3 different isoparametric elements with one having 28 DoFs and other two with 70 DoFs to study plane strain problems in strain-gradient elasticity.

Andreaus et al. [20] studied the role of external double edge forces and external wedge forces in second-gradient elasticity using a commercial code and established mesh-independency in results. They further showcased the importance of second gradient implementation using experimental evidence of an internal boundary layer for a non-linear anisotropic problem. Ansari et al. [21] proposed a quadrilateral element based FEM approach to study bending of microplates using Mindlin's strain gradient theory. Jafari et al. [22] used first and second order gradient theories to numerically study vibrations of beams. They also investigated the effect of different boundary conditions, beam size and material characteristic lengths.

Tsinopoulos et al. [23] have thoroughly reviewed both the boundary element method (BEM) and the FEM for static and dynamic strain gradient elasticity problems. Peddieson et al. [24] extended the Euler-Bernoulli beam model to study linear elastic beams using a simplified version of Eringen's [25] non-local continuum theory. For the lateral deflection of a simply supported beam with a uniformly distributed load, they derived a sixth-order

ordinary differential equation and found the expression for the deflection by using only two boundary conditions at each end.

Yury and Lurie [26] obtained a semi-inverse analytical solution of a plane strain pure bending problem for a piezoelectric layer in the framework of linear electroelasticity theory with strain gradient and electric field gradient effects. They discussed the importance of ensuring the fulfillment of boundary conditions on the top and the bottom surfaces of the beam [27] and proposed a consistent variational approach for developing gradient beam models.

The following few paragraphs review the application of the FEM in gradient theories. Shu et al. [1] applied the mixed finite element formulation that bypassed the construction of higher-order Hermite shape functions. The authors proposed six different finite elements for two-dimensional problems and recommended two quadrilateral elements for practical use, each having 34 degrees of freedom.

Beheshti [28] used Hermite polynomials to numerically study strain-gradient solids using 4-noded quadrilateral elements in the FEM. However, the author enforced only one non-classical or higher-order boundary condition at the fixed end of the cantilever, as mentioned in Eq.(3.7d).

Various other numerical techniques have been explored to study problems in strain-gradient elasticity such as, the meshless method, isogeometric analysis. [29] used the Hellinger-Reissner variational principle to develop a finite element model for linear second-order strain gradient elasticity. They applied various boundary conditions on polyhedra and concluded that first-gradient and second-gradient materials do not sustain point forces at corners.

In the current contribution, we develop a finite element code for analyzing plane-strain deformations of strain-gradient dependent materials by introducing displacement gradients as auxiliary variables (added nodal degrees of freedom) and Lagrange multipliers that facilitates

using simple low order polynomials as basis functions.

The Method of Manufactured Solutions (MMS) is a mathematical approach used to verify that a given code solves the underlying governing equations correctly. Roache [30] used MMS and verified that mesh refinement and time step refinement reduces numerical error at the expected rate based on the underlying numerical schemes. Steinberg and Roache described this technique more formally in [31]. Batra and Liang [32] and Batra and Love [33] used a similar technique called the 'method of fictitious body forces' to verify finite element codes and for error quantification.

Chapter 3

Problem Formulation

3.1 Problem Formulation for Linearly Elastic Strain-Gradient Materials

We follow Toupin [4] and Mindlin [5] in assuming that for a homogeneous, isotropic and linearly elastic strain-gradient material, the strain energy density is the sum of a quadratic function of the infinitesimal strain tensor, ϵ_{ij}, and a quadratic function of the strain-gradient, κ_{ijk}. That is, in rectangular Cartesian coordinates,

$$W(\epsilon_{ij},\kappa_{ijk}) = \frac{1}{2}\lambda\epsilon_{ii}\epsilon_{jj} + \mu\epsilon_{ij}\epsilon_{ij} + a_1\kappa_{iik}\kappa_{kjj} + a_2\kappa_{ijj}\kappa_{ikk} + a_3\kappa_{iik}\kappa_{jjk} + a_4\kappa_{ijk}\kappa_{ijk} + a_5\kappa_{ijk}\kappa_{kji} \tag{3.1}$$

where

$$\epsilon_{ij} = \frac{1}{2}(u_{i,j} + u_{j,i}) = \epsilon_{ji} \tag{3.2a}$$

$$\kappa_{ijk} = \frac{\partial\epsilon_{ij}}{\partial x_k} = \frac{1}{2}(u_{i,jk} + u_{j,ik}) = \kappa_{jik} \tag{3.2b}$$

where $\boldsymbol{u}(\boldsymbol{x})$ is the displacement vector at a point $\boldsymbol{x} = \{x_1, x_2, x_3\}$ and $u_{i,j} = \partial u_i/\partial x_j$, a free index takes values 1, 2, 3, and a repeated index implies summation over the range of the index. For a three dimensional solid, W is a function of 24 variables because $\epsilon_{ij} = \epsilon_{ji}$ and $\kappa_{ijk} = \kappa_{jik}$. Note that the expression (3.1) for W does not have terms containing the product

of ϵ_{ij} and κ_{ijk} because the only 5th order isotropic tensor is the null tensor. Furthermore, λ and μ are the Lame' constants having units of stress [Pascal (Pa) or pound-force per square inch (psi)], κ_{ijk} has the units of 1/length [1/meter ($1/m$) or 1/inch ($1/in$)], and the material moduli a_1 through a_5 associated with the strain-gradients have units of stress times area or force [Newton (N) or pound-force (lbf)][1].

Altan and Aifantis [34] proposed a simple form of W by setting the following values for $a_1 - a_5$ in (3.1):

$$a_1 = 0, a_2 = \frac{1}{2}\lambda l_c^2, a_3 = 0, a_4 = \mu l_c^2, a_5 = 0 \tag{3.3}$$

where l_c is a material characteristic length. Thus, in Altan and Aifantis' work [34], there is only one additional material parameter, l_c, for an isotropic strain-gradient material. Henceforth, this assumption was adopted. For W to be positive definite for non-rigid deformations, it is required that $\mu > 0$ and $(3\lambda + 2\mu) > 0$, implying that the shear modulus and the bulk modulus are positive.

The Cauchy stress σ_{ij} and the higher-order stress τ_{ijk} are work conjugates of ϵ_{ij} and κ_{ijk}. Their expressions are:

$$\sigma_{ij} = \sigma_{ji} = \frac{\partial W}{\partial \epsilon_{ij}} = \lambda \epsilon_{kk}\delta_{ij} + 2\mu\epsilon_{ij} \tag{3.4a}$$

$$\tau_{ijk} = \tau_{jik} = \frac{\partial W}{\partial \kappa_{ijk}} = l_c^2(\lambda \kappa_{ppk}\delta_{ij} + 2\mu\kappa_{ijk}) \tag{3.4b}$$

That is, the Cauchy stress depends only upon the infinitesimal strains, ϵ_{ij}, and the higher-order stress only upon the strain-gradients, κ_{ijk}.

Equilibrium equations and boundary conditions:

We follow Toupin [4] and use the principle of minimum potential energy to derive equilibrium

[1] In this work, all quantities are expressed in the SI units. For conversion to the US Customary units: $1/m = 0.0254\ 1/in$; $1\ Pa = 1.45038 \times 10^{-4}\ psi$; $1\ Pa \cdot m = 0.00571\ psi \cdot in$; $1\ N = 0.224809\ lbf$.

equations and the boundary conditions. The potential energy, Π, is defined by

$$\Pi = \left[\int_\Omega W dV\right] - \left[\int_\Omega b_i u_i dV + \int_{\partial\Omega} \left(t_i u_i + r_i \frac{\partial u_i}{\partial n}\right) dA + \int_{\Gamma_p} p_i u_i d\Gamma\right] \tag{3.5}$$

where b_i is the body force per unit volume, t_i and r_i are the surface traction and the higher-order surface traction prescribed on the boundary $\partial\Omega$, and p_i is the line force per unit length on the edge Γ_p intercepted by two smooth surfaces $\partial_3\Omega$ and $\partial_4\Omega$ as shown in Fig 3.1a. Necessary conditions for Π to be stationary for all admissible displacement fields $\boldsymbol{u}(\boldsymbol{x})$ are:

$$(\sigma_{ij} - \tau_{ijk,k})_{,\,j} + b_i = 0 \quad \boldsymbol{x} \in \Omega \tag{3.6}$$

and

$$(\sigma_{ij} - \tau_{ijk,k})n_j - (\tau_{ijk}n_k)_{,\,j} - (\tau_{ijk}n_k n_l)_{,\,l} n_j = t_i \text{ on } \partial_1\Omega \tag{3.7a}$$

$$u_i = \bar{u}_i \text{ on } \partial_2\Omega \tag{3.7b}$$

$$\tau_{ijk}n_j n_k = r_i \text{ on } \partial_3\Omega \tag{3.7c}$$

$$u_{i,j}n_j = 0 \text{ on } \partial_4\Omega \tag{3.7d}$$

$$[[\tau_{ijk}m_j n_k]] = p_i \text{ on } \Gamma_p(\,\overline{\partial_3\Omega} \,\cap\, \overline{\partial_4\Omega}\,) \tag{3.7e}$$

Here n_i is the outward unit normal vector to $\partial\Omega$ as shown in Fig 3.1. $\partial_1\Omega$ and $\partial_2\Omega$ are complementary parts of the boundary of Ω where surface traction, t_i, and displacement, $\bar{u}_i$, are prescribed, respectively. Similarly, $\partial_3\Omega$ and $\partial_4\Omega$ are complementary parts of the boundary of Ω where higher-order surface traction, r_i, and normal derivative of the displacements, $u_{i,j}n_j$, are prescribed, respectively. Also, $m_j = \epsilon_{jml}s_m n_l$ where ϵ_{jml} is the permutation symbol and s_m is the unit vector tangent to the edge: $\Gamma_p(\overline{\partial_3\Omega} \,\cap\, \overline{\partial_4\Omega})$ as shown in Fig 3.1b. The notation [[…]] indicates the difference between the values of the quantity inside

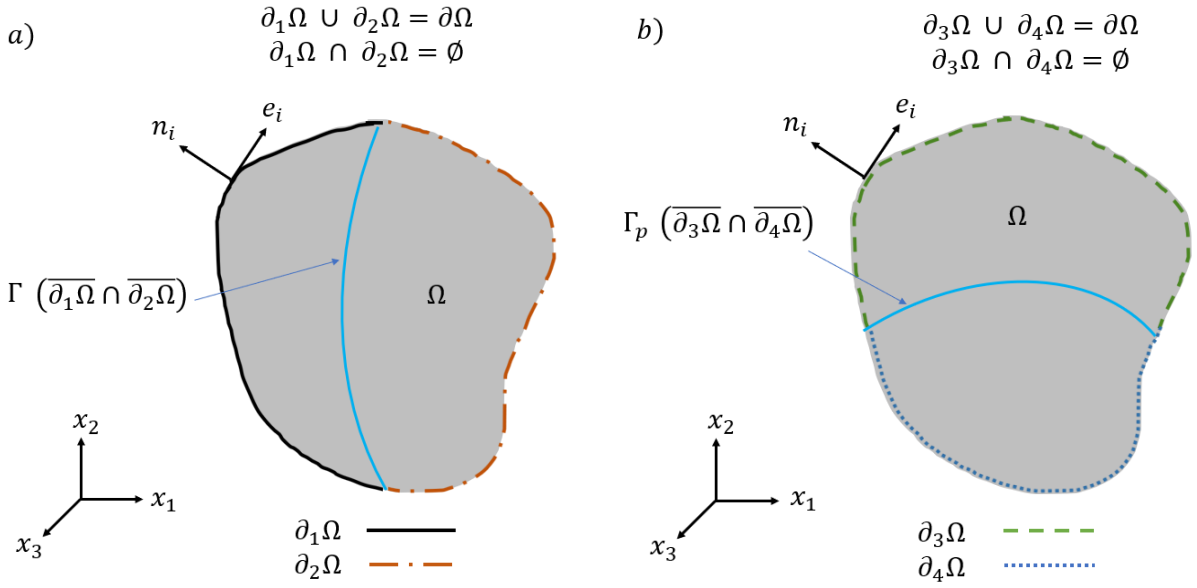

Figure 3.1: A 3-D body with domain Ω and unit normal vector n_i and a unit tangent vector e_i illustrating edges a) $\Gamma(\overline{\partial_1\Omega} \cap \overline{\partial_2\Omega})$ and b) $\Gamma_p(\overline{\partial_3\Omega} \cap \overline{\partial_4\Omega})$.

[[...]] across the edge: $\overline{\partial_3\Omega} \cap \overline{\partial_4\Omega}$.

We note that both σ_{ij} and τ_{ijk} contribute to the surface traction t_i as evidenced by Eq. (3.7a). Thus, on a surface with the outward unit normal n_j, the normal traction equals $t_i n_i$ and the shear traction in the direction e_i equals $t_i e_i$ where $n_i e_i = 0$. That is, e_i is a unit vector in the plane perpendicular to n_i.

In this work, we ignore the boundary condition (3.7e) at the edges because of the *St. Venant's principle* [35] that implies that this term will influence the solution only near the edge.

Plane strain deformations:

We assume that the x_1x_2-plane is the deformation plane, $u_3 = 0$, and

$$u_1 = u_1(x_1, x_2), u_2 = u_2(x_1, x_2) \tag{3.8}$$

Thus,

$$\epsilon_{k3} = \kappa_{33k} = \kappa_{13k} = \kappa_{23k} = \kappa_{113} = \kappa_{223} = \kappa_{123} = 0 \text{ where } k \in \{1, 2, 3\} \tag{3.9}$$

From Eq.(3.4a) and (3.4b), the classical stress, σ_{ij}, and the higher-order stress, τ_{ijk}, can be written as:

$$\begin{gathered}
\sigma_{11} = (\lambda + 2\mu)\varepsilon_{11} + \lambda\varepsilon_{22};\ \sigma_{22} = \lambda\varepsilon_{11} + (\lambda + 2\mu)\varepsilon_{22};\ \sigma_{12} = 2\mu\varepsilon_{12} \\
\tau_{111} = l_c^2(\lambda + 2\mu)\kappa_{111} + l_c^2\lambda\kappa_{221};\ \tau_{112} = l_c^2\lambda\kappa_{222} + l_c^2(\lambda + 2\mu)\kappa_{112} \\
\tau_{221} = l_c^2\lambda\kappa_{111} + l_c^2(\lambda + 2\mu)\kappa_{221};\ \tau_{222} = l_c^2\lambda\kappa_{112} + l_c^2(\lambda + 2\mu)\kappa_{222} \\
\tau_{211} = 2l_c^2\mu\kappa_{211};\ \tau_{212} = 2l_c^2\mu\kappa_{212}
\end{gathered} \tag{3.10}$$

3.1.1 Transversely Isotropic Material

We assume the following form of the strain energy density for a linearly elastic strain gradient-dependent material [7]:

$$W = \frac{1}{2}C_{ijkl}\epsilon_{ij}\epsilon_{kl} + \frac{1}{2}A_{ijklmn}\kappa_{ijk}\kappa_{lmn} \tag{3.11}$$

where C_{ijkl} and A_{ijklmn} are the fourth- and the sixth-order tensors of the elastic moduli. C_{ijkl} and A_{ijklmn} possess the following relations:

$$C_{ijkl} = C_{klij} = C_{jikl}, A_{ijklmn} = A_{lmnijk} = A_{jiklmn} \tag{3.12}$$

Gitman et al. [36] assumed that:

$$A_{ijklmn} = C_{ijkl}L_{mn} \tag{3.13}$$

We follow [36, 37, 38] and assume (3.13) with $L_{ij} = l_c^2 \delta_{ij}$. Hence, there is only a single length scale parameter l_c. When $l_c = 0$, the strain energy density (3.11) reduces to that for the classical theory.

The stress-strain laws are given by:

$$\sigma_{ij} = \frac{\partial W}{\partial \epsilon_{ij}} = C_{ijkl}\epsilon_{kl} \tag{3.14a}$$

$$\tau_{ijk} = \frac{\partial W}{\partial \kappa_{ijk}} = A_{ijklmn}\kappa_{lmn} = l_c^2 C_{ijlm}\kappa_{lmk} \tag{3.14b}$$

To obtain stress-strain relations for a transversely isotropic material, we need the explicit form of C_{ijkl}. Assuming plane strain deformations with x_1x_2-plane to be the deformation plane and x_1 to be the axis of transverse isotropy, the 4 non-zero components of the elasticity matrix C_{ijkl} are [33]:

$$\begin{gathered} C_{11} = 1/E_1 \; ; \; C_{12} = -v_{12}/E_1 \; ; \; C_{22} = 1/E_2 \; ; \; C_{23} = -v_{23}/E_2 \\ C_{1111} = \left(C_{22}C_{22} - C_{23}C_{23}\right)/C_v \; ; \; C_{1122} = \left(C_{12}C_{23} - C_{12}C_{22}\right)/C_v \\ C_{2222} = \left(C_{22}C_{11} - C_{12}C_{12}\right)/C_v \; ; \; C_{1212} = G_{12} \\ \text{where } C_v = C_{11}C_{22}C_{22} - C_{11}C_{23}C_{23} - C_{22}C_{12}C_{12} - C_{22}C_{12}C_{12} + 2C_{12}C_{23}C_{12}. \end{gathered} \tag{3.15}$$

where E_1 is the Young's modulus in the x_1-direction, E_2 is the Young's modulus in the x_2-direction, G_{12} is the shear modulus in the $x_1 - x_2$ plane, and v_{12} is the Poisson's ratio for loading along the longitudinal x_1-axis.

In Chapter 4, we present results for strain-gradient transversely isotropic materials under different loading. We try to understand the effect of the material characteristic length and the direction of transverse isotropy on the mechanical response of strain gradient-dependent solids.

3.2 Finite element formulation of the problem

Recalling the expression (3.1) for W we note that in order to integrate W over the domain Ω occupied by the body, squares of κ_{ijk} must be integrable over Ω. This requires that the displacement field $\boldsymbol{u}(\boldsymbol{x})$ must be continuously differentiable on Ω. A possibility is to use Hermitian basis functions for approximating $\boldsymbol{u}(\boldsymbol{x})$ as was done by Beheshti [28]. However, Hermitian basis functions for 2-dimensional problems pose challenges at vertices of triangular and rectangular elements. An alternative is to introduce auxiliary variables analogous to displacement gradients, take them as nodal degrees of freedom, and satisfy relations between the auxiliary variables and the displacement gradients (3.16) by using the Lagrange multipliers. This is akin to solving problems for incompressible materials wherein the incompressibility constraint is satisfied by using the hydrostatic pressure as a Lagrange multiplier. For strain-gradient materials, Batra [14] and Batra and Hwang [17] employed both displacements and displacement gradients as nodal variables to analyze nonlinear transient elasto-thermo-viscoplastic problems. Shu et al. [1] have investigated the performance of several two-dimensional triangular and quadrilateral elements for studying plane strain static deformations of linearly elastic strain-gradient materials. They used Hughes' [39] method of the constraint ratio to assess if an element is likely to satisfy the Babuska-Brezzi condition [40, 41, 42] that ensures the convergence of the numerical solution as the FE mesh is refined.

Thus, in order to use C^0-basis functions for plane strain problems, we use 2 displacement components and 4 auxiliary variables, β_{11}, β_{12}, β_{21}, and, β_{22}, as nodal unknowns. We set

$$\beta_{ij} = u_{i,j} \tag{3.16}$$

The higher-order strain tensor, κ_{ijk}, is written in terms of the first-order derivatives of β_{ij}

as:

$$\kappa_{ijk} = \frac{\partial \epsilon_{ij}}{\partial k} = \frac{1}{2}(\beta_{ij,k} + \beta_{ji,k}) \tag{3.17}$$

We use four Lagrange multipliers (Λ_{ij}) to satisfy the kinematic constraint of Eq.(3.16) and augment the potential energy Π given by Eq. (3.5) as follows.

$$\Pi^* = \Pi - \int_\Omega \Lambda_{ij}(\beta_{ij} - u_{i,j})dV \tag{3.18}$$

where dV is the volume element in Ω. Noting that admissible displacement fields for finding the stationary points of Π^* only have to be C^0- continuous, and in the absence of body forces (b_i) and line forces (p_i), we obtain

$$\delta\Pi^* = \int_\Omega \frac{1}{2}\left(\sigma_{ij}\left(\delta u_{i,j} + \delta u_{j,i}\right) + \tau_{ijk}\left(\delta\beta_{ij,k} + \delta\beta_{ji,k}\right)\right) dV - \int_{\partial\Omega}\left(t_i\delta u_i + r_i\delta\beta_{ij}n_j\right) dA$$
$$- \int_\Omega \Lambda_{ij}(\delta\beta_{ij} - \delta u_{i,j})dV - \int_\Omega \delta\Lambda_{ij}(\beta_{ij} - u_{i,j})dV = 0 \tag{3.19}$$

where dA is the area element on $\partial\Omega$.

Finite element basis/shape functions:

The FE shape functions are restrictions of the FE basis functions to an element. The FE basis functions can be obtained by patching together shape functions for elements meeting at a node. Thus, it suffices to discuss the FE shape functions that depend upon the number of nodes and their locations on an element.

In this work, we investigate the performance of three quadrilateral elements, $QU34L4$, $QU34L16$, and $QU48L32$ depicted in Fig. 3.2. We follow Shu et al.'s [1] terminology,

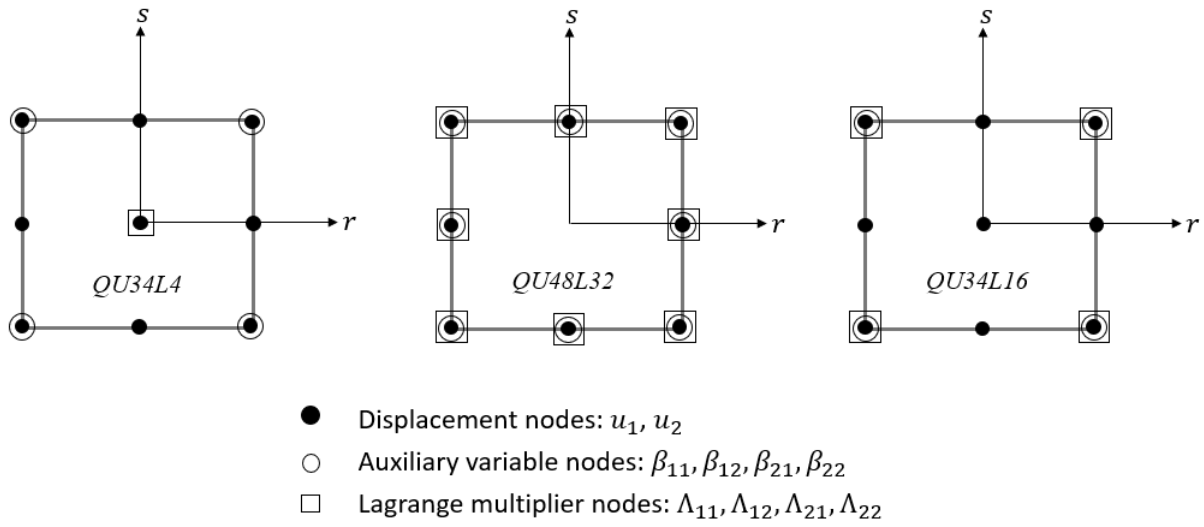

Figure 3.2: Sketch of $QU34L4$, $QU34L16$ and $QU48L32$ finite elements. $QU34L16$ and $QU48L32$ FEs were studied by Shu et al. [1]

i.e., 'Q' stands for Quadrilateral, the number following 'U' signifies the total number of kinematic variables ($u_i's$ *and* $\beta_{ij}'s$) as nodal DoFs, the number following 'L' equals the total number of Lagrange multipliers as nodal DoFs. Thus, the element $QU34L4$ has a total of 34 displacement and displacement gradient components as DoFs, and a total of 4 Lagrange multipliers ($\Lambda_{ij}'s$) as DoFs.

We generate shape functions on a 2×2 master element using local coordinates (r, s) with $-1 \leq r \leq 1$, and $-1 \leq s \leq 1$. For element $QU34L4$ depicted in Fig. 3.2, there are six DoFs, u_1, u_2, β_{11}, β_{12}, β_{21} and β_{22}, at each corner node, two DoFs, u_1 and u_2, at each of the remaining five nodes, and four Lagrange multipliers, Λ_{11}, Λ_{12}, Λ_{21} and Λ_{22} at the centroidal node resulting in a total of 38 unknowns for the element. In a $QU34L16$ element, the four Lagrange multipliers, Λ_{11}, Λ_{12}, Λ_{21} and Λ_{22}, are nodal DoFs at the four corner nodes making the total number of unknowns as 50. For the element $QU48L32$ having no node at the centroid, all u_i, β_{ij} and Λ_{ij} are taken as unknowns at each of the 8 nodes giving rise to 80 unknowns.

We divide the region of interest into disjoint either 9-noded (for $QU34L4$ and $QU34L16$) or 8-noded serendipity ($QU48L32$) elements. A function defined on an element, e, is expressed in terms of its values at the nodes as:

$$u_i^e(x_1(r,s), x_2(r,s)) = \sum_{a=1}^{n} d_i^a \mathbb{N}_u^a(r,s) \tag{3.20a}$$

$$\beta_{ij}^e(x_1(r,s), x_2(r,s)) = \sum_{a=1}^{m} w_{ij}^a \aleph_\beta^a(r,s) \tag{3.20b}$$

$$\Lambda_{ij}^e(x_1(r,s), x_2(r,s)) = \sum_{a=1}^{p} g_{ij}^a N_\Lambda^a(r,s) \tag{3.20c}$$

$$T_e : \left[x_1 = \sum_{a=1}^{n} x_1^a \mathbb{N}^a(r,s),\ x_2 = \sum_{a=1}^{n} x_2^a \mathbb{N}^a(r,s) \right] \tag{3.20d}$$

where d_i^a, w_{ij}^a, and g_{ij}^a are the approximate solution for u_i, β_{ij}, and Λ_{ij} respectively at node a, $\mathbb{N}_u, \aleph_\beta$, and N_Λ represent the shape functions for displacements (u_i), displacement gradients (β_{ij}), and Lagrange multipliers (Λ_{ij}), respectively, defined on a master quadrilateral element Ω_M. The map T_e defined by Eq. (3.20d) links points in Ω_e to those in Ω_M and vice-versa. n, m and p represent the respective number of shape functions for u_i, β_{ij} and Λ_{ij}, respectively, for the considered element-type. The respective values of n, m and p for the three element types are given in Appendix A.4. Expressions for the shape functions are given in several books; e.g., see Hughes [39], and also listed in Appendix A.4.

The expression for $\delta\Pi^*$ given in Eq.(3.19) equals the sum of integrals over each element. By substituting for u_i, β_{ij} and Λ_{ij} using Eq.(3.20) into Eq.(3.19) and writing each integral on the right-hand side of Eq. (3.19) as the sum of integrals over each FE Ω_e, we obtain:

$$\delta\Pi^* = \sum_e \left[\int_{\Omega^e} \sigma_{ij} \mathbb{N}^n_{,j} \delta d^n_i dA + g^p_{ij} \int_{\Omega^e} N^p \mathbb{N}^n_{,j} \delta d^n_i dA - \int_{\partial\Omega^e} t^e_i \mathbb{N}^n \delta d^n_i dl \quad + \int_{\Omega^e} \tau_{ijk} \aleph^m_{,k} \delta w^m_{ij} dA \right]$$
$$- \sum_e \left[\int_{\Omega^e} g^p_{ij} N^p \aleph^m \delta w^m_{ij} dA \quad + \int_{\partial\Omega^e} r^e_i n^e_j \aleph^m \delta w^m_{ij} dl + \int_{\Omega^e} \left(w^m_{ij} \aleph^m - d^n_i \mathbb{N}^n_{,j} \right) N^p \delta g^p_{ij} dA \right] = 0 \tag{3.21}$$

where dA is the vector area element on Ω^e and dl is the vector line element on $\partial\Omega^e$. Since the above equation should hold for arbitrary δd_i, δw_{ij}, and δg_{ij}, thus exploiting the arbitrariness of δd_i, δw_{ij}, and δg_{ij}, we collect their respective terms and arrive at the following set of simultaneous equations:

$$\sum_e \left[\int_{\Omega^e} \sigma_{ij} \mathbb{N}^n_{,j} dA + g^p_{ij} \int_{\Omega^e} N^p \mathbb{N}^n_{,j} dA \right] = \sum_e \left[\int_{\partial\Omega^e} t^e_i \mathbb{N}^n dl \right] \tag{3.22a}$$

$$\sum_e \left[\int_{\Omega^e} \tau_{ijk} \aleph^m_{,k} dA - g^p_{ij} \int_{\Omega^e} N^p \aleph^m dA \right] = \sum_e \left[\int_{\partial\Omega^e} r^e_i n^e_j \aleph^m dl \right] \tag{3.22b}$$

$$\sum_e \left[\int_{\Omega^e} N^p \left(w^m_{ij} \aleph^m - d^n_i \mathbb{N}^n_j \right) dA \right] = 0 \tag{3.22c}$$

In the FEM, we write the stress-strain relations in matrix form by defining the classical and higher-order stresses and strains as vectors to ease the process of writing a FE code. Thus, for isotropic materials, we have:

$$\begin{gathered}\boldsymbol{\sigma} = \boldsymbol{D}\boldsymbol{\epsilon} \\ \text{where } \boldsymbol{\sigma} = \{\sigma_{11}, \sigma_{22}, \sigma_{12}\}^T \\ \text{and } \boldsymbol{\epsilon} = \{\epsilon_{11}, \epsilon_{22}, 2\epsilon_{12}\}^T \\ \boldsymbol{\tau} = \overline{\boldsymbol{D}}\boldsymbol{\kappa} \\ \text{where } \boldsymbol{\tau} = \{\tau_{111}, \tau_{112}, \tau_{221}, \tau_{222}, \tau_{211}, \tau_{212}\}^T \\ \text{and } \boldsymbol{\kappa} = \{\kappa_{111}, \kappa_{112}, \kappa_{221}, \kappa_{222}, 2\kappa_{211}, 2\kappa_{212}\}^T\end{gathered} \tag{3.23}$$

where the material matrices $\boldsymbol{D}$ (3×3) and $\overline{\boldsymbol{D}}$ (6×6), obtained using Eq.(3.10), can be written as:

$$\boldsymbol{D} = \begin{bmatrix} \lambda + 2\mu & \lambda & 0 \\ \lambda & \lambda + 2\mu & 0 \\ 0 & 0 & \mu \end{bmatrix} \tag{3.24}$$

$$\overline{\boldsymbol{D}} = l_c^2 \begin{bmatrix} \lambda + 2\mu & 0 & \lambda & 0 & 0 & 0 \\ 0 & \lambda + 2\mu & 0 & \lambda & 0 & 0 \\ \lambda & 0 & \lambda + 2\mu & 0 & 0 & 0 \\ 0 & \lambda & 0 & \lambda + 2\mu & 0 & 0 \\ 0 & 0 & 0 & 0 & \mu & 0 \\ 0 & 0 & 0 & 0 & 0 & \mu \end{bmatrix} \tag{3.25}$$

Substituting for classical (σ_{ij}) and higher-order stresses (κ_{ijk}) in terms of strains and strain-gradients from the constitutive relation in Eq.(3.23) and then for u_i, β_{ij} and Λ_{ij} in terms of their nodal values, we arrive at a set of linear simultaneous algebraic equations which can be written in the matrix form as:

$$\boldsymbol{K}_g\,\boldsymbol{U} = \boldsymbol{F}_g$$

$$\text{where } \boldsymbol{K}_g = \begin{bmatrix} \boldsymbol{K} & \boldsymbol{0} & \boldsymbol{A}^T \\ \boldsymbol{0} & \overline{\boldsymbol{K}} & -\boldsymbol{M}^T \\ \boldsymbol{A} & -\boldsymbol{M} & \boldsymbol{0} \end{bmatrix} \text{ and } \boldsymbol{F}_g = \begin{bmatrix} \boldsymbol{F} \\ \boldsymbol{H} \\ \boldsymbol{0} \end{bmatrix} \tag{3.26}$$

where $\boldsymbol{U} = \{\boldsymbol{d}, \boldsymbol{w}, \boldsymbol{g}\}$ is the vector of nodal unknowns, $\boldsymbol{K}_g$ is the global stiffness matrix, and $\boldsymbol{F}_g$ is the global load vector. The details about the assembly of $\boldsymbol{K}_g$ and $\boldsymbol{F}_g$ and the definition of their components are provided in Appendix A.1. In Appendix A.4, we provide the size of different element matrices in Eq. (3.26) for the three different element types. Also, note that the integrals over each element are evaluated by using 3×3 Gauss quadrature rule.

The system of simultaneous linear equations, Eq. (3.26), is solved after modifying $\boldsymbol{K}_g$ and $\boldsymbol{F}_g$ to satisfy the prescribed essential boundary conditions by using the penalty method. That is, to impose, $d_i = \bar{\beta}$, we replace K_{ii} (no sum on i) by $(K_{ii}+\gamma)$, F_i by $\bar{\beta}\gamma$ where γ is very large as compared to a typical entry in $\boldsymbol{K}_g$, and then solve the resulting system of simultaneous linear equations to obtain the numerical solution of the problem. To enforce displacement gradient-type boundary conditions in (3.7d), i.e., $w_{ij}n_j = \bar{\alpha}$, the penalty method is used.

Solution Procedure: For elements $QU34L16$ and $QU48L32$, a direct solver in MATLAB, *mldivide*, is used. For element $QU34L4$, where Lagrange multiplier is associated only with the node at the element centroid and is considered constant within an element, direct solution is not possible as the global stiffness matrix is singular even after the essential boundary conditions (Displacement type: $d_i = \bar{\beta}$ and/or Displacement-gradient type: $w_{ij}n_j = \bar{\alpha}$) have been imposed. However, the system of equations can be solved by using an iterative approach [43]. The details of the iterative procedure are given in Appendix A.5. Nodal displacements, d_i, are obtained by using *mldivide* and the nodal displacement-gradients,

w_{ij}, are determined with a minimum residual-based iterative solver, $minres$, as the stiffness matrix $\overline{K}$ is singular.

Chapter 4

Results and Discussion

4.1 Verification of the developed software

4.1.1 Verification of the code by using the method of manufactured solutions

The method of manufactured solutions (MMS) provides a way to verify if the software correctly solves the boundary-value problem (BVP) (i.e., partial differential equations (PDEs) and the associated boundary conditions (BCs)). The general procedure for the MMS is outlined below. In this exercise, we use the $Q34L16$ finite element as shown in Fig. 3.2.

- Assume analytical expressions for non-dimensional displacements, $\bar{u}_1$ and $\bar{u}_2$ in terms of non-dimensional coordinates, $\bar{x}_1$ and $\bar{x}_2$. For example, set:

$$\begin{gathered} \bar{u}_1 = \bar{x}_1^3\, \bar{x}_2^2\ ,\ \bar{u}_2 = (1-\bar{x}_1^2)\,(1-\bar{x}_2^3) \\ \text{where } \bar{x}_1 = \tfrac{x_1}{L} \text{ and } \bar{x}_2 = \tfrac{x_2}{L}, \bar{u}_1 = \tfrac{u_1}{L} \text{ and } \bar{u}_2 = \tfrac{u_2}{L} \end{gathered} \tag{4.1}$$

- Find infinitesimal strains and strain gradients from the assumed displacement field using Eq. (3.2).

- Find expressions for non-dimensional stresses, $\bar{\sigma}_{ij}$ and $\bar{\tau}_{ijk}$ from the constitutive rela-

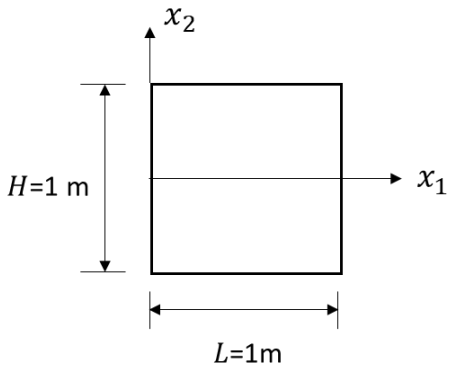

Figure 4.1: Geometric configuration of the body.

tions, Eq. (3.10), where $\bar{\sigma}_{ij} = \sigma_{ij}/E$ and $\bar{\tau}_{ijk} = \tau_{ijk}/(E\, l_c)$.

- Find body forces that are required to satisfy the equilibrium equations (3.6).
- For a rectangular beam, find classical and higher-order surface traction on all six surfaces using Eq. (3.7a) and Eq. (3.7c).
- Input the above computed traction and body forces into the FE code and apply essential boundary conditions (Eq. (3.7b) and Eq. (3.7d)) to eliminate the rigid body motion of the structure.
- Solve for displacements, displacement gradients and Lagrange multipliers.
- Compare the computed displacements, displacement-gradients, and stresses with those assumed above.
- If the computed and the assumed fields differ by more than an acceptable tolerance, then the software has bugs in it. On the other hand, even if the difference in the two fields is within the acceptable tolerance ($< 0.1\%$), there is no guarantee that the software accurately solves such BVPs. One needs to verify the software by the MMS for a large variety of BVPs to establish confidence in it and ensure its validity.

Expressions for strains, strain gradients, classical and higher-order stresses, classical traction, and higher order traction on all four surfaces, and the body forces are included in the Appendix A.3. The geometry and the coordinate axes for an example problem are shown in Fig. 4.1. We assume that the body is made of a linearly isotropic material having the following material properties:

$$E = 200\,GPa\,;\ \nu = 0.3\,;\ l_c = 2\,mm^2 \tag{4.2}$$

Table 4.1: Maximum % relative difference between the computed and the assumed MMS solution for five different meshes.

Maximum % relative difference for respective quantities	Mesh size 4×4	8×8	12×12	16×16	20×20
$\bar{u}_1$	0.34	0.10	0.09	0.089	0.088
$\bar{u}_2$	0.02	0.005	0.003	0.0028	0.0027
β_{11}	8.17	2.10	0.96	0.55	0.37
β_{12}	13.43	3.26	1.5	0.92	0.66
β_{21}	1.53	0.42	0.19	0.11	0.073
β_{22}	2.82	0.70	0.31	0.18	0.12
$\bar{\sigma}_{11}$	25.47	6.04	2.71	1.56	1.03
$\bar{\sigma}_{12}$	0.64	0.21	0.10	0.06	0.04
$\bar{\sigma}_{22}$	6.12	1.26	0.53	0.29	0.19
$\bar{\tau}_{111}$	22.22	11.91	8.09	6.12	4.92
$\bar{\tau}_{112}$	20.86	5.20	2.32	1.31	0.84
$\bar{\tau}_{121}$	9.26	5.45	3.81	2.93	2.37
$\bar{\tau}_{122}$	6.16	1.27	0.56	0.35	0.26
$\bar{\tau}_{221}$	22.23	11.90	8.08	6.11	4.91
$\bar{\tau}_{222}$	2.33	0.58	0.26	0.15	0.09

In addition to applying the computed traction and body forces, we set $\bar{u}_1 = 0$ on the edge $\bar{x}_1 = 0$ and $\bar{u}_2 = 0$ on the edge $\bar{x}_1 = 1$ as given by the assumed displacement field, Eq. (4.1). Using $Q34L16$ finite elements and four uniform FE meshes (8×8, 12×12, 16×16, and 20×20), the computed and the assumed displacements and displacement gradients on

[2] In US Customary units: $E = 2.9\times10^7\,psi\,;\ \nu = 0.3\,;\ l_c = 0.0787\,in.$

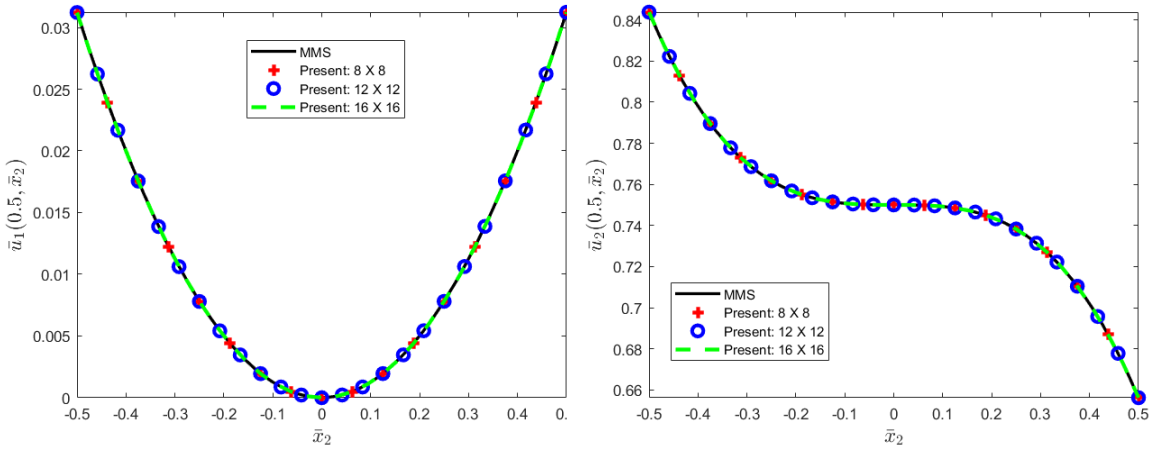

Figure 4.2: Comparison of computed and assumed (MMS) displacements on the line $\bar{x}_1 = 0.5$.

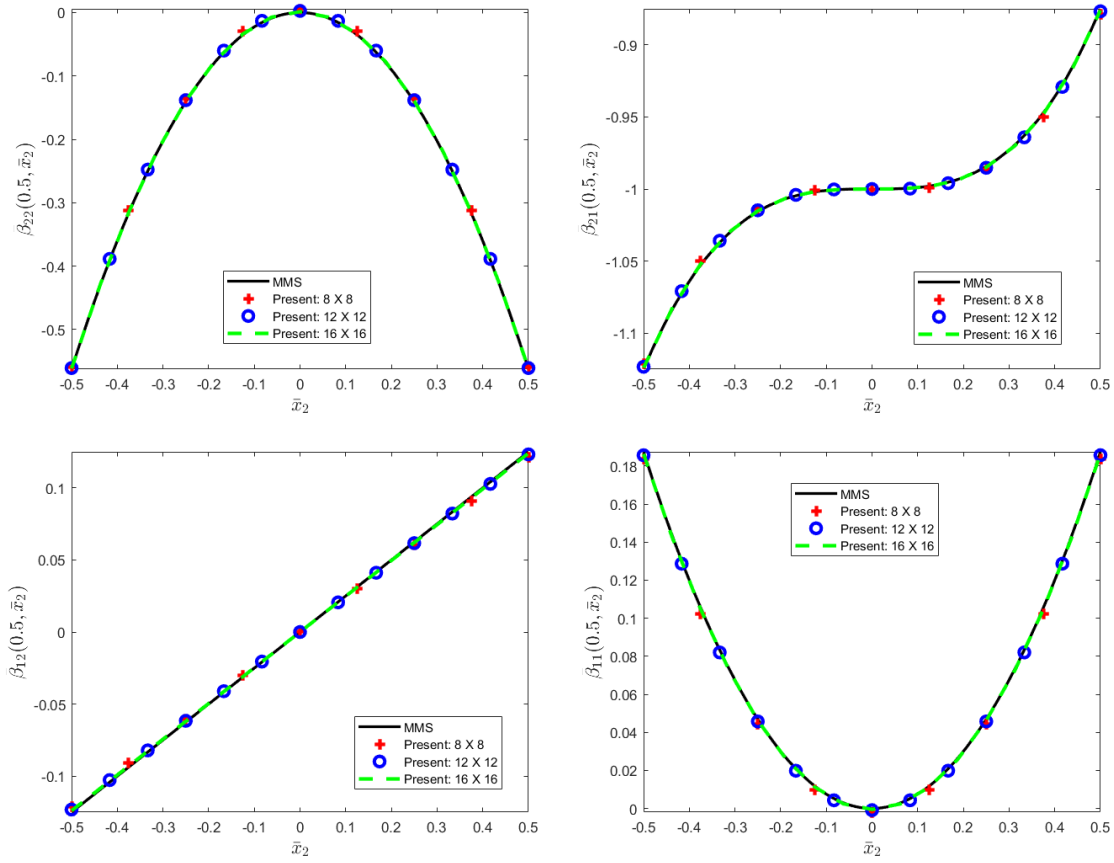

Figure 4.3: Comparison on the line $\bar{x}_1 = 0.5$ of the computed and the MMS values of displacement gradients.

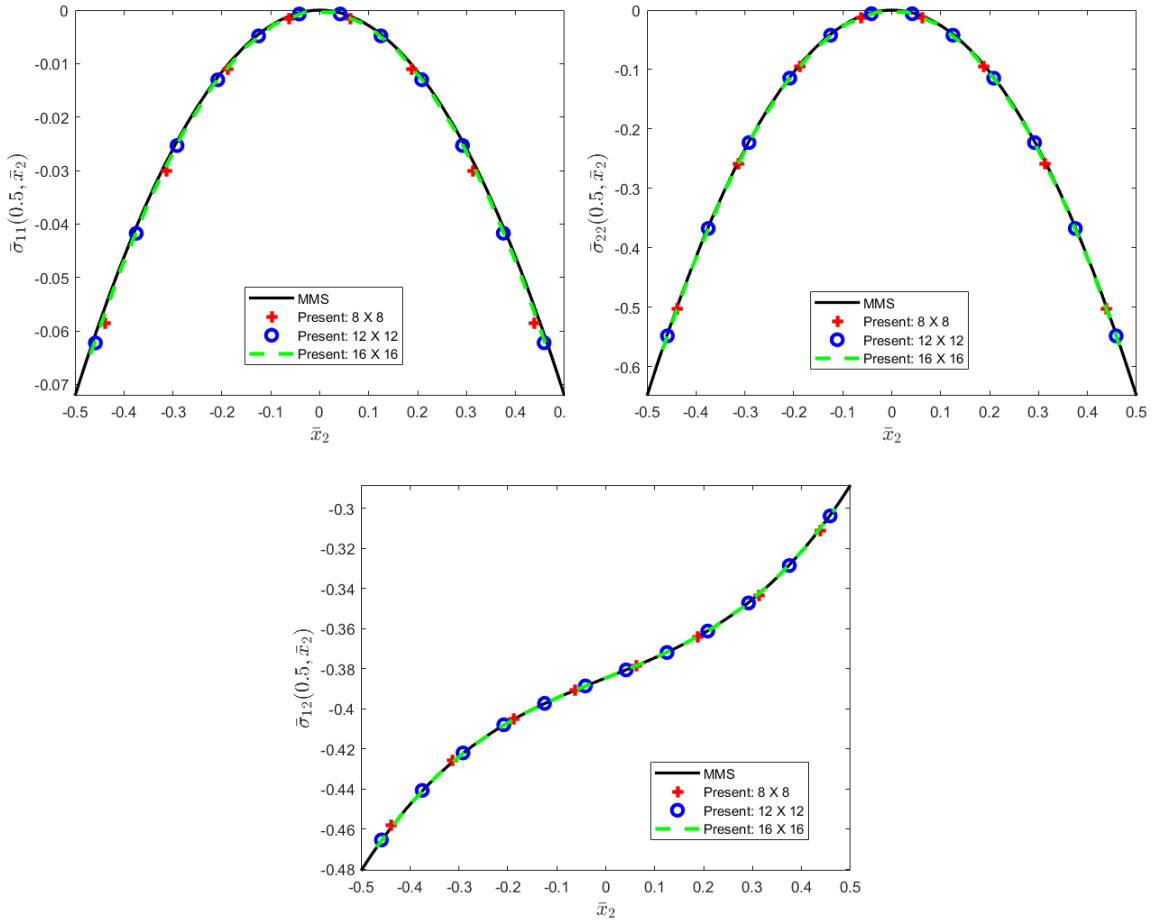

Figure 4.4: Comparison of through-the-thickness distributions of classical stresses at $\bar{x}_1 = 0.5$.

the line $\bar{x}_1 = 0.5$ are, respectively, plotted in Figs. 4.2 and 4.3. Both the displacements and displacement gradients agree well as listed in Table 4.1. The higher-order stresses exhibit slightly higher percentage relative difference due to edge effects, which arise from boundary influences, reduced element support, and numerical sensitivity in strain-gradient formulations.

We confirmed whether the kinematic constraints ($\beta_{ij} = \bar{u}_{i,j}$) are well satisfied by comparing nodal values of β_{ij} with $\bar{u}_{i,j}$'s obtained by differentiating the computed $\bar{u}_i$ with respect to $\bar{x}_j$. In Fig. 4.4 and Fig. 4.5, we have compared the distribution of the computed and the MMS

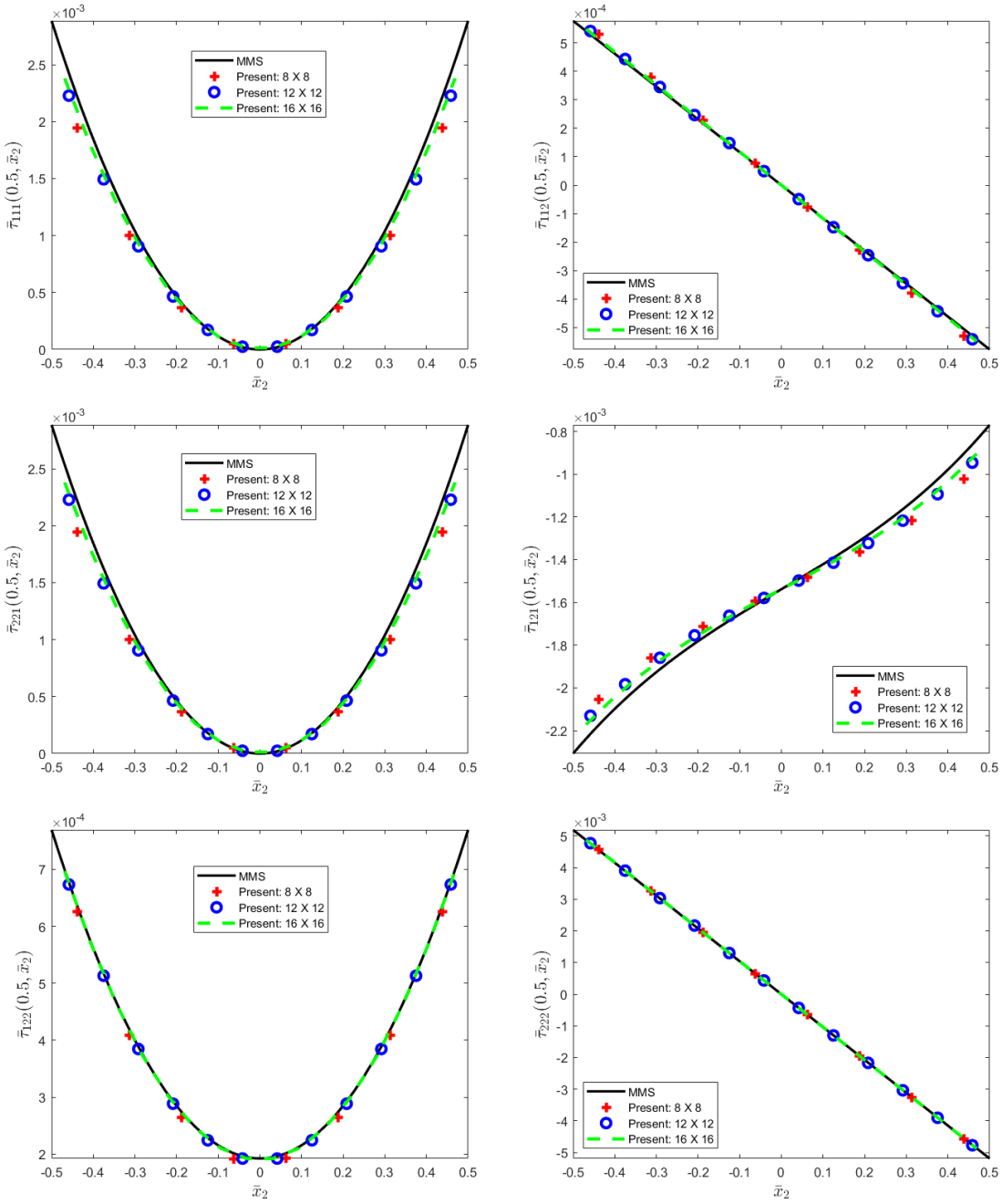

Figure 4.5: Comparison of through-the-thickness distributions of higher-order stresses at $\bar{x}_1 = 0.5$.

stress components $\bar{\sigma}_{11}, \bar{\sigma}_{22}, \bar{\tau}_{111}$ etc. on the line $\bar{x}_1 = 0.5$. The numerical solutions agree well with the manufactured solutions, especially when using a 20×20 FE mesh, as shown in Table

4.1, thus verifying the developed code. We use $\|e\|_{\text{sup}}$, which gives the maximum relative difference between the analytical and the approximate solution, to quantify the error, where $\|e\|_{\text{sup}} = \sup_{x\in\Omega} \frac{|\theta_{\text{anal}}-\theta_{\text{num}}|}{|\theta_{\text{anal}}|}$.

In Fig. 4.6, we compare the performance of three elements $QU34L4$, $QU34L16$, and $QU48L32$. We have plotted the comparison of computed results using three different elements $QU34L4$ (40×40), $QU34L16$ (12×12), and $QU48L32$ (12×12) for the problem considered in the MMS. We observe that the elements $QU34L16$ (*green curve*) and $QU48L32$ (*red curve*), perform very well for a 12×12 mesh, whereas element $QU34L4$ (*blue curve*) is not able to capture the displacement-gradients well even for the fine mesh.

4.1.2 Plane strain deformation of a clamped-clamped transversely isotropic beam

To further verify the developed software, we compare the presently computed results with those of Vel and Batra [44] who used the Eshelby-Stroh formalism to study plane strain deformations of a clamped-clamped transversely isotropic classical beam subjected to a sinusoidal distributed normal traction, ($t_2 = -q_0 \sin(\pi x_1/L)$), on the top surface as shown in Fig. 4.7. The following values of material parameters are used:

$$\frac{E_1}{E_2} = 25\,;\ \frac{G_{12}}{E_2} = 0.5\,;\ v_{12} = 0.25\,;\ E_2 = 4\,GPa^{3}\,;\ l_c = 0\,mm \tag{4.3}$$

We use the ($n_1 \times n_2 = 50 \times 24$) non-uniform Chebyshev-Gauss-Lobatto grid [45] on the

[3] In US Customary units: $E_2 = 5.8 \times 10^5\ psi$.

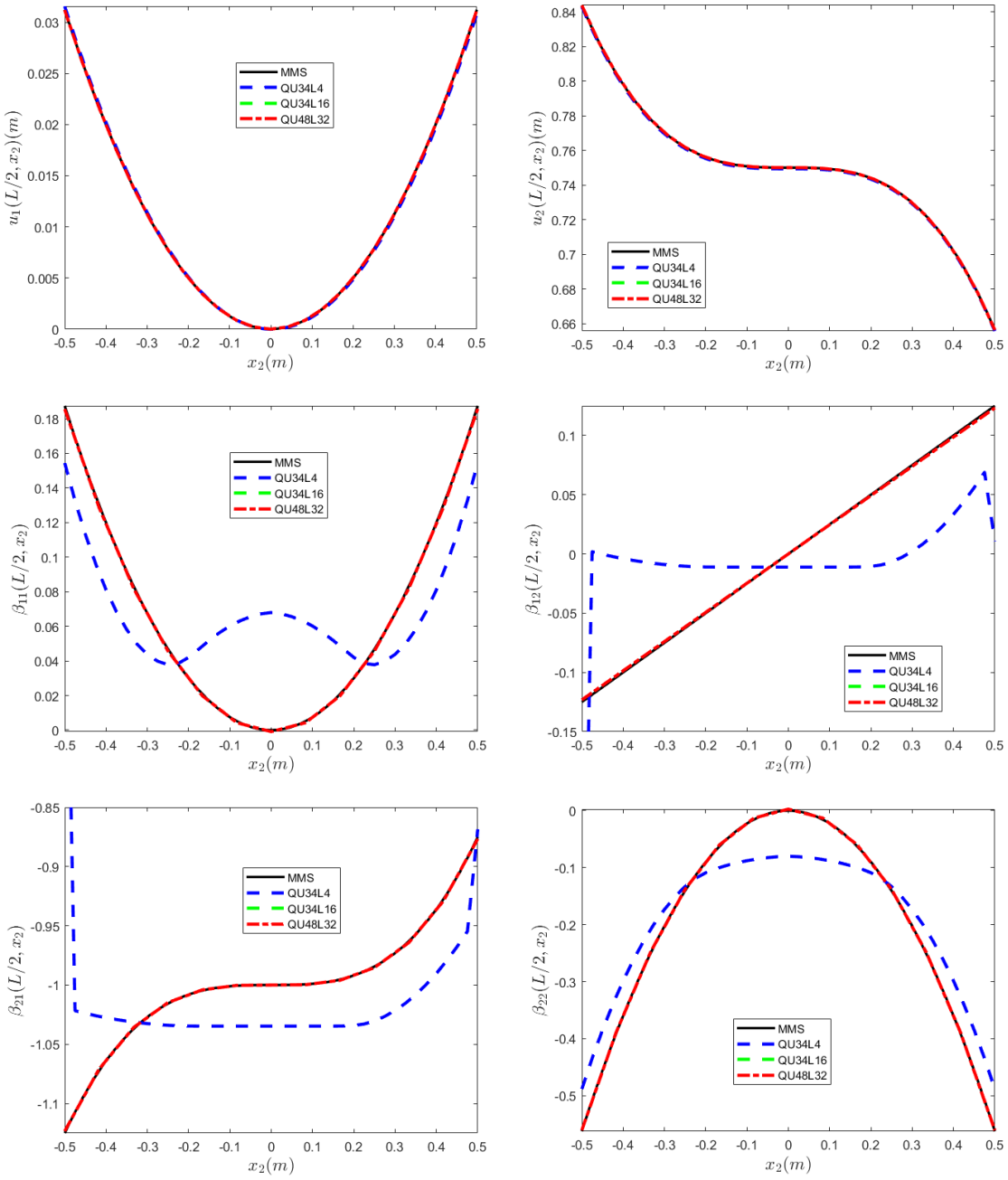

Figure 4.6: Comparison of the MMS solution with the computed results using three different elements $QU34L4$ (40×40), $QU34L16$ (12×12), and $QU48L32$ (12×12).

beam's domain $\Omega : (x_1 : [0, L])(x_2 : [0, H])$ with nodal locations given by:

$$x_1^i = \frac{L}{2}\left[1 - \cos\left(\frac{i-1}{n_1 - 1}\pi\right)\right] \; ; \; x_2^j = \frac{H}{2}\left[1 - \cos\left(\frac{j-1}{n_2 - 1}\pi\right)\right] \tag{4.4}$$

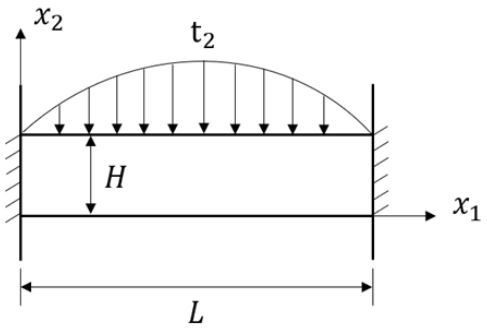

Figure 4.7: Sketch of the beam problem with sinusoidal load on the top surface.

where $i = 1, \ldots, n_1$ and $j = 1, \ldots, n_2$. Table 4.2 shows that as we refine the mesh, the % relative difference for non-dimensional displacement $\left(\bar{u}_2 = \frac{100E_2H^3}{q_0L^4}u_2\right)$ and displacement gradients $\left(\bar{\beta}_{ij} = \frac{100E_2H^3}{q_0L^3}\beta_{ij}\right)$ reaches $< 0.1\%$.

Table 4.2: % Relative difference between the computed results with varying mesh size for non-dimensional displacement and displacement gradients for the case L/H=4.

	Mesh size			
Quantity	20×10	30×20	40×20	50×24
$\bar{u}_2$	-1.4828	-1.4894	-1.4916	-1.4927
% Diff	-	0.45	0.15	0.074
β_{11}	0.0088	0.0087	0.0086	0.0086
% Diff	-	1.15	1.14	0
β_{21}	4.3134	4.3241	4.3248	4.3254
% Diff	-	0.25	0.016	0.014
β_{22}	-0.7208	-0.7191	-0.7184	-0.7181
% Diff	-	0.24	0.097	0.042

For $L/H = 4$, 10 and 20, we have compared in Fig. 4.8 the presently computed deflection profile of the beam's mid-surface with that of Vel and Batra [44]. The maximum difference between the two results is about 0.13% for $L/H = 4$ at $x_1/L = 0.5$. Besides, the through-the-thickness variations of the normalized axial and shear stress at different locations for a beam with $L/H = 4$ are plotted in Fig. 4.9. It is observed that the maximum difference between the two sets of results is approximately 1.95% for the shear stress σ_{12} at $x_1/L = 0.05$. One

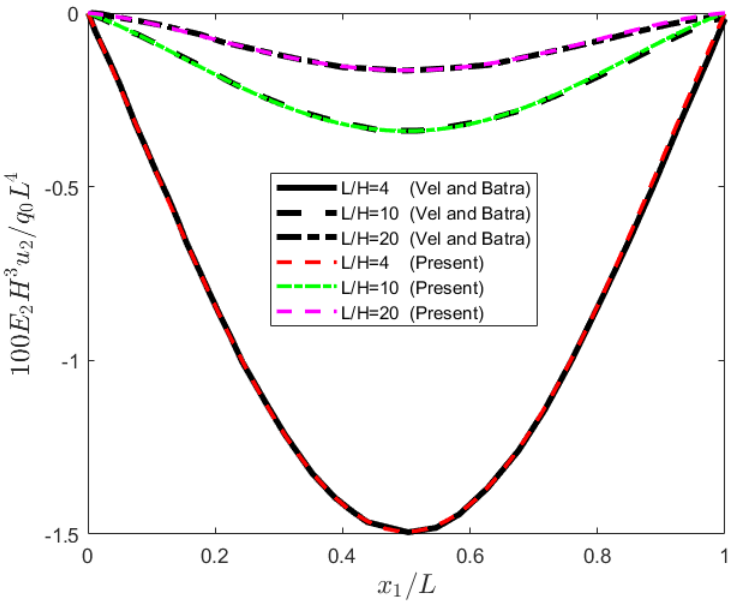

Figure 4.8: Non-dimensional deformed shapes of the mid-surface for $L/H = 4$, 10 and 20.

reason for getting reasonably accurate values of the transverse shear stress σ_{12} is that we are also taking displacement gradients as nodal DoFs and these are used to compute the stresses.

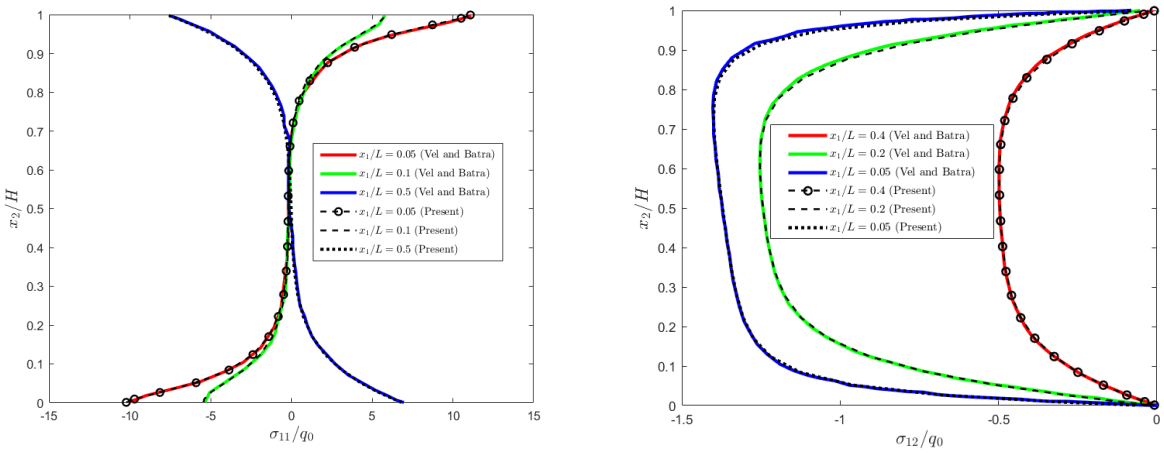

Figure 4.9: For the beam with $(L/H = 4)$, through-the-thickness distributions of the non-dimensional axial and shear stresses at different locations.

4.2 Numerical Examples

We now present results for plane strain deformations of several problems numerically analyzed with the developed software.

4.2.1 An isotropic cantilever beam under a uniform tangential traction

This example problem involves a cantilever beam, shown in Fig. 4.10 , under a uniform tangential traction at the unclamped edge that has the following boundary conditions on the four bounding surfaces:

$$
\begin{aligned}
&\underline{x_1 = 0}: \\
&u_1 = u_2 = 0, \quad u_{1,1} = u_{2,1} = 0 \\
&\underline{x_1 = L\ [\vec{\boldsymbol{n}} = (1,0)]}: \\
&t_1 = \sigma_{11} - \tau_{121,2} - \tau_{112,2} - \tau_{111,1} = 0 \\
&t_2 = \sigma_{12} - \tau_{121,1} - \tau_{122,2} - \tau_{221,2} = -P_0 \text{ where } P_0 = 100\ MPa^{4} \\
&r_1 = \tau_{111} = 0\ ;\ r_2 = \tau_{211} = 0 \\
&\underline{x_2 = \pm\tfrac{H}{2}\ [\vec{\boldsymbol{n}} = (0,\pm 1)]}: \\
&t_1 = \sigma_{12} - \tau_{121,1} - \tau_{122,2} - \tau_{112,1} = 0 \\
&t_2 = \sigma_{22} - \tau_{221,1} - \tau_{222,2} - \tau_{212,1} = 0 \\
&r_1 = \tau_{122} = 0\ ;\ r_2 = \tau_{222} = 0
\end{aligned}
\tag{4.5}
$$

We consider an isotropic material with the following properties:

$$
E = 200\ GPa,\ \nu = 0.3,\ l_c = 0,\ 2,\ 6, \text{and } 10\ mm^{4} \tag{4.6}
$$

[4] In US Customary units: $P_0 = 1.45 \times 10^4 psi; E = 2.9 \times 10^7 psi; \nu = 0.3; l_c = 0,\ 0.079,\ 0.236, \text{and} 0.394\ in.$

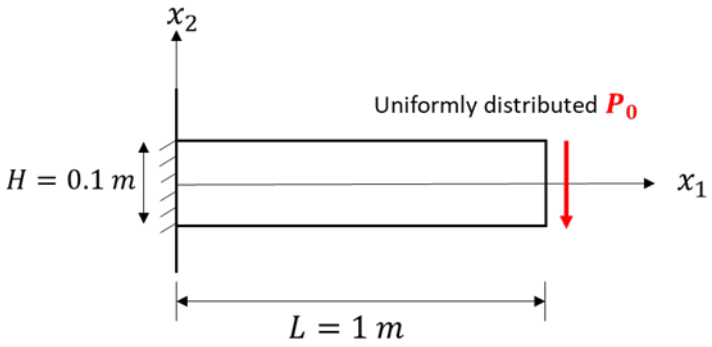

Figure 4.10: Sketch of the beam under a uniform shear traction at the right edge.

Table 4.3: Deflections at the tip of the mid-surface of the beam for different values of l_c.

$l_c(mm)$[5]	$u_2^{tip}(m)$	% Change from u_2 for $l_c = 0$
0	-0.1813	–
2	-0.1801	0.71
6	-0.1720	5.33
10	-0.1586	12.71

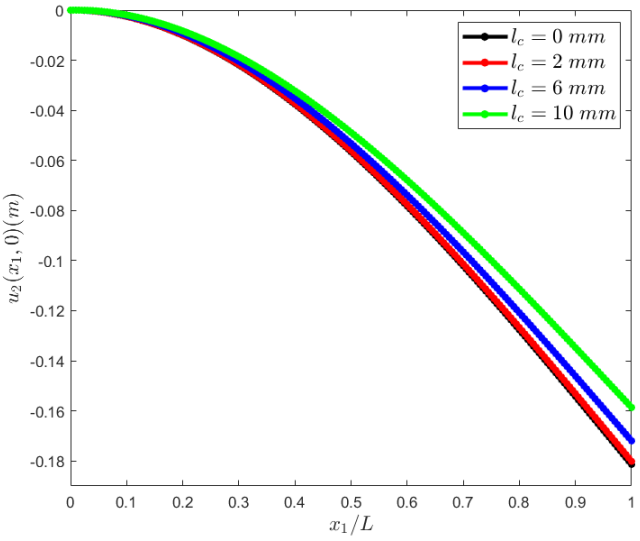

Figure 4.11: For $l_c = 0$, 2, 6, and 10 mm, deformed mid-surfaces of the clamped beam.

[5]For US Customary units: $1\,mm = 0.0394\,in$

In each case, the results are computed for 4 values of the characteristic length l_c, with the beam discretized by a uniform 100×20 FE mesh.

In Fig. 4.11, we have depicted deformed shapes of the mid-surface of the beam and values of the deflection at the right end of the mid-surface are provided in Table 4.3. It is clear that the magnitude of the deflection decreases with an increase in l_c implying that the overall beam stiffness increases with an increase in l_c.

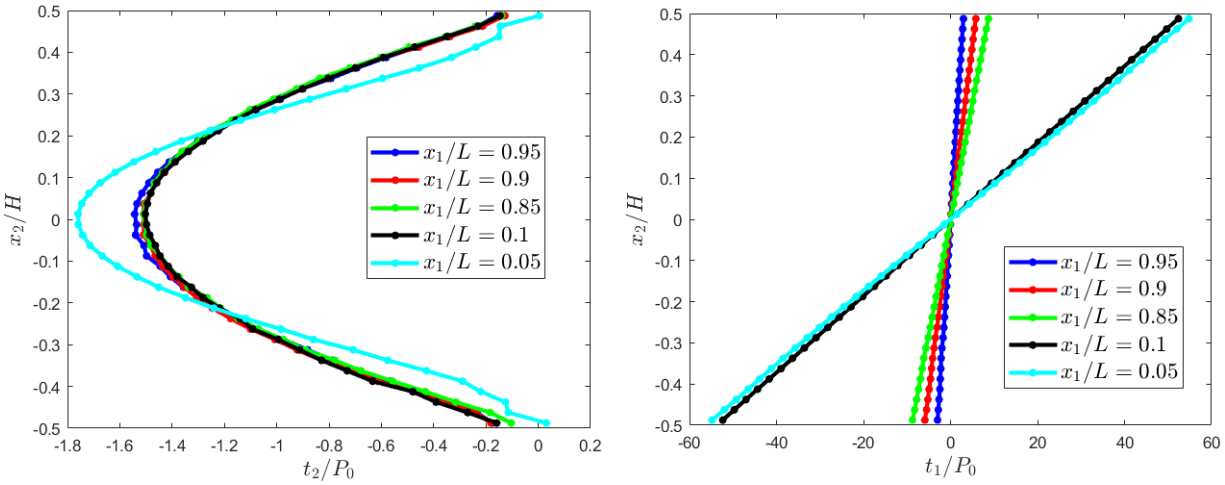

Figure 4.12: Through-the-thickness distributions of non-dimensional surface traction t_1 and t_2 at different values of x_1/L.

In Fig. 4.12, we plot through-the-thickness distributions of non-dimensional surface traction t_1/P_0 and t_2/P_0 at different values of x_1/L. Classical surface traction t_1 and t_2 are negligible near the top and the bottom surfaces for all values of x_1/L thus satisfying the boundary conditions, Eq. (4.5). In Fig. 4.13, we have plotted the axial distribution of non-dimensional surface traction t_1/P_0 and t_2/P_0 at different values of x_2/H. Clearly, t_1/P_0 is zero at the right edge where t_2/P_0 approaches 1. Also note that the t_1/P_0 is larger in magnitude near the top and bottom surfaces ($x_2/H = \pm 0.425$) as compared to the mid-surface ($x_2/H = \pm 0.025$). The distribution of t_2/P_0 is symmetric about the mid-surface hence red-green ($x_2/H = \pm 0.425$) curves coincide and blue-black ($x_2/H = \pm 0.025$) curves coincide.

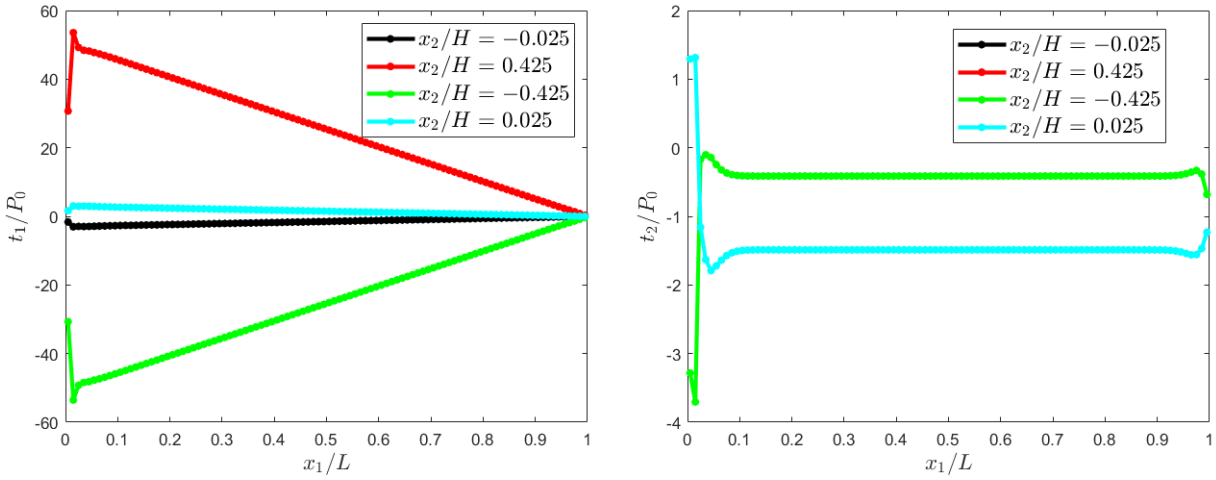

Figure 4.13: Axial distribution of non-dimensional surface traction t_1 and t_2 at different values of x_2/H.

In Fig. 4.12 (left), the curve corresponding to $x_1/L = 0.05$ shows a noticeable deviation from the other curves. This behavior can be attributed to edge effects, where the stress distribution is influenced by proximity to the boundary. The reduced support from neighboring elements and the imposition of boundary conditions contribute to a distinct traction response in this region. Furthermore, the strain gradient effects are more pronounced near the edges, leading to increased numerical sensitivity and higher-order stress variations. Similar behavior is observed in Fig. 4.13 near the left boundary ($x_1/L = 0$), especially near the corners ($x_1/L = 0, x_2/H = \pm 0.425$).

Using Eq. (3.7a) surface traction t_1 and t_2, and higher-order surface traction r_1 and r_2 at $x_2 = -0.025H$ computed on the transverse cross-sections $X_1 =$ constant with $\vec{\boldsymbol{n}} = (1, 0)$ are plotted in Fig. 4.14. Nearly zero values of t_1, r_1 and r_2 at the right end $x_1/L = 1$ indicate that the traction boundary conditions prescribed there are well satisfied. Besides, $t_2/P_0 \sim -1$ at $x_1/L = 1$ with the corresponding applied traction ($-P_0 = 100\ MPa$). Note that for the classical beam theory ($l_c = 0\ mm$), $r_1 = r_2 = 0$, and t_1 and t_2, respectively, equal the axial stress σ_{11} and the shear stress σ_{12}.

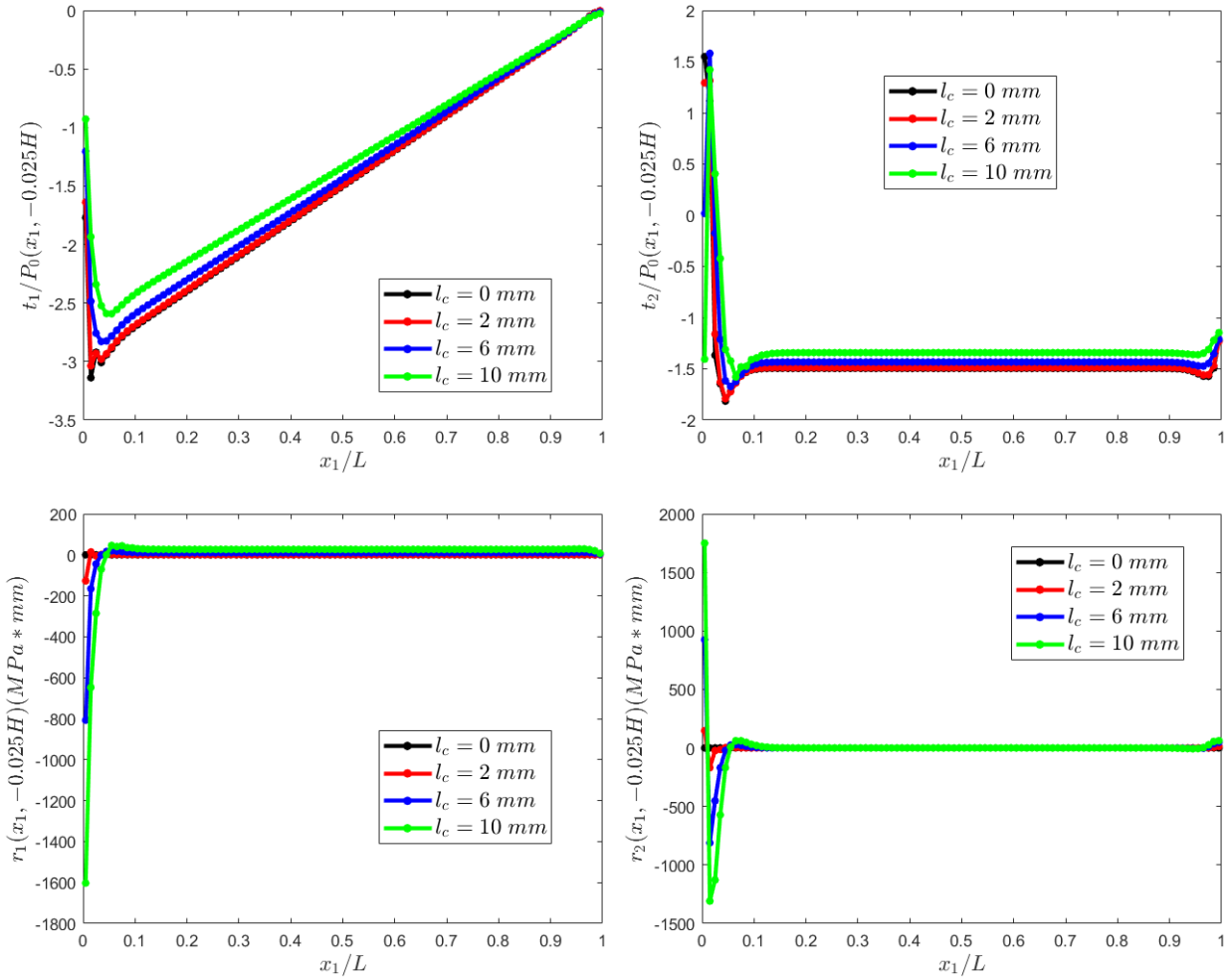

Figure 4.14: Variations on planes X_1 = constant of t_1, t_2, r_1 and r_2 at the point $x_2 = -0.025H$.

The maximum value of t_1 occurs at a point slightly away from the clamped edge. This differs from that for a Euler-Bernoulli beam for which the maximum magnitude of t_1 occurs at the clamped edge. Except at points within $0.2L$ of the clamped edge, t_1 is nearly uniform over the beam span and its value, independent of l_c, is close to zero because the point $x_2 = -0.025H$ is close to the neutral surface, $x_2 = 0$. Near the clamped edge, variations with x_1 of both t_1 and t_2 exhibit boundary layers that are more dominant for t_2.

Effect of beam thickness

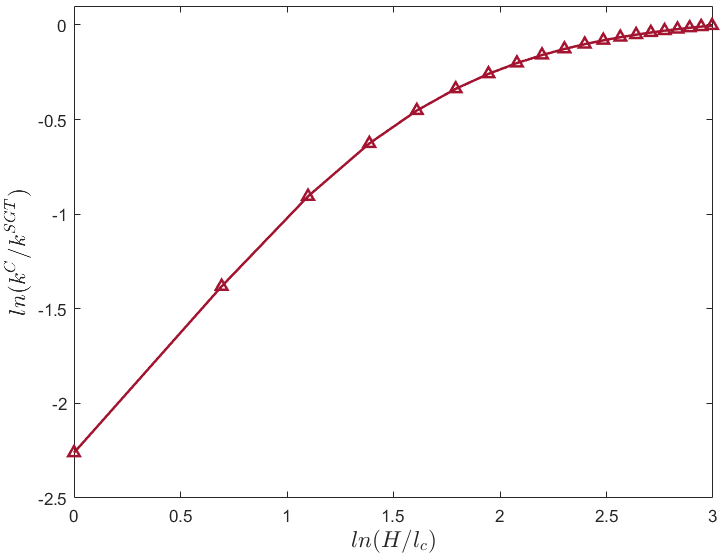

Figure 4.15: The logarithm of the ratio of stiffness versus the logarithm of H/l_c.

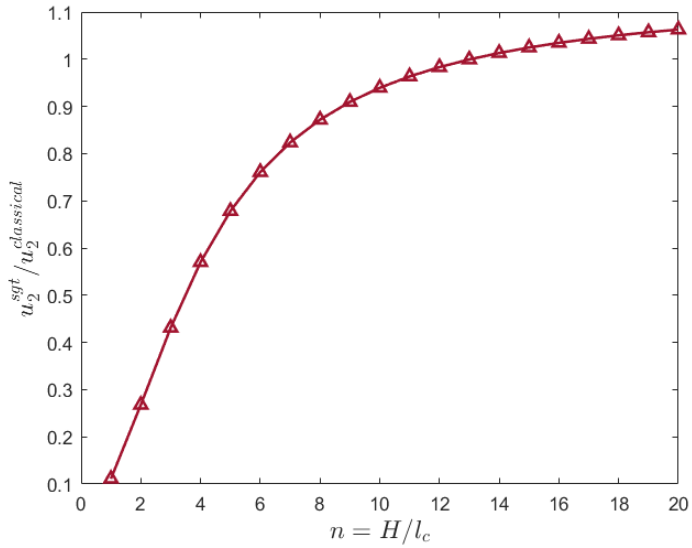

Figure 4.16: The non-dimensional deflection versus H/l_c.

In this exercise, we consider a strain-gradient beam made of an isotropic material with $l_c = 0.1\ mm$ and satisfying the boundary conditions listed in Eq. (4.5). In Fig. 4.15, we have presented the logarithm plot of the ratio of stiffness-es from classical ($k^{\mathrm{C}} = \frac{EH^3}{4L^3}$) and

the strain-gradient ($k^{\text{SGT}} = \frac{P}{\delta_{tip}}$) solution versus H/l_c. As we keep l_c fixed and increase $n = H/l_c$, the size of the beam increases and the difference between the classical and the strain-gradient solution decreases. A similar conclusion can be derived from Fig. 4.16 where we plot the ratio of the vertical deflection of the mid-surface tip for the strain-gradient (u_2^{sgt}) and the classical theory $\left(u_2^{classical} = PL^3\left(1-\nu^2\right)/3EI\right)$ [46] versus H/l_c.

4.2.2 An isotropic and a transversely isotropic cantilever beam under a tangential traction at the unclamped edge

This example problem involves a cantilever beam, shown in Fig. 4.17, under a parabolic tangential traction at the unclamped edge that has the following boundary conditions on the four bounding surfaces. The axis of transverse isotropy coincides with the x_1-axis.

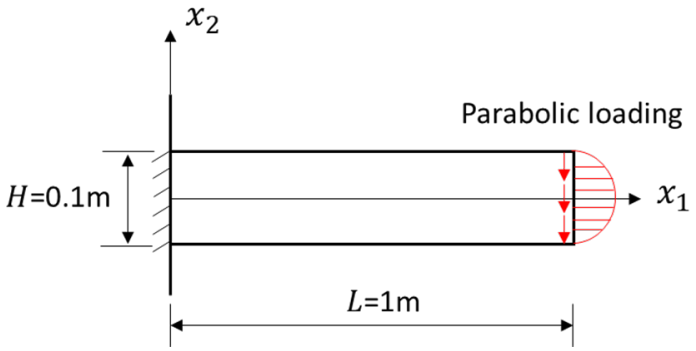

Figure 4.17: Sketch of the beam under a parabolic shear traction at the right edge.

$$
\begin{aligned}
&x_2 = \pm\tfrac{H}{2}: \quad t_1 = t_2 = 0, \quad r_1 = r_2 = 0 \\
&x_1 = 0: \quad u_1 = u_2 = 0, \quad u_{1,1} = u_{2,1} = 0 \\
&x_1 = L: t_1 = 0, r_1 = r_2 = 0, t_2 = -\tfrac{3}{2H}\left(1 - \left(\tfrac{2x_2}{H}\right)^2\right) P \text{ and } P = 10\ MPa^6
\end{aligned}
\tag{4.7}
$$

[6] In US Customary units: $P = 1.45 \times 10^3\ psi$.

For the isotropic material, we take:

$$E = 200\ GPa,\ \nu = 0.3,\ l_c = 0,\ 2,\ 4,\ 6,\ 8, \text{and } 10\ mm^{7} \tag{4.8}$$

and for the transversely isotropic material with the axis of transverse isotropy along the x_1-axis, we set:

$$\frac{E_1}{E_2} = 25\ ;\ \frac{G_{12}}{E_2} = 0.5\ ;\ \nu_{12} = 0.25\ ;\ E_2 = 4\,GPa\,^{7};\ l_c = 0,\ 2,\ 6,\ 8,\ 10\,mm \tag{4.9}$$

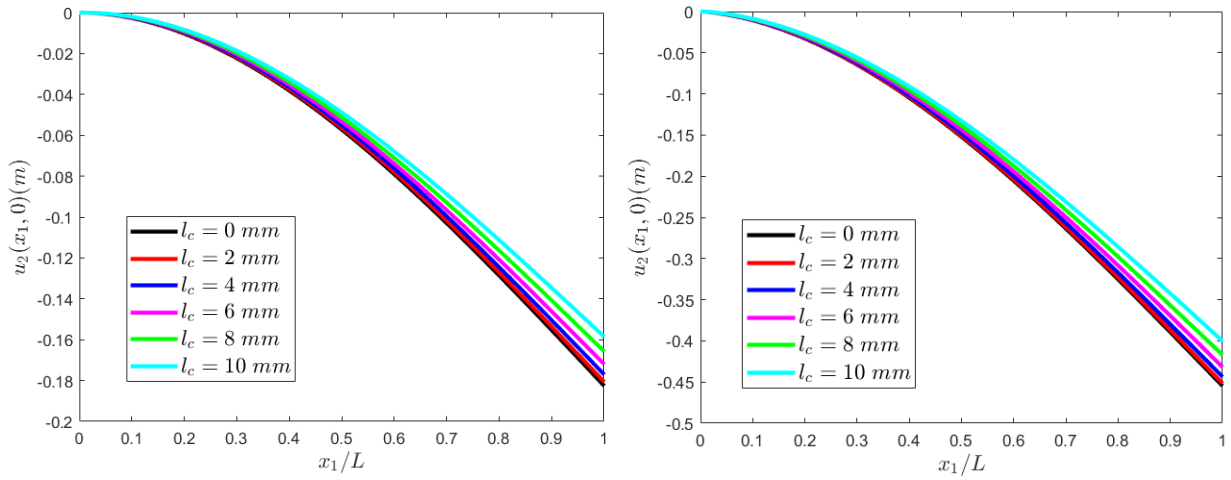

Figure 4.18: Deflections of the mid-surface of the beam for different values of the characteristic length; (left) isotropic, and (right) transversely isotropic material.

In each case results are computed for six values of the characteristic length, l_c with the beam discretized by a uniform 100×12 FE mesh.

In Fig. 4.18, we have depicted deformed shapes of the mid-surface of the beam and values of the deflection at the right end of the mid-surface are provided in Table 4.4. It is clear that

[7] In US Customary units: $E = 2.9 \times 10^7\ psi$; $l_c = 0,\ 0.079,\ 0.236,\ 0.315, \text{and } 0.394\ in$; $E_2 = 5.8 \times 10^5\ psi$.

Table 4.4: For isotropic and transversely isotropic material beams with the axis of transverse isotropy along the beam axis, deflections at the tip of the mid-surface of the beam for different values of l_c. [Analytical solution for isotropic material beam and $l_c = 0$: $u_2(m) = -0.201$]

$l_c(mm)$	$u_2(m)$ (isotropic)	$u_2(m)$ (transversely isotropic)	% Change (isotropic) from u_2 for $l_c = 0$	% Change (transversely isotropic) from u_2 for $l_c = 0$
0	-0.1818	-0.4568	–	–
2	-0.1805	-0.4537	0.71	0.69
4	-0.1771	-0.4454	2.58	2.51
6	-0.1721	-0.4333	5.33	5.15
8	-0.1659	-0.4184	8.76	8.41
10	-0.1587	-0.4015	12.71	12.11

the magnitude of the deflection decreases with an increase in l_c implying that the overall beam stiffness increases with an increase in l_c. Even though E_1 for the transversely isotropic beam is one-half of that for the isotropic beam, the deflection is smaller by a factor of 2.5 suggesting that E_2 for the transversely isotropic beam also plays a role in the beam deflection. On comparing the beam deflections of an isotropic material for the case of a uniform tangential traction at the right edge, the results are almost identical as can be seen in Tables 4.3 and 4.4.

Using Eq. (3.7a) surface traction t_1 and t_2, and higher-order surface traction r_1 and r_2 at $x_2 = -0.0417H$ computed on the transverse cross-sections $X_1 =$ constant with $\vec{\boldsymbol{n}}$ as $(1, 0)$ are plotted in Figs. 4.19 and 4.20, respectively, for the isotropic and the transversely isotropic beams. For each beam, nearly zero values of t_1, r_1 and r_2 at the right end $x_1/L = 1$ indicate that the traction boundary conditions prescribed there are well satisfied. Besides, $t_2 \sim -1.48 \times 10^8$ at $x_1/L = 1$ with the corresponding applied traction $(-(3\times(1-(2/H)^2 \times (-0.0417H)^2))/2H\times 10^7 \approx -1.46 \times 10^8)$. Note that for the classical beam theory ($l_c = 0$ mm), $r_1 = r_2 = 0$, and t_1 and t_2, respectively, equal the axial stress σ_{11} and the shear stress σ_{12}. The variations of the traction are similar for both isotropic and transversely isotropic

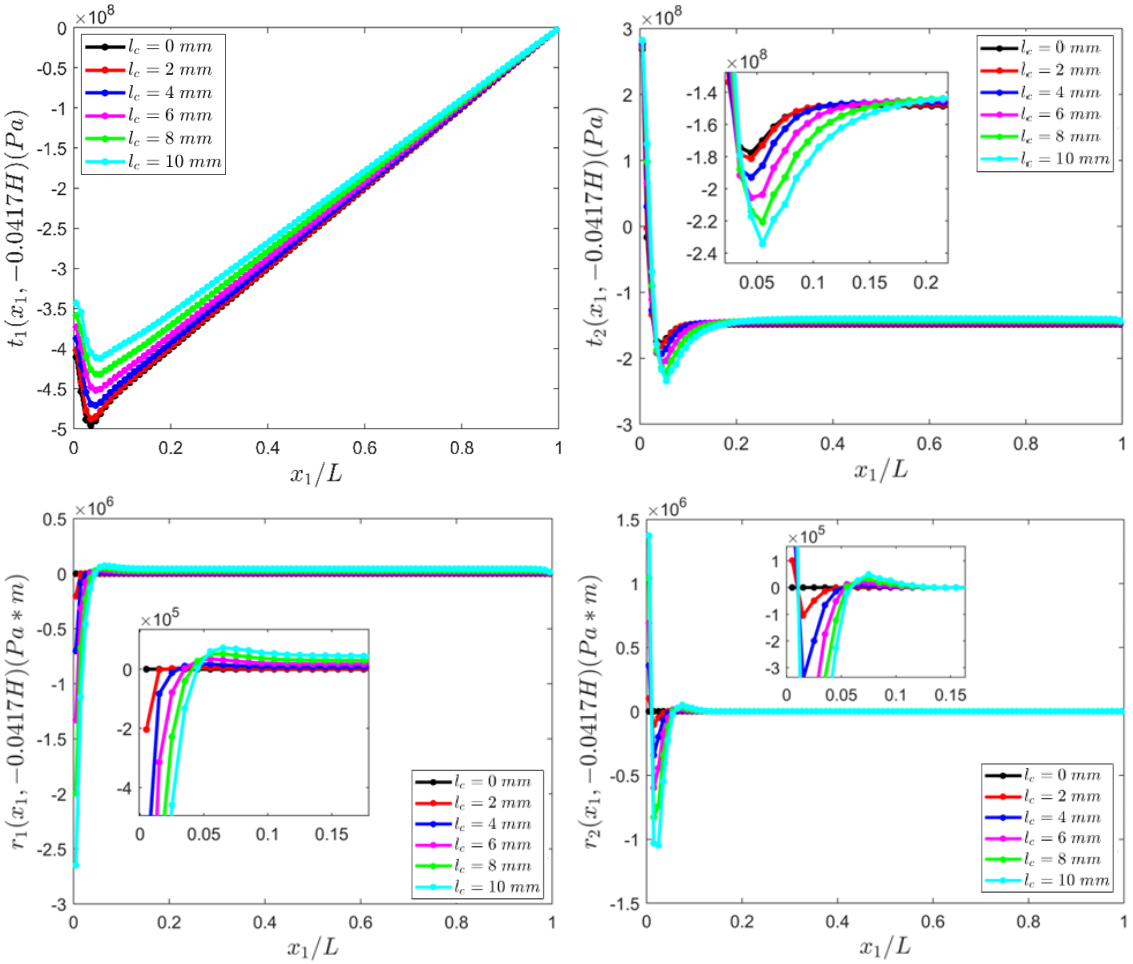

Figure 4.19: For the isotropic material beam, variations on planes x_1 =constant of t_1, t_2, r_1 and r_2 at the point $x_2 = -0.0417H$.

beams. Whereas peak magnitudes of t_1 and r_1 are nearly the same for the isotropic and the transversely isotropic beams, those of t_2 and r_2 at the clamped edge are much smaller for the transversely isotropic beam as compared to that for the isotropic beam mainly due to the large differences in the values of E_2 for them. For each beam, the maximum value of t_1 occurs at a point slightly away from the clamped edge. This differs from that for a Euler-Bernoulli beam for which the maximum magnitude of t_1 occurs at the clamped edge. Except at points within $0.2L$ of the clamped edge, t_1 is nearly uniform over the beam span and its value, independent of l_c, is close to zero because the point $x_2 = -0.0417H$ is close

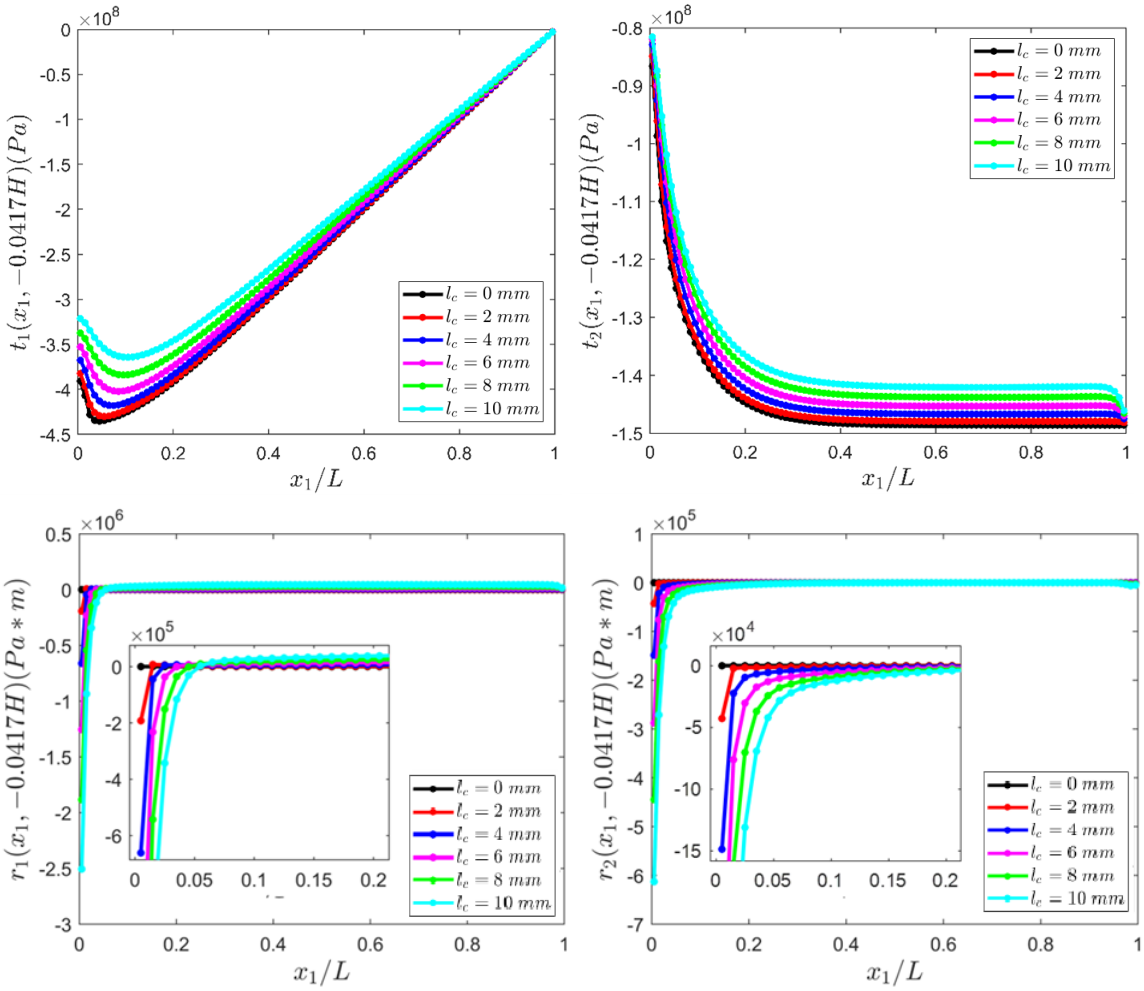

Figure 4.20: For the transversely isotropic material beam, variations on planes x_1 =constant of t_1, t_2, r_1 and r_2 at the point $x_2 = -0.0417H$.

to the neutral surface, $x_2 = 0$. Near the clamped edge, variations with x_1 of both t_1 and t_2 exhibit boundary layers that are more dominant for t_2.

4.2.3 Clamped transversely isotropic beam under a sinusoidal load on the top surface

We now analyze deformations of a clamped transversely isotropic beam of the previous section subjected to a sinusoidal load on the top surface; the sketch of the problem is shown

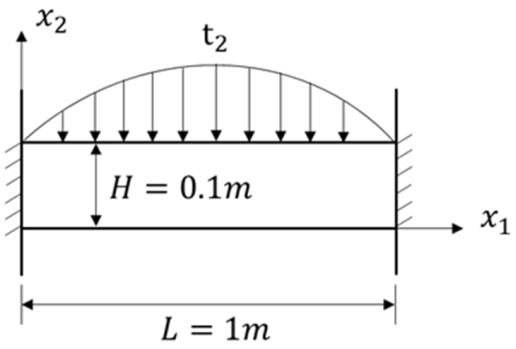

Figure 4.21: Sketch of the beam under a sinusoidal load on the top surface.

in Fig. 4.21. The boundary conditions are:

$$\begin{aligned} &x_2 = H: \quad t_1 = 0, \quad t_2 = -P\sin\left(\tfrac{\pi x_1}{L}\right); \quad r_1 = r_2 = 0 \text{ and } P = 1MPa^{8} \\ &x_2 = 0: \quad t_1 = t_2 = 0; \quad r_1 = r_2 = 0 \\ &x_1 = 0 \text{ and } L: \quad u_1 = u_2 = 0; \quad u_{1,1} = u_{2,1} = 0 \end{aligned} \tag{4.10}$$

Table 4.5: Maximum deflections of the beam's mid-surface ((u_2^{max})) with different values of the characteristic length l_c.

$l_c(mm)^8$	$u_2^{max}(mm)^8$	% Change from u_2 for $l_c = 0$
0	-0.8436	–
2	-0.8356	0.95
4	-0.8175	3.09
6	-0.7949	5.77
8	-0.7706	8.65
10	-0.7462	11.55

For $l_c = 0$, 2, 4, 6, 8 and 10 mm, deformed shapes of the beam mid-surface are depicted in Fig. 4.22, and values of the maximum deflection magnitude are listed in Table 4.5. The qualitative nature of results is similar to that for the cantilever beam studied above. When

[8] In US Customary units: $P = 145\,psi$; $1\,mm = 0.0394\,in$.

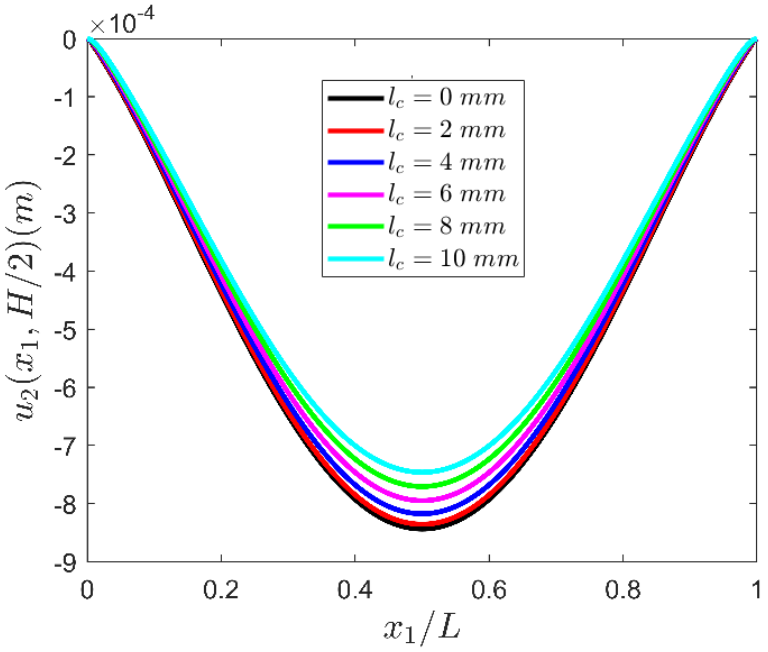

Figure 4.22: For $l_c = 0$, 2, 4, 6, 8 and 10 mm, deformed mid-surfaces of the clamped beam.

l_c is increased from 0 to 10 mm, the magnitude of u_2 decreases by approximately 12%.

The distributions of t_1, t_2, r_1 and r_2 near the mid-plane, on the plane $x_2 = 0.4353H$, are displayed in Fig. 4.23. When looking at the same points on the plane, the magnitudes of t_1 and t_2 (r_1 and r_2) decline (grow) with the increasing values of the characteristic length. Additionally, one can observe the boundary layer effect near the two clamped edges.

Table 4.6: Maximum deflections of the beam's mid-surface with different angles of transverse isotropy and characteristic length values.

$\theta \mid l_c$ [9]	0 mm	4 mm	8 mm
0°	-0.8436	-0.8175	-0.7706
30°	-4.9307	-4.6576	-4.2477
45°	-7.7280	-7.3537	-6.7359
60°	-8.4946	-8.1441	-7.4906
90°	-7.1113	-6.8633	-6.3420

Effect of direction of transverse isotropy

[9] In US Customary units: 1 $mm = 0.0394\ in$.

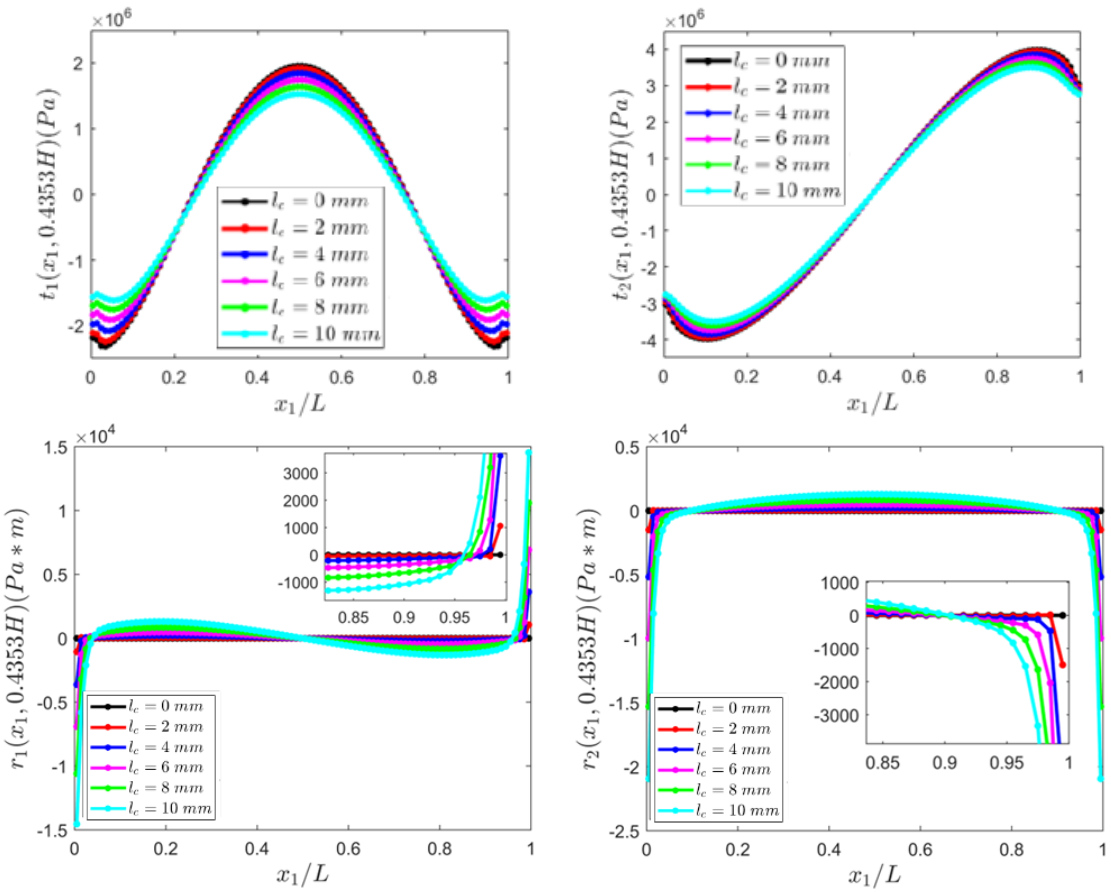

Figure 4.23: Distributions of t_1, t_2, r_1 and r_2 on the plane $x_2 = 0.4353H$.

Here we vary the angle of transverse isotropy of the strain-gradient material and plot in Fig. 4.24 the mid-surface deflections for the beam with $l_c = 4$ mm. We have also reported in Table 4.6 the values of the maximum mid-surface deflection for the beam with different angles of transverse isotropy and characteristic lengths. Notice that θ here represents the angle between the axes of the transverse isotropy of the material and the positive x_1- axis, as shown in Fig. 4.24. It is evident that the angle of transverse isotropy has a more significant effect on the deformation of the beam than the characteristic length value. When the transverse isotropy is along the x_1- direction, the beam experiences the smallest deformation. However, when θ equals to 60°, the maximum deflection is approximately 10 times larger than that when θ equals to 0°.

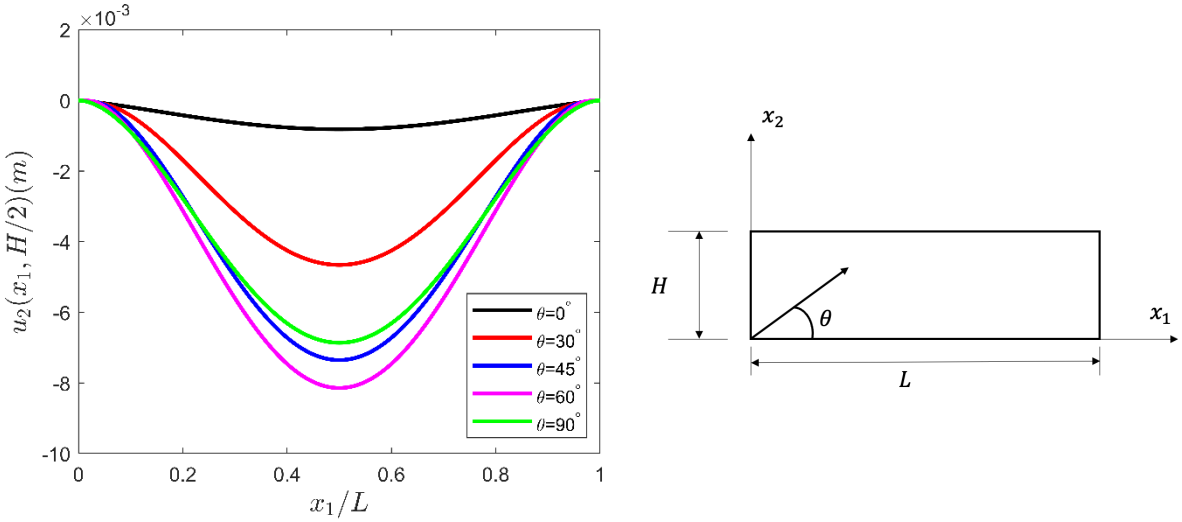

Figure 4.24: Deflections of the mid-surface of the beam with angles of transverse isotropy ($l_c = 4\ mm$), and a sketch of the beam showing the angle of transverse isotropy.

Effect of beam thickness

In this exercise, we consider a strain-gradient beam made of the transversely isotropic material with $l_c = 0.1\ mm$, with a sinusoidal load on the top surface $t_2 = -P \sin\left(\frac{20\pi x_1}{L}\right)$ and $\theta = 0°$. In Fig. 4.25, we plot the ratio of the maximum vertical deflection of the mid-surface for the strain-gradient theory (u_2^{sgt}) and the classical theory ($u_2^{classical}$) versus H/l_c. As we keep l_c fixed and increase $n = H/l_c$, the size of the beam increases and the ratio between the classical and the strain-gradient solutions goes to 1 as can be seen in the Table 4.7.

Table 4.7: Maximum deflections of the beam's mid-surface for strain-gradient theory (u_2^{sgt}) and the classical theory ($u_2^{classical}$) for different values of H/l_c.

$n = H/l_c$	u_2^{sgt}	$u_2^{classical}$	$u_2^{sgt}/u_2^{classical}$
1	-4.1187	-23.155	0.178
4	-0.4672	-0.795	0.588
8	-0.0862	-0.102	0.845
12	-0.0282	-0.0305	0.924
16	-0.0124	-0.013	0.954
20	-0.0065	-0.0067	0.974
100	-6.99 $\times 10^{-5}$	-7.00 $\times 10^{-5}$	0.998

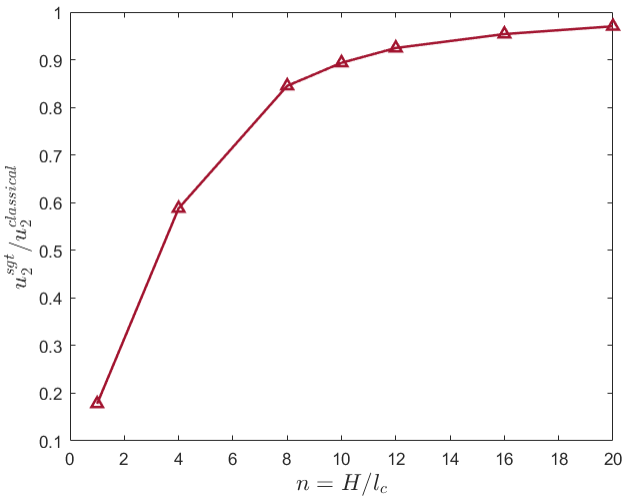

Figure 4.25: The non-dimensional deflection versus $n = H/l_c$.

4.2.4 Clamped transversely isotropic beam under a sinusoidal load with 25 half-waves

In this example, we consider applying on the top surface a sinusoidal load with 25 half-waves as shown in Fig. 4.26. The geometric and the material parameters are the same as for the previous problem. The boundary conditions are:

$$\begin{gathered} x_2 = H : t_1 = 0, t_2 = -P \operatorname{abs}\left(\sin\left(\tfrac{25\pi x_1}{L}\right)\right); r_1 = r_2 = 0 \text{ and } P = 1MPa^{10} \\ x_2 = 0 : t_1 = t_2 = 0; \quad r_1 = r_2 = 0 \\ x_1 = 0 \text{ and } L : u_1 = u_2 = 0; \quad u_{1,1} = u_{2,1} = 0 \end{gathered} \tag{4.11}$$

The deformed shapes of the mid-surface are plotted in Fig.4.27 and the values of the deflection at $x_1 = L/2$ are given in Table 4.8 The magnitude of the deflection changes monotonically with the increase in the characteristic length value. When l_c grows to 10 mm, the magnitude of the maximum deflection of the mid-surface decreases to 0.5740 mm, which is

[10] In US Customary units: $P = 145.04\, psi$

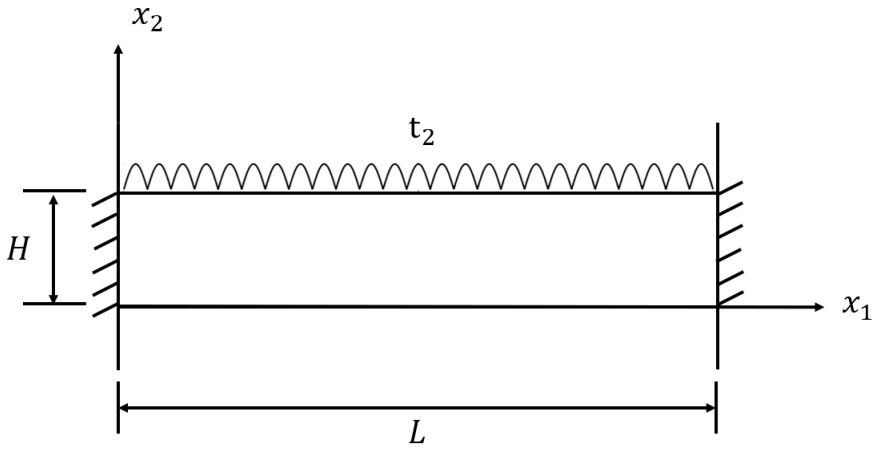

Figure 4.26: Sketch of the beam under a sinusoidal load with 25 half-waves on the top surface.

Table 4.8: Maximum deflections ((u_2^{max})) of the beam's mid-surface for different values of the characteristic length l_c.

$l_c(mm)$	$u_2^{max}(mm)$	% Change from u_2 for $l_c = 0$
0	-0.6519	–
2	-0.6452	1.02
4	-0.6306	3.27
6	-0.6125	6.04
8	-0.5933	8.99
10	-0.5740	11.94

approximately 12% less than that when l_c equals to 0 mm. The reduction in amplitude is slightly larger than that of the beam subjected to a sinusoidal load with only one half-wave.

In Fig.4.28 we have depicted the variations of t_1, t_2, r_1 and r_2 on the horizontal surface $x_2 = 0.4353$H. As can be seen from the figure, the magnitudes of t_1 and t_2 at the same cross-section decrease with the increase in l_c, while the trend is the opposite for r_1 and r_2.

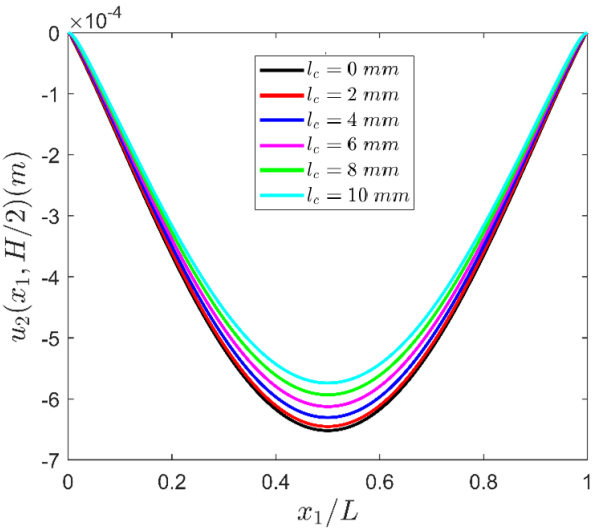

Figure 4.27: Deflections of the mid-surface of the beam with different values of the characteristic length.

4.2.5 Isotropic cantilever beam under higher-order loading

In this subsection, we study the plane strain bending of a cantilever beam under a tangential higher-order traction. The sketch of the problem is shown in Fig.4.29. The beam is fixed at the left end and a uniformly distributed higher-order surface traction, r_2, is applied at the right end. The boundary conditions are:

$$\begin{aligned} x_2 = \pm\tfrac{H}{2}: \quad & t_1 = t_2 = 0,\ r_1 = r_2 = 0 \\ x_1 = 0: \quad & u_1 = u_2 = 0,\ u_{1,1} = u_{2,1} = 0 \\ x_1 = L: \quad & t_1 = t_2 = 0,\ r_1 = 0,\ r_2 = -0.1\ MPa \cdot m \end{aligned} \tag{4.12}$$

The material of the beam is assumed to be an isotropic with material properties given by:

$$E = 200\ GPa,\ \nu = 0.3,\ l_c = 2,\ 4, \text{and } 6\ mm \tag{4.13}$$

[11] In US Customary units: $r_2 = -571\ psi \cdot in$; $E = 2.9 \times 10^7\ psi$; $l_c = 0.079,\ 0.156, \text{and } 0.236\ in$.

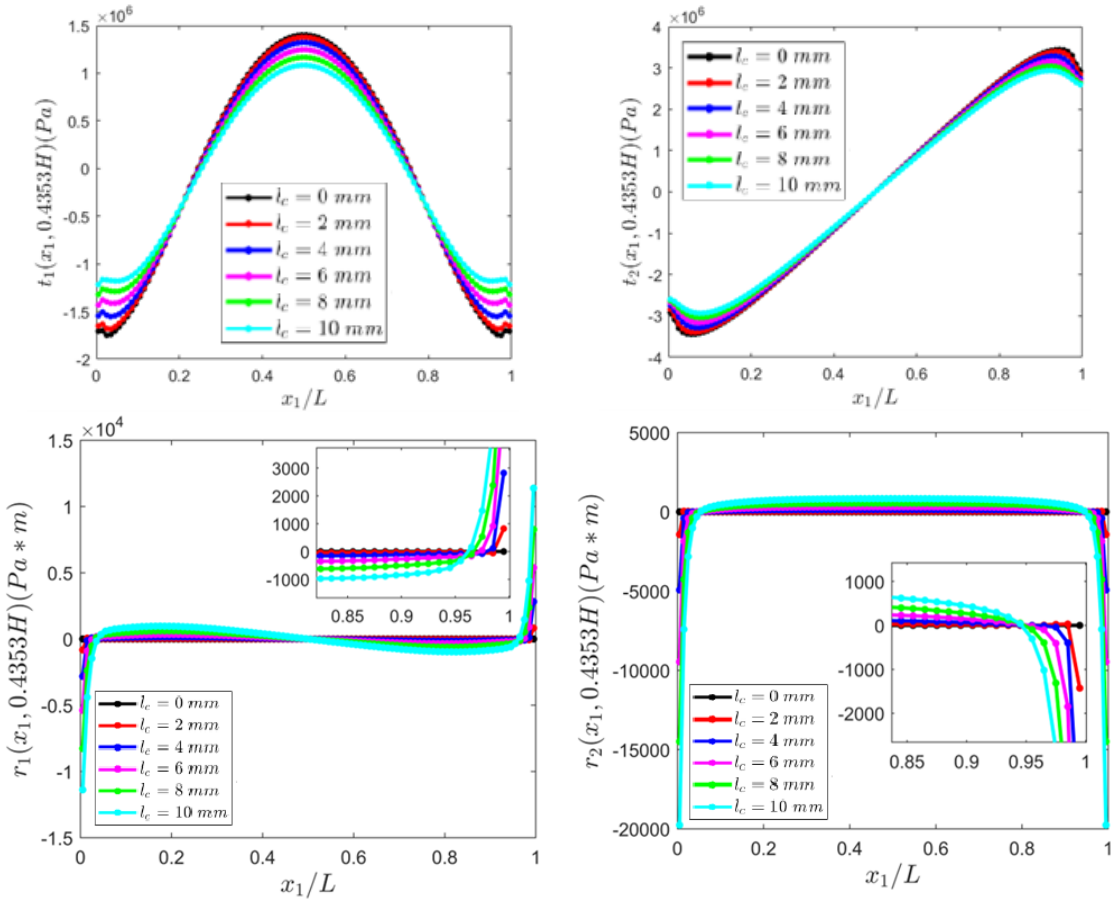

Figure 4.28: Distributions of t_1, t_2, r_1 and r_2 on the plane $x_2 = 0.4353H$.

It is supposed that the value of the characteristic length can vary from 2 to 6 mm to investigate the effects of strain gradients. A uniform 50×24 mesh is used to discretize the beam. The magnitude of the deflection decreases with an increase in the characteristic length, which indicates the beam becomes stiffer with increasing the strain gradient effects, i.e., l_c.

Using Eq.(3.7a), we compute values of surface tractions t_1 and t_2, and higher-order surface tractions r_1 and r_2 at the element centroids located at the transverse cross-sections along the horizontal line near the mid-surface ($x_2 = 0.4643H$) by taking $\vec{\boldsymbol{n}} = (1, 0)$ and plot them in Fig. 4.30. Values of t_1 and r_1 at the right end are found to be close to zero and r_2

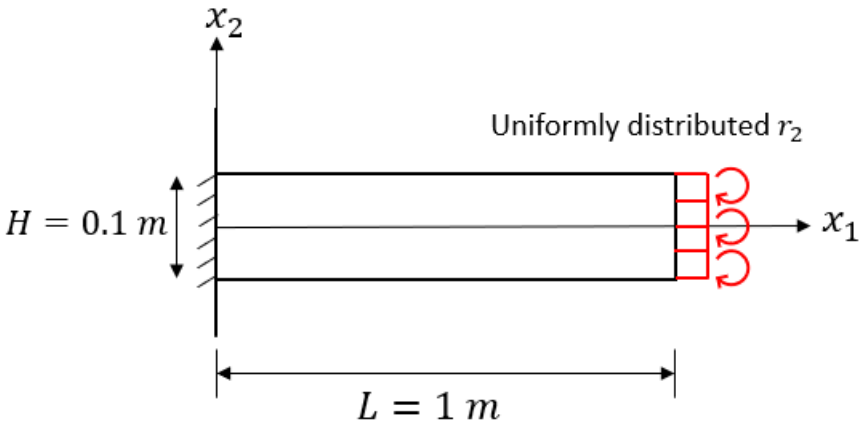

Figure 4.29: Sketch of the beam under a higher-order surface traction, r_2, at the right edge.

approaching $-1\ MPa.m$, which satisfies the traction boundary conditions. But, the value of t_2 is non-zero at the right end, which does not satisfy the traction boundary condition. Notice that for the case $l_c = 0\ mm$, r_2 cannot be applied as there are no strain gradient effects.

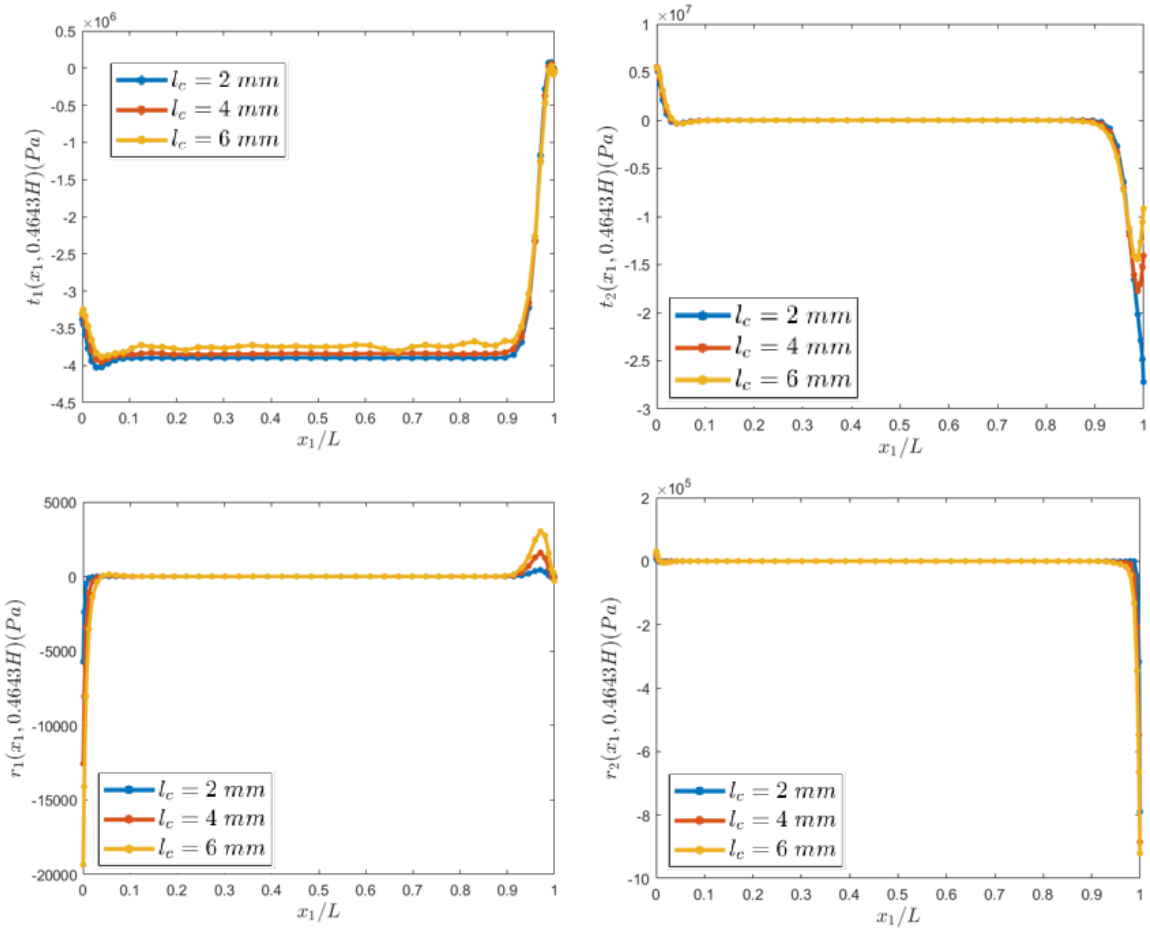

Figure 4.30: Distributions of t_1, t_2, r_1 and r_2 on the plane $x_2 = 0.4643H$.

Chapter 5

Conclusions

In this work, we have developed a finite element code to study static plane strain problems for linearly elastic strain gradient materials. A mixed finite element formulation is used, by introducing displacement-gradients as intermediate variables, to use C^0-continuous elements. Lagrange multipliers also act as nodal unknowns to enforce the kinematic constraints. We use a simple constitutive relation from the literature to find the corresponding stresses and non-classical stresses. We use the principle of minimum potential energy to derive the governing equations.

We analyzed three mixed isoparametric quadrilateral elements, as presented in subsection 4.1.1. We observed that $QU34L4$ did not capture the displacement gradients for the assumed displacement field in the method of manufactured solutions. Both $QU34L16$ and $QU48L32$ were able to reproduce the displacements as well as displacement gradients for the assumed solution numerically but the latter was computationally more expensive. We conclude from the results that $QU34L16$ is a good choice and used it to study beam bending problems.

The developed code is verified by comparing the results for problems solved in the literature and using the Method of Manufactured Solutions (MMS). The obtained results compare well for the problems studied.

To showcase the size-dependence in small scale solids, we numerically study beam bending problems for isotropic and transversely-isotropic strain-gradient-dependent materials. Sig-

nificant differences in beam deflections were observed on the comparison of classical and strain-gradient solutions. As the *material characteristic length* becomes smaller and smaller, the the strain gradient solution approaches the classical solution.

We also implemented MMS to verify our finite element implementation. In this approach, for an assumed displacement field, we obtain the classical and higher-order surface traction along with the body forces. Application of these body forces and surface traction should retrieve the assumed displacements. We observe that the results obtained are in good agreement with the assumed analytical solutions.

Bibliography

[1] J. Y. Shu, W. E. King, and N. A. Fleck, "Finite elements for materials with strain gradient effects," *International Journal for Numerical Methods in Engineering*, vol. 44, no. 3, pp. 373–391, 1999.

[2] N. A. Fleck, G. M. Muller, M. F. Ashby, and J. W. Hutchinson, "Strain gradient plasticity: Theory and experiment," *Acta Metallurgica Et Materialia*, vol. 42, no. 2, pp. 475–487, 1994.

[3] E. Cosserat and F. Cosserat, *Theorie des corps deformables*. Paris: Hermann et Fils, 1909.

[4] R. A. Toupin, "Theories of elasticity with couple-stress," 1964.

[5] R. D. Mindlin, "Micro-structure in linear elasticity," *Archive for Rational Mechanics and Analysis*, vol. 16, pp. 51–78, 1963.

[6] R. Artan and R. C. Batra, "Free vibrations of a strain gradient beam by the method of initial values," *Acta Mechanica*, vol. 223, no. 11, pp. 2393–2409, 2012.

[7] R. D. Mindlin and N. N. Eshel, "On first strain-gradient theories in linear elasticity," *International Journal of Solids and Structures*, vol. 4, no. 1, pp. 109–124, 1968.

[8] E. C. Aifantis, "On the role of gradients in the localization of deformation and fracture," *International Journal of Engineering Science*, vol. 30, no. 10, pp. 1279–1299, 1992.

[9] O. W. Dillon and J. Kratochvil, "A strain gradient theory of plasticity," *International Journal of Solids and Structures*, vol. 6, no. 12, pp. 1513–1533, 1970.

[10] E. C. Aifantis, "On the microstructural origin of certain inelastic models," *Journal of Engineering Materials and Technology*, vol. 106, pp. 326–330, oct 1984.

[11] N. A. Fleck and J. W. Hutchinson, *Strain gradient plasticity*, vol. 33. Elsevier Masson SAS, 1997.

[12] K. Hwang, H. Jiang, Y. Huang, H. Gao, and N. Hu, "A finite deformation theory of strain gradient plasticity," *Journal of the Mechanics and Physics of Solids*, vol. 50, pp. 81–99, 2002.

[13] R. C. Batra, "The initiation and growth of, and the interaction among, adiabatic shear bands in simple and dipolar materials," *International Journal of Plasticity*, vol. 3, pp. 75–89, 1987.

[14] R. C. Batra, "Thermodynamics of non-simple elastic materials," *Journal of Elasticity*, vol. 6, no. 4, pp. 451–456, 1976.

[15] A. E. Green and N. Laws, "On the entropy production inequality," *Archive for Rational Mechanics and Analysis*, vol. 45, no. 1, pp. 47–53, 1972.

[16] F. Yang, A. C. Chong, D. C. Lam, and P. Tong, "Couple stress based strain gradient theory for elasticity," *International Journal of Solids and Structures*, vol. 39, no. 10, pp. 2731–2743, 2002.

[17] R. C. Batra and J. Hwang, "Dynamic shear band development in dipolar thermoviscoplastic materials," *Computational Mechanics*, vol. 14, no. 4, pp. 354–369, 1994.

[18] M. Kandaz and H. Dal, "A comparative study of modified strain gradient theory and modified couple stress theory for gold microbeams," *Archive of Applied Mechanics*, vol. 88, no. 11, pp. 2051–2070, 2018.

[19] E. Amanatidou and N. Aravas, "Mixed finite element formulations of strain-gradient elasticity problems," *Computer Methods in Applied Mechanics and Engineering*, vol. 191, no. 15-16, pp. 1723–1751, 2002.

[20] U. Andreaus, F. Dell'Isola, I. Giorgio, L. Placidi, T. Lekszycki, and N. L. Rizzi, "Numerical simulations of classical problems in two-dimensional (non) linear second gradient elasticity," *International Journal of Engineering Science*, vol. 108, pp. 34–50, 2016.

[21] R. Ansari, M. Faghih Shojaei, A. H. Shakouri, and H. Rouhi, "Nonlinear bending analysis of first-order shear deformable microscale plates using a strain gradient quadrilateral element," *Journal of Computational and Nonlinear Dynamics*, vol. 11, no. 5, pp. 1–18, 2016.

[22] A. Jafari and M. Ezzati, "Investigating the non-classical boundary conditions relevant to strain gradient theories," *Physica E: Low-Dimensional Systems and Nanostructures*, vol. 86, no. September 2016, pp. 88–102, 2017.

[23] S. V. Tsinopoulos, D. Polyzos, and D. E. Beskos, "Static and dynamic BEM analysis of strain gradient elastic solids and structures," *CMES - Computer Modeling in Engineering and Sciences*, vol. 86, no. 2, pp. 113–144, 2012.

[24] J. Peddieson, G. R. Buchanan, and R. P. McNitt, "Application of nonlocal continuum models to nanotechnology," *International Journal of Engineering Science*, vol. 41, no. 3-5, pp. 305–312, 2003.

[25] A. C. Eringen, "Nonlocal polar elastic continua," *International Journal of Engineering Science*, vol. 10, no. 1, pp. 1–16, 1972.

[26] S. Lurie and Y. Solyaev, "Revisiting bending theories of elastic gradient beams," *International Journal of Engineering Science*, vol. 126, pp. 1–21, 2018.

[27] Y. Solyaev and S. Lurie, "Analytical solution of a plane strain pure bending problem in second gradient electroelasticity," *arXiv:1811.08087 [physics.class-ph]*, 2018.

[28] A. Beheshti, "Finite element analysis of plane strain solids in strain-gradient elasticity," *Acta Mechanica*, vol. 228, no. 10, pp. 3543–3559, 2017.

[29] J. C. Reiher, I. Giorgio, and A. Bertram, "Finite-element analysis of polyhedra under point and line forces in second-strain gradient elasticity," *Journal of Engineering Mechanics*, vol. 143, no. 2, pp. 1–13, 2017.

[30] P. J. Roache, "Code verification by the method of manufactured solutions," *Journal of Fluids Engineering*, vol. 124, pp. 4–10, nov 2001.

[31] S. Steinberg and P. J. Roache, "Symbolic manipulation and computational fluid dynamics," *Journal of Computational Physics*, vol. 57, pp. 251–284, 1985.

[32] R. C. Batra and X. Q. Liang, "Finite dynamic deformations of smart structures," *Computational Mechanics*, vol. 20, no. 5, pp. 427–438, 1997.

[33] R. C. Batra and B. M. Love, "Consideration of microstructural effects in the analysis of adiabatic shear bands in a tungsten heavy alloy," *International Journal of Plasticity*, vol. 22, no. 10, pp. 1858–1878, 2006.

[34] B. S. Altan and E. C. Aifantis, "On some aspects in the special theory of gradient elasticity," *Journal of the Mechanical Behavior of Materials*, vol. 8, no. 3, pp. 231–282, 1997.

[35] A. E. Giannakopoulos, E. Amanatidou, and N. Aravas, "A reciprocity theorem in linear gradient elasticity and the corresponding Saint-Venant principle," *International Journal of Solids and Structures*, vol. 43, no. 13, pp. 3875–3894, 2006.

[36] I. M. Gitman, H. Askes, E. Kuhl, and E. C. Aifantis, "Stress concentrations in fractured compact bone simulated with a special class of anisotropic gradient elasticity," *International Journal of Solids and Structures*, vol. 47, no. 9, pp. 1099–1107, 2010.

[37] Y. M. Yue, K. Y. Xu, and E. C. Aifantis, "Microscale size effects on the electromechanical coupling in piezoelectric material for anti-plane problem," *Smart Materials and Structures*, vol. 23, no. 12, 2014.

[38] Y. Yue, K. Xu, and E. C. Aifantis, "Strain gradient and electric field gradient effects in piezoelectric cantilever beams," *Journal of the Mechanical Behavior of Materials*, vol. 24, no. 3-4, pp. 121–127, 2015.

[39] T. J. Hughes, "Mixed and penalty methods, reduced and selective integration, and sundry variational crimes," in *The Finite Element Method: Linear Static and Dynamic Finite Element Analysis*, pp. 185–225, Dover Publications, 2000.

[40] O. A. Ladyzhenskaya, *The mathematical theory of viscous incompressible flow.* 1969.

[41] I. Babuška, "The finite element method with Lagrangian multipliers," *Numerische Mathematik*, vol. 20, no. 3, pp. 179–192, 1973.

[42] F. Brezzi, "On the existence, uniqueness and approximation of saddle-point problems arising from lagrangian multipliers," *RAIRO Ser. Anal. Numer.*, vol. 8, pp. 129–151, 1974.

[43] O. C. Zienkiewicz, J. P. Vilotte, and S. Toyoshima, "Iterative method for constrained and mixed approximation-an inexpensive improvement of f.e.m. performance," *Computer Methods in Applied Mechanics and Engineering*, vol. 51, pp. 3–29, 1985.

[44] S. S. Vel and R. C. Batra, "The generalized plane strain deformations of thick anisotropic

composite laminated plates," *International Journal of Solids and Structures*, vol. 37, pp. 715–733, 2000.

[45] F. Tornabene, N. Fantuzzi, E. Viola, and R. C. Batra, "Stress and strain recovery for functionally graded free-form and doubly-curved sandwich shells using higher-order equivalent single layer theory," *Composite Structures*, vol. 119, pp. 67–89, 2015.

[46] Timoshenko, *Theory of elasticity.* Engineering societies monographs, New York: McGraw-Hill, 1970.

[47] M. Fortin and R. Glowinski, *Méthodes de lagrangien augmenté.* Paris : Dunod, 1982.

Appendices

Appendix A

FEM details

A.1 Assembly of global stiffness matrix $\boldsymbol{K}_g$

For the assembly of global stiffness matrix ($\boldsymbol{K}_g$) and the global load vector ($\boldsymbol{F}_g$), we expand each of the three equations in (3.22) over $i, j = 1, ..., 2$ over the whole domain, Ω.

Eq. (3.22a) is summed over j, expanding it for $i = 1, 2$ gives:

$$\begin{aligned} i=1: \ & \textstyle\sum_e \left[\int_{\Omega^e}(\sigma_{11}\mathbb{N}^n_{,1} + \sigma_{12}\mathbb{N}^n_{,2})dA + \int_{\Omega^e}(g^p_{11}N^p\mathbb{N}^n_{,1} + g^p_{12}N^p\mathbb{N}^n_{,2})dA\right] = \textstyle\sum_e \left[\int_{\partial\Omega^e} t^e_1\mathbb{N}^n dl\right] \\ i=2: \ & \textstyle\sum_e \left[\int_{\Omega^e}(\sigma_{12}\mathbb{N}^n_{,1} + \sigma_{22}\mathbb{N}^n_{,2})dA + \int_{\Omega^e}(g^p_{21}N^p\mathbb{N}^n_{,1} + g^p_{22}N^p\mathbb{N}^n_{,2})dA\right] = \textstyle\sum_e \left[\int_{\partial\Omega^e} t^e_2\mathbb{N}^n dl\right] \end{aligned} \tag{A.1}$$

Expanding Eq. (3.22b) over $i, j = 1, 2$ gives:

$$\begin{aligned} i=1,\ j=1: \ & \textstyle\sum_e \left[\int_{\Omega^e}(\tau_{111}\aleph^m_{,1} + \tau_{112}\aleph^m_{,2})dA - g^p_{11}\int_{\Omega^e} N^p\aleph^m dA\right] = \textstyle\sum_e \left[\int_{\partial\Omega^e} r^e_1 n^e_1\aleph^m dl\right] \\ i=1,\ j=2: \ & \textstyle\sum_e \left[\int_{\Omega^e}(\tau_{121}\aleph^m_{,1} + \tau_{122}\aleph^m_{,2})dA - g^p_{12}\int_{\Omega^e} N^p\aleph^m dA\right] = \textstyle\sum_e \left[\int_{\partial\Omega^e} r^e_1 n^e_2\aleph^m dl\right] \\ i=2,\ j=1: \ & \textstyle\sum_e \left[\int_{\Omega^e}(\tau_{211}\aleph^m_{,1} + \tau_{212}\aleph^m_{,2})dA - g^p_{21}\int_{\Omega^e} N^p\aleph^m dA\right] = \textstyle\sum_e \left[\int_{\partial\Omega^e} r^e_2 n^e_1\aleph^m dl\right] \\ i=2,\ j=2: \ & \textstyle\sum_e \left[\int_{\Omega^e}(\tau_{221}\aleph^m_{,1} + \tau_{222}\aleph^m_{,2})dA - g^p_{22}\int_{\Omega^e} N^p\aleph^m dA\right] = \textstyle\sum_e \left[\int_{\partial\Omega^e} r^e_2 n^e_2\aleph^m dl\right] \end{aligned} \tag{A.2}$$

Similarly, expanding Eq. (3.22c) over $i, j = 1, 2$ gives:

$$
\begin{aligned}
i=1,\ j=1:\ &\textstyle\sum_e \left[\int_{\Omega^e} N^p \left(w_{11}^m \aleph^m - d_1^n \mathbb{N}_1^n\right) dA\right] = 0 \\
i=1,\ j=2:\ &\textstyle\sum_e \left[\int_{\Omega^e} N^p \left(w_{12}^m \aleph^m - d_1^n \mathbb{N}_2^n\right) dA\right] = 0 \\
i=2,\ j=1:\ &\textstyle\sum_e \left[\int_{\Omega^e} N^p \left(w_{21}^m \aleph^m - d_2^n \mathbb{N}_1^n\right) dA\right] = 0 \\
i=2,\ j=2:\ &\textstyle\sum_e \left[\int_{\Omega^e} N^p \left(w_{22}^m \aleph^m - d_2^n \mathbb{N}_2^n\right) dA\right] = 0
\end{aligned}
\tag{A.3}
$$

Substituting for classical (σ_{ij}) and higher-order stresses (κ_{ijk}) in terms of strains and strain-gradients from the constitutive relation in Eq.(3.23) and then for u_i, β_{ij} and Λ_{ij} in terms of their nodal values in Eqns. (A.1), (A.2), (A.3), we get:

$$
\begin{aligned}
i=1:\ &\textstyle\sum_e \left[d_1^n(D_{11}K_{11}^e + D_{33}K_{22}^e) + d_2^n(D_{33}K_{21}^e + D_{12}K_{12}^e) + (A_1^e)^T g_{11}^p + (A_2^e)^T g_{12}^p\right] = \sum_e [F_1^e] \\
i=2:\ &\textstyle\sum_e \left[d_1^n(D_{12}K_{21}^e + D_{33}K_{12}^e) + d_2^n(D_{33}K_{11}^e + D_{22}K_{22}^e) + (A_1^e)^T g_{21}^p + (A_2^e)^T g_{22}^p\right] = \sum_e [F_2^e] \\
&\text{where } K_{ij}^e = \textstyle\int_{\Omega^e} (\mathbb{N}_{,i}^n)^T \mathbb{N}_{,j}^n dA,\ A_j^e = \int_{\partial\Omega^e} N^p \mathbb{N}_{,j}^n dA \text{ and } F_i^e = \int_{\partial\Omega^e} t_i^e \mathbb{N}^n dl.
\end{aligned}
\tag{A.4}
$$

$$
\begin{aligned}
i=1,\ j=1:\ &\textstyle\sum_e \left[w_{11}^m \overline{D}_{11} \overline{K}_{11}^e + w_{12}^m \overline{D}_{22} \overline{K}_{21}^e + w_{21}^m \overline{D}_{13} \overline{K}_{12}^e + w_{22}^m \overline{D}_{24} \overline{K}_{22}^e - (M^e)^T g_{11}^p\right] = \sum_e [H_{11}^e] \\
i=1,\ j=2:\ &\textstyle\sum_e \left[w_{11}^m \overline{D}_{55} \overline{K}_{12}^e + w_{12}^m \overline{D}_{66} \overline{K}_{22}^e + w_{21}^m \overline{D}_{55} \overline{K}_{11}^e + w_{22}^m \overline{D}_{66} \overline{K}_{21}^e - (M^e)^T g_{12}^p\right] = \sum_e [H_{12}^e] \\
i=2,\ j=1:\ &\textstyle\sum_e \left[w_{11}^m \overline{D}_{55} \overline{K}_{12}^e + w_{12}^m \overline{D}_{66} \overline{K}_{22}^e + w_{21}^m \overline{D}_{55} \overline{K}_{11}^e + w_{22}^m \overline{D}_{66} \overline{K}_{21}^e - (M^e)^T g_{21}^p\right] = \sum_e [H_{21}^e] \\
i=2,\ j=2:\ &\textstyle\sum_e \left[w_{11}^m \overline{D}_{31} \overline{K}_{11}^e + w_{12}^m \overline{D}_{42} \overline{K}_{21}^e + w_{21}^m \overline{D}_{33} \overline{K}_{12}^e + w_{22}^m \overline{D}_{44} \overline{K}_{22}^e - (M^e)^T g_{22}^p\right] = \sum_e [H_{22}^e] \\
&\text{where } \overline{K}_{ij}^e = \textstyle\int_{\Omega^e} (\aleph_{,k}^m)^T\ \aleph_{,k}^m dA,\ M^e = \int_{\partial\Omega^e} N^p \aleph^m dA \text{ and } H_{ij}^e = \int_{\partial\Omega^e} r_i^e n_j^e \aleph^m dl.
\end{aligned}
\tag{A.5}
$$

$$\begin{aligned} i=1,\ j=1:\ \textstyle\sum_e [w_{11}^m M^e - d_1^n A_1^e] = 0 \\ i=1,\ j=2:\ \textstyle\sum_e [w_{12}^m M^e - d_1^n A_2^e] = 0 \\ i=2,\ j=1:\ \textstyle\sum_e [w_{21}^m M^e - d_2^n A_1^e] = 0 \\ i=2,\ j=2:\ \textstyle\sum_e [w_{22}^m M^e - d_2^n A_2^e] = 0 \end{aligned} \tag{A.6}$$

where $A_j^e = \int_{\partial\Omega^e} N^p \mathbb{N}_{,j}^n dA$ and $M^e = \int_{\partial\Omega^e} N^p \aleph^m dA$.

Now, combining Eqns. (A.4), (A.5), (A.6) and writing in the matrix form, we get:

$$\boldsymbol{K}_g\, \boldsymbol{U} = \boldsymbol{F}_g$$

$$\text{That is, } \begin{bmatrix} \boldsymbol{K} & \boldsymbol{0} & \boldsymbol{A}^T \\ \boldsymbol{0} & \overline{\boldsymbol{K}} & -\boldsymbol{M}^T \\ \boldsymbol{A} & -\boldsymbol{M} & \boldsymbol{0} \end{bmatrix} \begin{bmatrix} \boldsymbol{d} \\ \boldsymbol{w} \\ \boldsymbol{g} \end{bmatrix} = \begin{bmatrix} \boldsymbol{F} \\ \boldsymbol{H} \\ \boldsymbol{0} \end{bmatrix} \tag{A.7}$$

where $\boldsymbol{d} = \{d_1,\ d_2\}^T$, $\boldsymbol{e} = \{w_{11},\ w_{12},\ w_{21},\ w_{22}\}^T$, and $\boldsymbol{g} = \{g_{11},\ g_{12},\ g_{21},\ g_{22}\}^T$

Please note that $d_1 = \{d_1^1, d_1^2, ..., d_1^n\}^T$ where n represents the total number of nodes where u_1 is an unknown. The components of the global stiffness matrix ($\boldsymbol{K}_g$) and the global load vector ($\boldsymbol{F}_g$) are given by:

$$\boldsymbol{K} = \begin{bmatrix} D_{11}K_{11} + D_{33}K_{22} & D_{33}K_{21} + D_{12}K_{12} \\ D_{12}K_{21} + D_{33}K_{12} & D_{33}K_{11} + D_{22}K_{22} \end{bmatrix}$$

$$\overline{\boldsymbol{K}} = \begin{bmatrix} \overline{D}_{11}\overline{K}_{11} & \overline{D}_{22}\overline{K}_{21} & \overline{D}_{13}\overline{K}_{12} & \overline{D}_{24}\overline{K}_{22} \\ \overline{D}_{55}\overline{K}_{12} & \overline{D}_{66}\overline{K}_{22} & \overline{D}_{55}\overline{K}_{11} & \overline{D}_{66}\overline{K}_{21} \\ \overline{D}_{55}\overline{K}_{12} & \overline{D}_{66}\overline{K}_{22} & \overline{D}_{55}\overline{K}_{11} & \overline{D}_{66}\overline{K}_{21} \\ \overline{D}_{31}\overline{K}_{11} & \overline{D}_{42}\overline{K}_{21} & \overline{D}_{33}\overline{K}_{12} & \overline{D}_{44}\overline{K}_{22} \end{bmatrix}$$

$$\boldsymbol{A} = \begin{bmatrix} A_1 & 0 \\ A_2 & 0 \\ 0 & A_1 \\ 0 & A_2 \end{bmatrix} \text{ where } size(0) = size(A_i) \tag{A.8}$$

$$\boldsymbol{M} = \begin{bmatrix} M & 0 & 0 & 0 \\ 0 & M & 0 & 0 \\ 0 & 0 & M & 0 \\ 0 & 0 & 0 & M \end{bmatrix} \text{ where } size(0) = size(M)$$

$$\boldsymbol{F} = \begin{bmatrix} F_1 & F_2 \end{bmatrix}^T$$

$$\boldsymbol{H} = \begin{bmatrix} H_{11} & H_{12} & H_{21} & H_{22} \end{bmatrix}^T$$

where $K_{ij} = \sum_e K^e_{ij}$, $\overline{K}_{ij} = \sum_e \overline{K}^e_{ij}$, $A_j = \sum_e A^e_j$,
$M = \sum_e M^e$, $F_i = \sum_e F^e_i$, and $H_{ij} = \sum_e H^e_{ij}$.

A.2 Method of constraint counting

Babuska-Brezzi, or *LBB*, stability condition is a technique to ensure there is no element locking and that the mixed finite element methods lead to mathematical convergence. But checking whether this condition is satisfied for elements is not a trivial task. Here we use a heuristic approach called Method of constraint counts, explained in [39]. It is a quick, simple, and effective tool to assess whether an element will lock or not, although there might be other issues deciding the overall element performance.

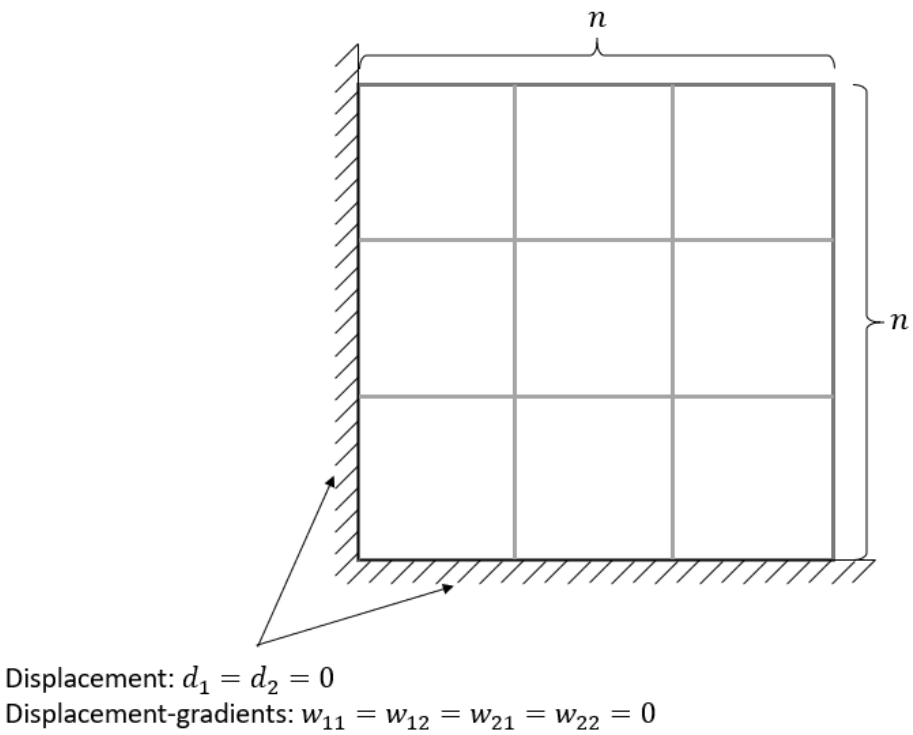

Figure A.1: Standard mesh with n elements in both x_1 and x_2 directions and the left and bottom edges are clamped.

For the standard FE mesh shown in Fig. A.1, let n_{eq} equal the total number of displacement (u_i) and displacement-gradient (β_{ij}) equations after the application of essential boundary conditions, and n_c the total number of constraint equations, i.e., equations corresponding to

the Lagrange multipliers (Λ_{ij}). The *constraint ratio*, r_c, is defined as [39]:

$$r_c = \frac{n_{eq}}{n_c} \tag{A.9}$$

Hughes [39] has stated that a quick and easy way to check if an element satisfies the *LBB* condition is to find r_c and use the following criteria for a 2-dimensional (e.g., plane strain) problem. [39]:

$$\begin{gathered} r_c > 2 \quad \textit{too few constraint equation} \\ r_c = 2 \quad \textit{optimal} \\ r_c < 2 \quad \textit{too many constraint equation} \\ r_c \leq 1 \quad \textit{locking} \end{gathered} \tag{A.10}$$

When $r_c > 2$, the constraint (i.e., $\beta_{ij} = u_{i,j}$) is not well satisfied. Similarly, for $r_c < 2$ the system of equations is overly constrained.

Although Hughes [39] used the method of constraint counting for displacement and pressure as nodal unknowns, one can extend that approach for elements with displacement-gradients as nodal unknowns. For the three elements shown in Fig. 3.2 and using the standard FE mesh of Fig. A.1, we obtain the following values of constraint ratio, r_c.

$$QU34L4: \ \frac{n_{eq}}{n_c} = \frac{[2(2n+1)^2 - (4n-1)] + [(4(n+1)^2 - 4(2n-1)]}{4n^2} = \frac{12n^2}{4n^2} = 3 \tag{A.11a}$$

$$QU34L16: \ \frac{n_{eq}}{n_c} = \frac{[2(2n+1)^2 - (4n-1)] + [(4(n+1)^2 - 4(2n-1)]}{4n^2} = 3 \tag{A.11b}$$

$$QU48L32: \ \frac{n_{eq}}{n_c} = \frac{6[(3n+1)(n+1) - (4n-1)]}{4[(3n+1)(n+1) - (4n-1)]} = \frac{18n^2}{12n^2} = 1.5 \tag{A.11c}$$

From the calculations in Eq. (A.11), we conclude that the constraint ratio *constraint ratio*, for the three element types, is independent of the variable, n, which depicts the number of elements in each direction as shown in Fig. A.1. All the three considered elements, $QU34L4$,

$QU34L16$, and $QU48L32$, satisfy the stability condition ($r_c > 1$) hence, they are not prone to locking. In section 4.1.1, we observe that in the computed results for element $QU34L4$, it is not able to capture the displacement-gradients as compared to the assumed solution whereas elements $QU34L16$ and $QU48L32$ compare very well with the assumed solution. We conclude that the element $QU32L16$ is the optimal choice out of the three elements for our problems as it gives reasonably accurate results for significantly fewer degrees of freedom as compared to $QU48L32$.

A.3 Expressions for MMS

We begin with writing the assumed analytical expressions for non-dimensional displacements, $\bar{u}_1$ and $\bar{u}_2$ in terms of non-dimensional coordinates, $\bar{x}_1$ and $\bar{x}_2$, as mentioned in Eq. (4.1):

$$\begin{gathered} \bar{u}_1 = \bar{x}_1^3\,\bar{x}_2^2\ ,\ \bar{u}_2 = (1-\bar{x}_1^2)\,(1-\bar{x}_2^3) \\ \text{where } \bar{x}_1 = \tfrac{x_1}{L} \text{ and } \bar{x}_2 = \tfrac{x_2}{L}, \bar{u}_1 = \tfrac{u_1}{L} \text{ and } \bar{u}_2 = \tfrac{u_2}{L} \end{gathered} \tag{A.12}$$

Here we find the non-dimensional infinitesimal *strains* ($\bar{\epsilon}_{ij}$) and *strain gradients* ($\bar{\kappa}_{ijk}$) from the assumed displacement field using Eq. (3.2):

$$\begin{aligned} \bar{\epsilon}_{11}(\bar{x}_1,\bar{x}_2) &= 3\bar{x}_1^2\bar{x}_2^2 \\ \bar{\epsilon}_{22}(\bar{x}_1,\bar{x}_2) &= 3\bar{x}_2^2(\bar{x}_1^2-1) \\ \bar{\epsilon}_{12}(\bar{x}_1,\bar{x}_2) &= \bar{x}_1^3\bar{x}_2 + \bar{x}_1(\bar{x}_2^3-1) \end{aligned} \tag{A.13}$$

$$\begin{aligned} &\bar{\kappa}_{111}(\bar{x}_1,\bar{x}_2) = 6\bar{x}_1\bar{x}_2^2\ ;\ \bar{\kappa}_{112}(\bar{x}_1,\bar{x}_2) = 6\bar{x}_1^2\bar{x}_2 \\ &\bar{\kappa}_{221}(\bar{x}_1,\bar{x}_2) = 6\bar{x}_1\bar{x}_2^2\ ;\ \bar{\kappa}_{222}(\bar{x}_1,\bar{x}_2) = 6\bar{x}_2(\bar{x}_1^2-1) \\ &\bar{\kappa}_{211}(\bar{x}_1,\bar{x}_2) = 3\bar{x}_1^2\bar{x}_2 + (\bar{x}_2^3-1)\ ;\ \bar{\kappa}_{212}(\bar{x}_1,\bar{x}_2) = \bar{x}_1^3 + 3\bar{x}_1\bar{x}_2^2 \end{aligned} \tag{A.14}$$

Here we write the obtained expressions for non-dimensional stresses, $\bar{\sigma}_{ij}$ and $\bar{\tau}_{ijk}$ from the constitutive relations, Eq. (3.10), where $\bar{\sigma}_{ij} = \sigma_{ij}/E$ and $\bar{\tau}_{ijk} = \tau_{ijk}/(E \times l_c)$:

$$\begin{aligned}
\bar{\sigma}_{11}(\bar{x}_1, \bar{x}_2) &= -0.77\bar{x}_1^3 - 13.85\bar{x}_1\bar{x}_2^2 + 0.00013\bar{x}_1 \\
\bar{\sigma}_{22}(\bar{x}_1, \bar{x}_2) &= 0.00013\bar{x}_2 - 8.08\bar{x}_2(\bar{x}_1^2 - 1) - 5.77\bar{x}_1^2\bar{x}_2 - 0.77\bar{x}_2^3 + 0.77 \\
\bar{\sigma}_{12}(\bar{x}_1, \bar{x}_2) &= 0.00013\bar{x}_2 - 8.08\bar{x}_2(\bar{x}_1^2 - 1) - 5.77\bar{x}_1^2\bar{x}_2 - 0.77\bar{x}_2^3 + 0.77
\end{aligned} \tag{A.15}$$

$$\begin{aligned}
\bar{\tau}_{111}(\bar{x}_1, \bar{x}_2) &= 0.023\bar{x}_1\bar{x}_2^2 \\
\bar{\tau}_{121}(\bar{x}_1, \bar{x}_2) &= 0.0046\bar{x}_1^2\bar{x}_2 + 0.0015\bar{x}_2^3 - 0.0015 \\
\bar{\tau}_{221}(\bar{x}_1, \bar{x}_2) &= 0.023\bar{x}_1\bar{x}_2^2 \\
\bar{\tau}_{112}(\bar{x}_1, \bar{x}_2) &= 0.007\bar{x}_2(\bar{x}_1^2 - 1) + 0.016\bar{x}_1^2\bar{x}_2 \\
\bar{\tau}_{222}(\bar{x}_1, \bar{x}_2) &= 0.016\bar{x}_2(\bar{x}_1^2 - 1) + 0.007\bar{x}_1^2\bar{x}_2 \\
\bar{\tau}_{122}(\bar{x}_1, \bar{x}_2) &= 0.0015\bar{x}_1^3 + 0.0046\bar{x}_1\bar{x}_2^2
\end{aligned} \tag{A.16}$$

Now we obtain the non-dimensional *body forces* ($\bar{b}_i = b_i/(E \times L \times H)$) that are required to satisfy the equilibrium equations as mentioned in Eq. (3.6):

$$\begin{aligned}
\bar{b}_1(\bar{x}_1, \bar{x}_2) &= -0.77\bar{x}_1^3 - 13.85\bar{x}_1\bar{x}_2^2 + 0.00013\bar{x}_1 \\
\bar{b}_2(\bar{x}_1, \bar{x}_2) &= 0.00013\bar{x}_2 - 8.08\bar{x}_2(\bar{x}_1^2 - 1) - 5.77\bar{x}_1^2\bar{x}_2 - 0.77\bar{x}_2^3 + 0.77
\end{aligned} \tag{A.17}$$

Finally, we write the non-dimensional *classical surface traction* ($\bar{t}_i = t_i/E$) and *higher-order surface traction* ($\bar{r}_i = r_i/(E \times l_c)$) on all four surfaces obtained using Eq. (3.7a) and Eq. (3.7c):

$$
\begin{aligned}
\bar{t}_1^{right}(\bar{x}_1,\bar{x}_2) &= 4.04\bar{x}_2^2 - 0.000042\\
\bar{t}_2^{right}(\bar{x}_1,\bar{x}_2) &= 0.77\bar{x}_2^3 + 0.77\bar{x}_2 - 0.77\\
\bar{r}_1^{right}(\bar{x}_1,\bar{x}_2) &= 0.023\bar{x}_2^2\\
\bar{r}_2^{right}(\bar{x}_1,\bar{x}_2) &= 0.0015\bar{x}_2^3 + 0.0046\bar{x}_2 - 0.0015
\end{aligned}
$$

$$
\begin{aligned}
\bar{t}_1^{left}(\bar{x}_1,\bar{x}_2) &= 1.73\bar{x}_2^2 - 0.000014\\
\bar{t}_2^{left}(\bar{x}_1,\bar{x}_2) &= 0\\
\bar{r}_1^{left}(\bar{x}_1,\bar{x}_2) &= 0\\
\bar{r}_2^{left}(\bar{x}_1,\bar{x}_2) &= 0.0015\bar{x}_2^3 - 0.0015
\end{aligned}
\tag{A.18}
$$

$$
\begin{aligned}
\bar{t}_1^{top}(\bar{x}_1,\bar{x}_2) &= 0.38\bar{x}_1^3 - 0.67\bar{x}_1\\
\bar{t}_2^{top}(\bar{x}_1,\bar{x}_2) &= 1.44\bar{x}_1^2 - 1.01\\
\bar{r}_1^{top}(\bar{x}_1,\bar{x}_2) &= 0.0015\bar{x}_1^3 + 0.0012\bar{x}_1\\
\bar{r}_2^{top}(\bar{x}_1,\bar{x}_2) &= 0.012\bar{x}_1^2 - 0.0081
\end{aligned}
$$

$$
\begin{aligned}
\bar{t}_1^{bottom}(\bar{x}_1,\bar{x}_2) &= 0.38\bar{x}_1^3 + 0.87\bar{x}_1\\
\bar{t}_2^{bottom}(\bar{x}_1,\bar{x}_2) &= 1.01 - 1.44\bar{x}_1^2\\
\bar{r}_1^{bottom}(\bar{x}_1,\bar{x}_2) &= 0.0015\bar{x}_1^3 + 0.0012\bar{x}_1\\
\bar{r}_2^{bottom}(\bar{x}_1,\bar{x}_2) &= 0.0081 - 0.012\bar{x}_1^2
\end{aligned}
$$

A.4 Expressions for shape functions

Within an element e, displacements $\left(u_i^e\right)$, displacement gradients $\left(\beta_{ij}^e\right)$, and Lagrange multipliers $\left(\Lambda_{ij}^e\right)$ can be expressed in terms of their nodal values as:

$$u_i^e(x_1(r,s),x_2(r,s)) = \sum_{a=1}^{n} d_i^a \mathbb{N}_u^a(r,s) \tag{A.19a}$$

$$\beta_{ij}^e(x_1(r,s),x_2(r,s)) = \sum_{a=1}^{m} w_{ij}^a \aleph_\beta^a(r,s) \tag{A.19b}$$

$$\Lambda_{ij}^e(x_1(r,s),x_2(r,s)) = \sum_{a=1}^{p} g_{ij}^a N_\Lambda^a(r,s) \tag{A.19c}$$

$$T_e : \left[x_1 = \sum_{a=1}^{n} x_1^a \mathbb{N}^a(r,s),\ x_2 = \sum_{a=1}^{n} x_2^a \mathbb{N}^a(r,s) \right] \tag{A.19d}$$

where $\mathbb{N}_u, \aleph_\beta$, and N_Λ represent the shape functions for displacements (u_i), displacement gradients (β_{ij}), and Lagrange multipliers (Λ_{ij}), respectively, defined on a master quadrilateral element Ω_M. n, m and p represent the respective number of shape functions for u_i, β_{ij} and Λ_{ij}, respectively, for the considered element-type.

Element $QU34L4 : (n = 9,\ m = 4,\ p = 1)$

For element $QU34L4$ depicted in Fig. A.2, there are six degrees of freedom (DoFs), u_1, u_2, β_{11}, β_{12}, β_{21} and β_{22}, at each corner node, two DoFs, u_1 and u_2, at each of the remaining five nodes, and four Lagrange multipliers, Λ_{11}, Λ_{12}, Λ_{21} and Λ_{22} at the central node resulting in a total of 38 unknowns for the element.

Shape functions for $u_i^e(r,s)$:

$$\begin{aligned}
&\text{Corner nodes}: \ \mathbb{N}^1(r,s) = \tfrac{1}{4}rs(r-1)(s-1);\ \mathbb{N}^2(r,s) = \tfrac{1}{4}rs(s-1)(r+1)\\
&\qquad\qquad \mathbb{N}^3(r,s) = \tfrac{1}{4}rs(r+1)(s+1);\ \mathbb{N}^4(r,s) = \tfrac{1}{4}rs(s+1)(r-1)\\
&\text{Midside nodes}: \ \mathbb{N}^5(r,s) = \tfrac{1}{2}s\left(1-r^2\right)(s-1);\ \mathbb{N}^6(r,s) = \tfrac{1}{2}r\left(1-s^2\right)(r+1)\\
&\qquad\qquad \mathbb{N}^7(r,s) = \tfrac{1}{2}s\left(1-r^2\right)(s+1);\ \mathbb{N}^8(r,s) = \tfrac{1}{2}r\left(1-s^2\right)(r-1)\\
&\text{Middle node}: \ \mathbb{N}^9(r,s) = \left(1-r^2\right)\left(1-s^2\right)
\end{aligned} \tag{A.20}$$

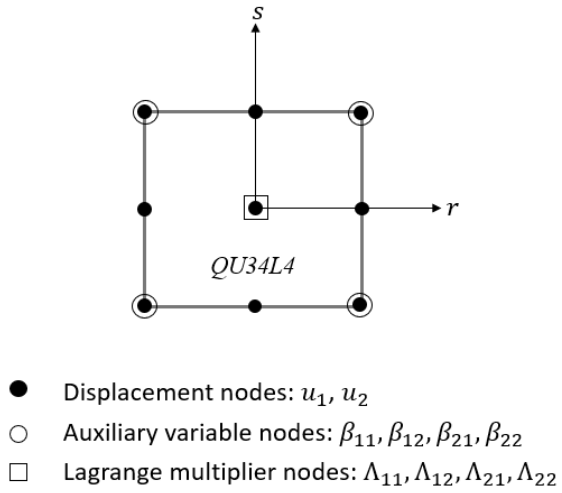

Figure A.2: Sketch of the $QU34L4$ finite element.

Shape functions for $\beta_{ij}^e(r,s)$:

$$\begin{aligned}
\aleph^1(r,s) &= \tfrac{1}{4}(1-r)(1-s) \\
\aleph^2(r,s) &= \tfrac{1}{4}(1+r)(1-s) \\
\aleph^3(r,s) &= \tfrac{1}{4}(1+r)(1+s) \\
\aleph^4(r,s) &= \tfrac{1}{4}(1-r)(1+s)
\end{aligned} \tag{A.21}$$

Please note that $\Lambda_{ij}^e(r,s)'s$ are considered constant within a $QU34L4$ element. Here we write the simultaneous system of linear equations using Eq.(3.22) and Eq.(3.26) for a single element, e, and give the size of the element stiffness matrices:

$$\underbrace{K^e}_{18\times18}\underbrace{d^e}_{18\times1}+\underbrace{(A^e)^T}_{18\times4}\underbrace{g^e}_{4\times1}=\underbrace{F^e}_{18\times1} \tag{A.22a}$$

$$\underbrace{\overline{K^e}}_{16\times16}\underbrace{w^e}_{16\times1}-\underbrace{(M^e)^T}_{16\times4}\underbrace{g^e}_{4\times1}=\underbrace{H^e}_{16\times1} \tag{A.22b}$$

$$\underbrace{A^e}_{4\times18}\underbrace{d^e}_{18\times1}-\underbrace{M^e}_{4\times16}\underbrace{w^e}_{16\times1}=\underbrace{0}_{4\times1} \tag{A.22c}$$

Element $QU34L16$: $(n=9,\ m=4,\ p=4)$

The element $QU34L16$ depicted in Fig. A.3, is exactly the same as $QU34L4$ except that the four Lagrange multipliers, Λ_{11}, Λ_{12}, Λ_{21} and Λ_{22}, are nodal DoFs at the four corner nodes making the total number of unknowns as 50.

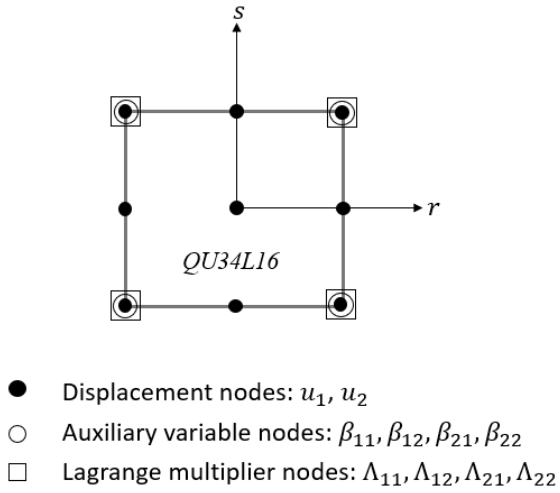

Figure A.3: Sketch of the $QU34L16$ finite element.

Shape functions for $u_i^e(r,s)$ and $\beta_{ij}^e(r,s)$ are same as mentioned in Eq. (A.20) and Eq. (A.21), respectively. Shape functions for $\Lambda_{ij}^e(r,s)$ are given by:

$$\begin{aligned} N^1(r,s) &= \tfrac{1}{4}(1-r)(1-s) \\ N^2(r,s) &= \tfrac{1}{4}(1+r)(1-s) \\ N^3(r,s) &= \tfrac{1}{4}(1+r)(1+s) \\ N^4(r,s) &= \tfrac{1}{4}(1-r)(1+s) \end{aligned} \tag{A.23}$$

Here we write the simultaneous system of linear equations using Eq.(3.22) and Eq.(3.26) for a single element, e, and give the size of the element stiffness matrices:

$$\underbrace{K^e}_{18\times18}\underbrace{d^e}_{18\times1} + \underbrace{(A^e)^T}_{18\times16}\underbrace{g^e}_{16\times1} = \underbrace{F^e}_{18\times1} \tag{A.24a}$$

$$\underbrace{\overline{K^e}}_{16\times16}\underbrace{w^e}_{16\times1} - \underbrace{(M^e)^T}_{16\times16}\underbrace{g^e}_{16\times1} = \underbrace{H^e}_{16\times1} \tag{A.24b}$$

$$\underbrace{A^e}_{16\times18}\underbrace{d^e}_{18\times1} - \underbrace{M^e}_{16\times16}\underbrace{w^e}_{16\times1} = \underbrace{0}_{16\times1} \tag{A.24c}$$

Element $QU48L32 : (n = m = p = 8)$

For the element $QU48L32$, depicted in Fig. A.4, there is no node at the centroid, all $u_i's$, $\beta_{ij}'s$ and $\Lambda_{ij}'s$ are taken as unknowns at each of the 8 nodes giving rise to 80 unknowns.

For the 8-noded serendipity element, $QU48L32$, the shape functions are the same for all three unknowns, hence $\mathbb{N}_u = \aleph_\beta = N_\Lambda = N^i$, where N^i's are given by:

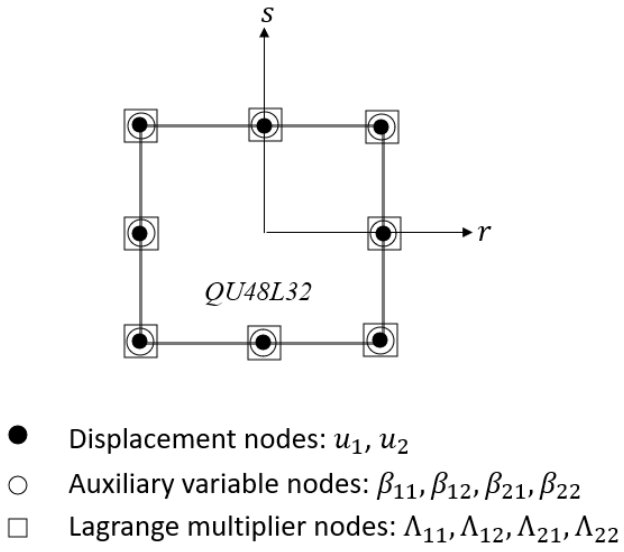

Figure A.4: Sketch of the $QU48L32$ finite element.

$$
\begin{aligned}
N^1(r,s) &= -\tfrac{1}{4}(1-r)(1-s)(1+r+s) \\
N^2(r,s) &= -\tfrac{1}{4}(1+r)(1-s)(1-r+s) \\
N^3(r,s) &= -\tfrac{1}{4}(1+r)(1+s)(1-r-s) \\
N^4(r,s) &= -\tfrac{1}{4}(1-r)(1+s)(1+r-s) \\
N^5(r,s) &= \tfrac{1}{2}\left(1-r^2\right)(1-s) \\
N^6(r,s) &= \tfrac{1}{2}(1+r)\left(1-s^2\right) \\
N^7(r,s) &= \tfrac{1}{2}\left(1-r^2\right)(1+s) \\
N^8(r,s) &= \tfrac{1}{2}(1-r)\left(1-s^2\right)
\end{aligned}
\tag{A.25}
$$

Here we write the simultaneous system of linear equations using Eq.(3.22) and Eq.(3.26) for a single element, e, and give the size of the element stiffness matrices:

$$\underbrace{K^e}_{16\times16}\underbrace{d^e}_{16\times1}+\underbrace{(A^e)^T}_{16\times32}\underbrace{g^e}_{32\times1}=\underbrace{F^e}_{16\times1} \tag{A.26a}$$

$$\underbrace{\overline{K^e}}_{32\times32}\underbrace{w^e}_{32\times1}-\underbrace{(M^e)^T}_{32\times32}\underbrace{g^e}_{32\times1}=\underbrace{H^e}_{32\times1} \tag{A.26b}$$

$$\underbrace{A^e}_{32\times16}\underbrace{d^e}_{16\times1}-\underbrace{M^e}_{32\times32}\underbrace{w^e}_{32\times1}=\underbrace{0}_{32\times1} \tag{A.26c}$$

A.5 Iterative procedure

Here we discuss the iterative procedure, proposed by [43], used for element $QU34L4$, where Lagrange multiplier is associated only with a single node located at the element centroid, i.e., Lagrange multipliers are considered constant within an element.

The system of simultaneous algebraic equations in terms of global matrices can be written using Eq.(3.26) as:

$$\boldsymbol{K}_g\,\boldsymbol{U}=\boldsymbol{F}_g$$

$$\text{That is, } \begin{bmatrix} \boldsymbol{K} & \boldsymbol{0} & \boldsymbol{A}^T \\ \boldsymbol{0} & \overline{\boldsymbol{K}} & -\boldsymbol{M}^T \\ \boldsymbol{A} & -\boldsymbol{M} & \boldsymbol{0} \end{bmatrix} \begin{bmatrix} \boldsymbol{d} \\ \boldsymbol{w} \\ \boldsymbol{g} \end{bmatrix} = \begin{bmatrix} \boldsymbol{F} \\ \boldsymbol{H} \\ \boldsymbol{0} \end{bmatrix} \tag{A.27}$$

where $\boldsymbol{d}=\{d_1,\ d_2\}^T$, $\boldsymbol{e}=\{w_{11},\ w_{12},\ w_{21},\ w_{22}\}^T$, and $\boldsymbol{g}=\{g_{11},\ g_{12},\ g_{21},\ g_{22}\}^T$

Starting from the first equation of the system (A.27), direct solution is possible for nodal

displacements, $\boldsymbol{d}$, because $\boldsymbol{K}$ is invertible, hence we get:

$$\boldsymbol{d} = \boldsymbol{K}^{-1}(\boldsymbol{F} - \boldsymbol{A}^T\boldsymbol{g}) \quad \Rightarrow \quad \boldsymbol{d}^{n+1} = \boldsymbol{K}^{-1}\left(\boldsymbol{F} - \boldsymbol{A}^T\boldsymbol{g}^{n+1}\right) \tag{A.28}$$

For the second equation of the system (A.27), the nodal displacement-gradients, $\boldsymbol{w}$, are determined with a minimum residual-based iterative solver, *minres*, as the stiffness matrix $\overline{\boldsymbol{K}}$ is singular. We get:

$$\boldsymbol{w} = minres(\overline{\boldsymbol{K}},\ \boldsymbol{H} + \boldsymbol{M}^T\boldsymbol{g}) \quad \Rightarrow \quad \boldsymbol{w}^{n+1} = minres\left(\overline{\boldsymbol{K}},\ \boldsymbol{H} + \boldsymbol{M}^T\boldsymbol{g}^{n+1}\right) \tag{A.29}$$

For the third equation of the system (A.27), we use a general procedure and write:

$$\boldsymbol{g}^{n+1} = \boldsymbol{g}^n - \rho\boldsymbol{r}^n \quad where \quad \boldsymbol{r}^n = \boldsymbol{A}\boldsymbol{d}^n - \boldsymbol{M}\boldsymbol{w}^n \tag{A.30}$$

where ρ is a scalar called the accelerator parameter. Although the algorithm is generally applicable but a suitable choice of the convergence accelerator ρ has to be made in order to get not only convergence but also the best rate of convergence and to keep step (A.30) as simple as possible. For a constant ρ and a symmetrical positive definite matrix $\boldsymbol{K}$, ρ has to satisfy the following [47]:

$$0 < \rho < 1/\beta^2 \tag{A.31}$$

$1/\beta^2$ is the maximum eigenvalue of the matrix $\boldsymbol{M}^T\boldsymbol{K}^{-1}\boldsymbol{M}$. For an unsymmetrical matrix A, which is positive definite, (A.31) is still valid when $\boldsymbol{K}$ is replaced by its symmetrical part.

Appendix B

MATLAB codes

B.1 Solution using *mldivide* : direct solver

MATLAB code for an isotropic cantilever beam bending with a parabolic shear traction at the right edge (using $QU34L16$).

```
1
2 %% QU34L16 ELEMENT
3
4 %STRAIN GRADIENT PLANE STRAIN PROBLEM%
5 %CANTILEVER BEAM BENDING%
6
7 %(2 DISPLACEMENTS: EQUILIBRIUM EQUATIONS): 9 NODES
8 %(4 DISPLACEMENT DERIVATIVES: aux-"e") : 4 NODES
9 %(4 Lagrange multiplies: "g") : 4 NODE
10
11 %% 9-NODED QUADRILATERAL ELEMENT%
12
13 clc
14 clear
15
16 %% ELEMENTS AND NODES
```

```
17
18 Nx=20;  %make it always even% %for neutral axis plotting: even
19 Ny=10;
20
21 %9-noded
22 nx1=2*Nx+1;
23 ny1=2*Ny+1;
24 %4-noded
25 nx2=Nx+1;
26 ny2=Ny+1;
27
28 noE=Nx*Ny;
29 noN=nx1*ny1;
30 noN2=nx2*ny2;
31 % doF=10; %each node
32 TdoF=2*noN+4*noN2+4*noN2;
33
34 %%  MATERIAL PROPERTIES AND MATRIX
35
36 E1=200*(10^9);
37 nyu=0.3;
38
39 %for plane strain
40 lambda=E1*nyu/((1+nyu)*(1-2*nyu));
41 mu=E1/(2*(1+nyu));
42
43 cl=2*(10^(-3));                    %% characteristic length
44
45 D11=lambda+2*mu;
46 D22=lambda+2*mu;
47 D12=lambda;
```

```
48 D33=mu;
49 D44=(cl^2)*(lambda+2*mu);
50 D46=(cl^2)*lambda;
51 D55=(cl^2)*(lambda+2*mu);
52 D57=(cl^2)*lambda;
53 D66=(cl^2)*(lambda+2*mu);
54 D77=(cl^2)*(lambda+2*mu);
55 D88=(cl^2)*mu;
56 D99=(cl^2)*mu;
57
58 %% BODY DIMENSIONS AND INERTIA
59
60 L=1;   %L=B=2 cuz -1<r,s<1
61 H=0.1; %L/3;
62
63 %% SHAPE FUNCTIONS AND THEIR DERIVATIVES:
64
65 syms r s
66 N4=[(1-r)*(1-s)/4,(1+r)*(1-s)/4,(1+r)*(1+s)/4,(1-r)*(1+s)/4];
67 Nd4=[diff(N4,r);diff(N4,s)];
68 N9=[r*s*(s-1)*(r-1)/4,r*s*(s-1)*(1+r)/4,r*s*(s+1)*(r+1)/4, ...
69     r*s*(s+1)*(r-1)/4,s*(s-1)*(1-r^2)/2,r*(1-s^2)*(1+r)/2, ...
70     s*(1+s)*(1-r^2)/2,r*(1-s^2)*(r-1)/2,(1-r^2)*(1-s^2)];
71 Nd9=[diff(N9,r);diff(N9,s)];
72
73 %% NODAL COORDINATES
74
75 %9-noded
76 k=1;
77 for i=1:1:ny1
78     yc=-H/2+(i-1)*(H/Ny)/2;
```

```
79      for j=1:1:nx1
80      Xc(k,1)=(j-1)*(L/Nx)/2;
81      Yc(k,1)=yc;
82      k=k+1;
83      end
84 end
85
86 %4-noded
87 k=1;
88 for i=1:1:ny2
89      yc2=-H/2+(i-1)*H/Ny; %removed -H/2
90      for j=1:1:nx2
91      Xc2(k,1)=(j-1)*L/Nx;
92      Yc2(k,1)=yc2;
93      k=k+1;
94      end
95 end
96
97 %% Q9: ELEMENT CONNECTIVITY
98
99 %9-NODED
100 %fix gives quotient(/) and mod(,) gives remainder%
101 for i=1:1:Nx*Ny
102   if (i>Nx) && (rem(i,Nx)==0)
103      var=2*nx1*(fix(i/Nx)-1)+2*Nx-1;
104   else if i>Nx
105      var=2*nx1*fix(i/Nx)+2*mod(i,Nx)-1;
106   else
107      var=2*i-1;
108   end
109   end
```

```
110       connect(i,1)=var;
111       connect(i,2)=connect(i,1)+2;
112       connect(i,3)=connect(i,1)+nx1+nx1+2;
113       connect(i,4)=connect(i,3)-2;
114       connect(i,5)=connect(i,1)+1;
115       connect(i,6)=var+nx1+2;
116       connect(i,7)=connect(i,3)-1;
117       connect(i,8)=connect(i,6)-2;
118       connect(i,9)=connect(i,1)+nx1+1;
119 end
120 connect;
121 % 4-NODED*
122 %fix gives quotient(/) and mod(,) gives remainder%
123 for i=1:1:Nx*Ny
124     if (i>Nx) && (rem(i,Nx)==0)
125       connect2(i,1)=i+fix(i/Nx)-1;
126       connect2(i,2)=i+1+fix(i/Nx)-1;
127       connect2(i,3)=i+1+nx2+fix(i/Nx)-1;
128       connect2(i,4)=i+nx2+fix(i/Nx)-1;
129       else if i>Nx
130       connect2(i,1)=i+fix(i/Nx);
131       connect2(i,2)=i+1+fix(i/Nx);
132       connect2(i,3)=i+1+nx2+fix(i/Nx);
133       connect2(i,4)=i+nx2+fix(i/Nx);
134       else
135       connect2(i,1)=i;
136       connect2(i,2)=i+1;
137       connect2(i,3)=i+1+nx2;
138       connect2(i,4)=i+nx2;
139       end
140       end
```

```
141 end
142 connect2;
143
144 %% JACOBIAN FOR UNIFORM RECTANGULAR ELEMENTS
145
146 J=[L/(2*Nx),0;0,H/(2*Ny)];
147 J_inv=inv(J);
148
149 for i=1:1:9
150  N19(i)=Nd9(1,i)*J_inv(1,1)+Nd9(2,i)*J_inv(2,1);
151  N29(i)=Nd9(1,i)*J_inv(1,2)+Nd9(2,i)*J_inv(2,2);
152 end
153 for i=1:1:4
154  N14(i)=Nd4(1,i)*J_inv(1,1)+Nd4(2,i)*J_inv(2,1);
155  N24(i)=Nd4(1,i)*J_inv(1,2)+Nd4(2,i)*J_inv(2,2);
156 end
157
158 %% 9-NODED
159
160 s1=transpose(N19)*N19*det(J);
161 s2=transpose(N19)*N29*det(J);
162 s3=transpose(N29)*N19*det(J);
163 s4=transpose(N29)*N29*det(J);
164 s5=transpose(N19)*N4*det(J);
165 s6=transpose(N29)*N4*det(J);
166
167 %% GAUSS QUADRATURE RULE [3 X 3] (weights and abscissa read from an ...
      excel file):
168 % data = readtable('excelfile filenmae','Sheet','3');
169
170 A = table2array(data);
```

```
171 ip=3; %no: of integration points along each axis
172 k11=zeros(9); k12=zeros(9); k21=zeros(9);
173 k22=zeros(9); b1=zeros(9,4); b2=zeros(9,4);
174 for m=1:1:ip
175     for n=1:1:ip
176     k11=k11+A(n,1)*A(m,1)*subs(subs(s1,r,A(m,2)),s,A(n,2));
177     k12=k12+A(n,1)*A(m,1)*subs(subs(s2,r,A(m,2)),s,A(n,2));
178     k21=k21+A(n,1)*A(m,1)*subs(subs(s3,r,A(m,2)),s,A(n,2));
179     k22=k22+A(n,1)*A(m,1)*subs(subs(s4,r,A(m,2)),s,A(n,2));
180     b1=b1+A(n,1)*A(m,1)*subs(subs(s5,r,A(m,2)),s,A(n,2));
181     b2=b2+A(n,1)*A(m,1)*subs(subs(s6,r,A(m,2)),s,A(n,2));
182     end
183 end
184
185 K11=zeros(noN);
186 K12=zeros(noN);
187 K21=zeros(noN);
188 K22=zeros(noN);
189
190 for k=1:1:Nx*Ny
191   D=connect(k,:);
192     for i=1:1:9
193         for j=1:1:9
194         a=D(1,i);
195         b=D(1,j);
196             K11(a,b)=K11(a,b)+k11(i,j);
197             K12(a,b)=K12(a,b)+k12(i,j);
198             K21(a,b)=K21(a,b)+k21(i,j);
199             K22(a,b)=K22(a,b)+k22(i,j);
200             end
201         end
```

```
202 end
203
204 %% 4-NODED
205
206 s4=transpose(N4)*N4*det(J);
207 s24=transpose(N14)*N14*det(J);
208 s34=transpose(N14)*N24*det(J);
209 s44=transpose(N24)*N14*det(J);
210 s54=transpose(N24)*N24*det(J);
211
212 %% GAUSS QUADRATURE RULE [3 X 3] (weights and abscissa read from an ...
       excel file):
213 % data = readtable('excel filename','Sheet','2');
214 A = table2array(data);
215 ip=2; %no: of integration points along each axis
216 m4=zeros(4); k114=zeros(4); k124=zeros(4);
217 k214=zeros(4); k224=zeros(4);
218 for m=1:1:ip
219     for n=1:1:ip
220     m4=m4+A(n,1)*A(m,1)*subs(subs(s4,r,A(m,2)),s,A(n,2));
221     k114=k114+A(n,1)*A(m,1)*subs(subs(s24,r,A(m,2)),s,A(n,2));
222     k124=k124+A(n,1)*A(m,1)*subs(subs(s34,r,A(m,2)),s,A(n,2));
223     k214=k214+A(n,1)*A(m,1)*subs(subs(s44,r,A(m,2)),s,A(n,2));
224     k224=k224+A(n,1)*A(m,1)*subs(subs(s54,r,A(m,2)),s,A(n,2));
225     end
226 end
227
228 M4=zeros(noN2);
229 K114=zeros(noN2);
230 K124=zeros(noN2);
231 K214=zeros(noN2);
```

```
232 K224=zeros(noN2);
233
234 for k=1:1:Nx*Ny
235   D=connect2(k,:);
236     for i=1:1:4
237         for j=1:1:4
238         a=D(1,i);
239         b=D(1,j);
240             M4(a,b)=M4(a,b)+m4(i,j);
241             K114(a,b)=K114(a,b)+k114(i,j);
242             K124(a,b)=K124(a,b)+k124(i,j);
243             K214(a,b)=K214(a,b)+k214(i,j);
244             K224(a,b)=K224(a,b)+k224(i,j);
245             end
246         end
247 end
248
249 B1=zeros(noN,noN2);
250 B2=zeros(noN,noN2);
251 for k=1:1:Nx*Ny
252   D=connect(k,:);
253   D2=connect2(k,:);
254     for i=1:1:9
255         for j=1:1:4
256         a=D(1,i);
257         b=D2(1,j);
258             B1(a,b)=B1(a,b)+b1(i,j);
259             B2(a,b)=B2(a,b)+b2(i,j);
260             end
261         end
262 end
```

```
263
264 Z1=zeros(noN,noN2);
265 Z2=zeros(noN2);
266
267 %% GLOBAL STIFFNESS MATRIX
268
269 KG=[D11*K11+D33*K22,D33*K21+D12*K12,Z1,Z1,Z1,Z1,B1,B2,Z1,Z1;
270       D12*K21+D33*K12,D33*K11+D22*K22,Z1,Z1,Z1,Z1,Z1,Z1,B1,B2;
271       Z1',Z1',D44*K114,D55*K214,D46*K124,D57*K224,-M4,Z2,Z2,Z2;
272       Z1',Z1',D88*K124,D99*K224,D88*K114,D99*K214,Z2,-M4,Z2,Z2;
273       Z1',Z1',D88*K124,D99*K224,D88*K114,D99*K214,Z2,Z2,-M4,Z2;
274       Z1',Z1',D46*K114,D57*K214,D66*K124,D77*K224,Z2,Z2,Z2,-M4;
275       B1',Z1',-M4,Z2,Z2,Z2,Z2,Z2,Z2,Z2;
276       B2',Z1',Z2,-M4,Z2,Z2,Z2,Z2,Z2,Z2;
277       Z1',B1',Z2,Z2,-M4,Z2,Z2,Z2,Z2,Z2;
278       Z1',B2',Z2,Z2,Z2,-M4,Z2,Z2,Z2,Z2];
279
280 %% ESSENTIAL BOUNDARY CONDITIONS: USING PENALTY METHOD
281
282 % new=zeros(1,TdoF);
283 gamma=1e30;
284 %% LEFT END FIXED: u1=u2=0
285
286 for i=1:1:noN
287    if Xc(i,1)==0
288         KG(i,i)=KG(i,i)+gamma; %u1
289         KG(i+noN,i+noN)=KG(i+noN,i+noN)+gamma; %u2
290         end
291 end
292 % LEFT END FIXED: q1=q3=0
293    for i=1:1:noN2
```

```
294     if Xc2(i,1)==0
295         KG(i+2*noN,i+2*noN)=KG(i+2*noN,i+2*noN)+gamma; %q1=e11
296         KG(i+2*noN+2*noN2,i+2*noN+2*noN2)=KG(i+2*noN+2*noN2, ... ...
                i+2*noN+2*noN2)+gamma; %q3=e21
297     end
298     end
299
300 %% RIGHT EDGE SURFACE TRACTION: PARABOLIC DISTRIBUTION%
301
302 F = zeros(TdoF,1);
303 P0 = 1e9;
304
305 t2R = @(x2) -3*P0*(1-((2*x2)/H).^2)/2*H;
306
307 for i=Nx:Nx:Nx*Ny  %RIGHT
308 J2=[L/(2*Nx),0;0,H/(2*Ny)];
309 py=0;
310 for j=1:1:9
311     py=py+N9(j)*Yc(connect(i,j), 1);
312 end
313 t2_not=t2R(py);
314 Nright=[N9(2),N9(6),N9(3)]';
315 INT2=int(subs(t2_not*Nright*J2(2,2),r,1),s,-1,1);
316
317 order= [2 6 3]';
318     for k=1:3
319         p=order(k,1);
320         b=connect(i,p)+noN;
321         F(b,1)=F(b,1)+INT2(k,1);
322     end
323 end
```

```
F;

X=KG\F;
```

B.2 Plotting

MATLAB code for plotting surface traction t_1, t_2, r_1 and r_2 at the right edge for an isotropic material.

```
%-------------------------------------------------------------------
%   plot t1,t2,r1 and r2 for isotropic material (horizontal)
%-------------------------------------------------------------------

L=1;
H=0.1;

Nx=100;
Ny=20;

%9-noded
 nx1=2*Nx+1;
 ny1=2*Ny+1;
%4-noded
 nx2=Nx+1;
 ny2=Ny+1;

 noE=Nx*Ny;
```

```
noN=nx1*ny1;
noN2=nx2*ny2;
% doF=10; %each node
TdoF=2*noN+4*noN2+4*noN2;

%%  MATERIAL PROPERTIES AND MATRIX

cl=2*(10^(-3));                         %%% characteristic length

%% FOR TRANSVERSELY ISOTROPIC MATERIAL

% E1 = 100*1e9;
% E2 = 4*1e9;
% G12 = 2*1e9;
% V12 = 0.25;
% V23 = V12; %*E2/E1;

% C11 = 1/E1;
% C12 = -V12/E1;
% C22 = 1/E2;
% C23 = -V23/E2;
%
% CV = C11*C22*C22 - C11*C23*C23 - C22*C12*C12 - C22*C12*C12 + ...
      2*C12*C23*C12;
%
% D11 = (C22*C22 - C23*C23)/CV;
% D12 = (C12*C23 - C12*C22)/CV;
% D22 = (C22*C11 - C12*C12)/CV;
% D33 = G12;

% D44=(cl^2)*D11;
```

```
% D46=(cl^2)*D12;
% D55=(cl^2)*D11;
% D57=(cl^2)*D12;
% D66=(cl^2)*D22;
% D77=(cl^2)*D22;
% D88=(cl^2)*D33;
% D99=(cl^2)*D33;

%-------------------------------------------------------------------------%
% MATERIAL PROPERTIES AND MATRIX
%-------------------------------------------------------------------------%
 cl=2*(10^(-3));                    %%% characteristic length

E=200*10^9;    % for iso material
 v=0.3;

 Q11=E/(1+v)/(1-2*v)*(1-v);
 Q12=E/(1+v)/(1-2*v)*v;
 Q22=E/(1+v)/(1-2*v)*(1-v);
 Q66=E/(1+v)/(1-2*v)*(0.5-v);

% Q11 = D11; Q22= D22; Q12 =D12; Q66 = D33;

MATQ=[Q11 Q12 0; Q12 Q22 0; 0 0 Q66];

 Qzero=zeros(3,3);
MATQ2=cl^2*[MATQ Qzero; Qzero MATQ];

%% Q9: ELEMENT CONNECTIVITY

%9-NODED
```

```
%fix gives quotient(/) and mod(,) gives remainder%
for i=1:1:Nx*Ny
  if (i>Nx) && (rem(i,Nx)==0)
    var=2*nx1*(fix(i/Nx)-1)+2*Nx-1;
  else if i>Nx
    var=2*nx1*fix(i/Nx)+2*mod(i,Nx)-1;
  else
    var=2*i-1;
  end
  end
    connect(i,1)=var;
    connect(i,2)=connect(i,1)+2;
    connect(i,3)=connect(i,1)+nx1+nx1+2;
    connect(i,4)=connect(i,3)-2;
    connect(i,5)=connect(i,1)+1;
    connect(i,6)=var+nx1+2;
    connect(i,7)=connect(i,3)-1;
    connect(i,8)=connect(i,6)-2;
    connect(i,9)=connect(i,1)+nx1+1;
end
connect;
% 4-NODED*
%fix gives quotient(/) and mod(,) gives remainder%
for i=1:1:Nx*Ny
   if (i>Nx) && (rem(i,Nx)==0)
    connect2(i,1)=i+fix(i/Nx)-1;
    connect2(i,2)=i+1+fix(i/Nx)-1;
    connect2(i,3)=i+1+nx2+fix(i/Nx)-1;
    connect2(i,4)=i+nx2+fix(i/Nx)-1;
    else if i>Nx
    connect2(i,1)=i+fix(i/Nx);
```

```
112       connect2(i,2)=i+1+fix(i/Nx);
113       connect2(i,3)=i+1+nx2+fix(i/Nx);
114       connect2(i,4)=i+nx2+fix(i/Nx);
115       else
116       connect2(i,1)=i;
117       connect2(i,2)=i+1;
118       connect2(i,3)=i+1+nx2;
119       connect2(i,4)=i+nx2;
120       end
121       end
122 end
123 connect2;
124 %% SHAPE FUNCTIONS AND THEIR DERIVATIVES:
125
126 syms r s
127 N4=[(1-r)*(1-s)/4,(1+r)*(1-s)/4,(1+r)*(1+s)/4,(1-r)*(1+s)/4];
128 Nd4=[diff(N4,r);diff(N4,s)];
129 N9=[r*s*(s-1)*(r-1)/4,r*s*(s-1)*(1+r)/4,r*s*(s+1)*(r+1)/4,...
130       r*s*(s+1)*(r-1)/4,s*(s-1)*(1-r^2)/2,r*(1-s^2)*(1+r)/2,...
131       s*(1+s)*(1-r^2)/2,r*(1-s^2)*(r-1)/2,(1-r^2)*(1-s^2)];
132 Nd9=[diff(N9,r);diff(N9,s)];
133
134 % horizontal line near H/2 for plotting t1,t2,r1 and r2
135 gg=Nx;
136 S11v=zeros(gg,1);
137 S22v=zeros(gg,1);
138 S12v=zeros(gg,1);
139
140 T111v=zeros(gg,1);
141 T221v=zeros(gg,1);
142 T121v=zeros(gg,1);
```

```
143 T112v=zeros(gg,1);
144 T222v=zeros(gg,1);
145 T122v=zeros(gg,1);
146
147 T1111v=zeros(gg,1);
148 T1112v=zeros(gg,1);
149 T2211v=zeros(gg,1);
150 T2212v=zeros(gg,1);
151 T1211v=zeros(gg,1);
152 T1212v=zeros(gg,1);
153 T1121v=zeros(gg,1);
154 T1122v=zeros(gg,1);
155 T2221v=zeros(gg,1);
156 T2222v=zeros(gg,1);
157 T1221v=zeros(gg,1);
158 T1222v=zeros(gg,1);
159
160 Xv=zeros(gg,1);
161 Yv=zeros(gg,1);
162
163 t2rightES=zeros(gg,1);
164 t1rightES=zeros(gg,1);
165
166 r1rightES=zeros(gg,1);
167 r2rightES=zeros(gg,1);
168
169 ii=1;
170 for i=Nx*(Ny/2-1)+1:Nx*Ny/2  %% near center (H/2)
171 %    for i=Nx/2:Nx:Nx*Ny-Nx/2  %% mid (L/2)
172 % for i=Nx:Nx:Nx*Ny  %% right surface
173 % for i=1:Nx:Nx*(Ny-1)+1  %% left surface
```

```
174
175     LxE=Xc(connect(i,2),1)-Xc(connect(i,1),1);
176     LyE=Yc(connect(i,3),1)-Yc(connect(i,2),1);
177   xr=LxE/2;
178     ys=LyE/2;
179     rx=1/xr;
180     sy=1/ys;
181
182     e11E=0;
183     e12E=0;
184     e21E=0;
185     e22E=0;
186     XE=0;
187     YE=0;
188     for j=1:9
189         XE=XE+N9(j)*Xc(connect(i,j),1);
190         YE=YE+N9(j)*Yc(connect(i,j),1);
191     end
192     for j=1:4
193         e11E=e11E+N4(j)*X(connect2(i,j)+2*noN,1);
194         e12E=e12E+N4(j)*X(connect2(i,j)+2*noN+noN2,1);
195         e21E=e21E+N4(j)*X(connect2(i,j)+2*noN+2*noN2,1);
196         e22E=e22E+N4(j)*X(connect2(i,j)+2*noN+3*noN2,1);
197     end
198     % derivative of e terms in each element %
199     e111E=diff(e11E,r)*rx; %+diff(e11E,s)*sx
200     e112E=diff(e11E,s)*sy;
201     e221E=diff(e22E,r)*rx;
202     e222E=diff(e22E,s)*sy;
203     e121E=diff(e12E,r)*rx;
204     e122E=diff(e12E,s)*sy;
```

```
205     e211E=diff(e21E,r)*rx;
206     e212E=diff(e21E,s)*sy;
207
208     strain11E=e11E;
209     strain22E=e22E;
210     strain12E=(e12E+e21E);
211
212     strainvecE=[strain11E.';strain22E.';strain12E.'];
213     stressvecE=MATQ*strainvecE;
214
215     S11v(ii,1)=subs(stressvecE(1,1),[r,s],[0,0]);
216     S22v(ii,1)=subs(stressvecE(2,1),[r,s],[0,0]);
217     S12v(ii,1)=subs(stressvecE(3,1),[r,s],[0,0]);
218
219     k111E=e111E;
220     k221E=e221E;
221     k121E=(e121E+e211E);
222     k112E=e112E;
223     k222E=e222E;
224     k122E=(e122E+e212E);
225
226     strainGvecE=[k111E.';k221E.';k121E.';k112E.';k222E.';k122E.'];
227     HOstressvecE=MATQ2*strainGvecE;
228
229     T111v(ii,1)=subs(HOstressvecE(1,1),[r,s],[0,0]);
230     T221v(ii,1)=subs(HOstressvecE(2,1),[r,s],[0,0]);
231     T121v(ii,1)=subs(HOstressvecE(3,1),[r,s],[0,0]);
232     T112v(ii,1)=subs(HOstressvecE(4,1),[r,s],[0,0]);
233     T222v(ii,1)=subs(HOstressvecE(5,1),[r,s],[0,0]);
234     T122v(ii,1)=subs(HOstressvecE(6,1),[r,s],[0,0]);
235
```

```
236     T1111E=diff(HOstressvecE(1,1),r)*rx;
237     T1112E=diff(HOstressvecE(1,1),s)*sy;
238
239     T2211E=diff(HOstressvecE(2,1),r)*rx;
240     T2212E=diff(HOstressvecE(2,1),s)*sy;
241
242     T1211E=diff(HOstressvecE(3,1),r)*rx;
243     T1212E=diff(HOstressvecE(3,1),s)*sy;
244
245     T1121E=diff(HOstressvecE(4,1),r)*rx;
246     T1122E=diff(HOstressvecE(4,1),s)*sy;
247
248     T2221E=diff(HOstressvecE(5,1),r)*rx;
249     T2222E=diff(HOstressvecE(5,1),s)*sy;
250
251     T1221E=diff(HOstressvecE(6,1),r)*rx;
252     T1222E=diff(HOstressvecE(6,1),s)*sy;
253
254     T1111v(ii,1)=subs(T1111E,[r,s],[0,0]);
255     T1122v(ii,1)=subs(T1122E,[r,s],[0,0]);
256     T1212v(ii,1)=subs(T1212E,[r,s],[0,0]);
257
258     T1211v(ii,1)=subs(T1211E,[r,s],[0,0]);
259     T1222v(ii,1)=subs(T1222E,[r,s],[0,0]);
260     T2212v(ii,1)=subs(T2212E,[r,s],[0,0]);
261
262     T1121v(ii,1)=subs(T1121E,[r,s],[0,0]);
263     T1221v(ii,1)=subs(T1221E,[r,s],[0,0]);
264
265     Xv(ii,1)=subs(XE,[r,s],[0,0]);
266     Yv(ii,1)=subs(YE,[r,s],[0,0]);
```

```
267
268         ii=ii+1;
269 end
270
271 %right
272 t1rightES=S11v-T1111v-T1122v-T1212v;
273 t2rightES=S12v-T1211v-T1222v-T2212v;
274 r1rightES=T111v;
275 r2rightES=T121v;
276
277 %top
278 % t1rightES=S12v-T1211v-T1222v-T1121v;
279 % t2rightES=S22v-T2211v-T2222v-T1221v;
280 % r1rightES=T122v;
281 % r2rightES=T222v;
282
283 %  plot figures  %%
284
285 %Plotting horizontally or vertically (through the thickness)
286 norm=1;
287 axis=Xv/norm;
288
289 %% Plotting displacements: u1 and u2
290 k=1;
291 for  i=1:1:noN  %mid-surface-hor%
292         if Yc(i,1)==0
293         U1mid(k,1)=X(i,1);
294         U2mid(k,1)=X(i+noN,1);
295         Xval(k,1)=Xc(i,1);
296         k=k+1;
297         end
```

```
298 end
299 % error1=max(e1)%/Ny;
300
301  figure(1)
302  plot(Xval,U1mid)
303  hold on
304 % title('Mid-surface deflection vs $\displaystyle ...
      x_{1}$','interpreter','latex')
305 % ylabel('$\displaystyle u_{1}(x_{1},0)(m)$','interpreter','latex')
306 % xlabel('$\displaystyle x_{11}$','interpreter','latex')
307 % legend('MMS','Present: 4 X 4','Present: 8 X 8','Location','SouthWest')
308
309 figure(2)
310 plot(Xval,U2mid)
311 hold on
312 % title('Mid-surface deflection vs $\displaystyle ...
      x_{1}$','interpreter','latex')
313 %ylabel('$\displaystyle u_{2}(x_{1},0)(m)$','interpreter','latex')
314 %xlabel('$\displaystyle x_{1}/L$','interpreter','latex)
315 %legend('$l_{c}=2\;mm$','$l_{c}=6\;mm$','$l_{c}=10\;mm$','Interpreter','latex');
316 % legend('MMS','Present: 4 X 4','Present: 12 X 12','Location','SouthWest')
317
318 %-------------------------------------------------------------
319 %   Plotting Surface traction:
320 %-------------------------------------------------------------
321
322 t1rightES=S11v-T1111v-T1122v-T1212v;
323 t2rightES=S12v-T1211v-T1222v-T2212v;
324 r1rightES=T111v;
325 r2rightES=T121v;
326
```

```
figure(29)
plot(axis,t1rightES)
hold on
%ylabel('$\displaystyle t_{1}(x_{1},-0.0417H) (Pa)$','interpreter','latex')
%xlabel('$\displaystyle x_{1}/L$','interpreter','latex')
%legend('$l_{c}=2\;mm$','$l_{c}=6\;mm$','$l_{c}=10\;mm$','Interpreter','latex');
% legend('40 X 20','60 X 30','80 X 20','Location','SouthWest')
% legend('cl = 2 mm','cl = 4 mm','cl = 6 mm','Location','SouthWest')
% xlim([0,1]);

figure(30)
plot(axis,t2rightES)
hold on
%ylabel('$\displaystyle t_{2}(x_{1},-0.0417H) (Pa)$','interpreter','latex')
%xlabel('$\displaystyle x_{1}/L$','interpreter','latex')
%legend('$l_{c}=2\;mm$','$l_{c}=6\;mm$','$l_{c}=10\;mm$','Interpreter','latex');
% legend('40 X 20','60 X 30','80 X 20','Location','SouthWest')
% legend('cl = 2 mm','cl = 4 mm','cl = 6 mm','Location','SouthWest')
% xlim([0,1]);

figure(31)
plot(axis,r1rightES)
hold on
%ylabel('$\displaystyle r_{1}(x_{1},-0.0417H) ...
    (Pa.m)$','interpreter','latex')
%xlabel('$\displaystyle % x_{1}/L$','interpreter','latex')
% ...
    legend('$l_{c}=2\;mm$','$l_{c}=6\;mm$','$l_{c}=10\;mm$','Interpreter','latex');
% legend('40 X 20','60 X 30','80 X 20','Location','SouthWest')
% legend('cl = 2 mm','cl = 4 mm','cl = 6 mm','Location','SouthWest')
% xlim([0,1]);
```

```
356
357 figure(32)
358 plot(axis,r2rightES)
359 hold on
360 %ylabel('$\displaystyle r_{2}(x_{1},-0.0417H)$','interpreter','latex')
361 %xlabel('$\displaystyle x_{1}/L$','interpreter','latex')
362 %legend('$l_{c}=2\;mm$','$l_{c}=6\;mm$','$l_{c}=10\;mm$','Interpreter','latex');
```

B.3 Chebyshev–Gauss–Lobatto (CGL) grid

MATLAB code for generating CGL grid.

```
1 % --ChebyshevGaussLobatto (CGL) GRID
2 %9-noded
3 k=1;
4 for i=1:1:ny1
5       yc=(1-cos((i-1)/(ny1-1)*pi))*H/2;
6       for j=1:1:nx1
7       Xc(k,1)=(1-cos((j-1)/(nx1-1)*pi))*L/2;
8       Yc(k,1)=yc;
9       k=k+1;
10      end
11 end
```